UNIVERSIDAD CARLOS III DE MADRID
ESCUELA POLITÉCNICA SUPERIOR

AERODYNAMIC MODELS FOR HIGH-AMPLITUDE, LOW REYNOLDS FLAPPING AIRFOILS

Bachelor Thesis

Author

Elisa Morales Tirado

Leganés, September 2015

Department of Aerospace Engineering
ESCUELA POLITÉCNICA SUPERIOR

AERODYNAMIC MODELS FOR HIGH-AMPLITUDE, LOW REYNOLDS FLAPPING AIRFOILS

Bachelor in Aerospace Engineering

Author

Elisa Morales Tirado

Supervisor

Manuel Moriche Guerrero

Leganés, September 2015

Acknowledgements

Firstly, I would like to express my sincere gratitude to my supervisors Manuel Moriche Guerrero and Óscar Flores Arias for the continuous support during my Bachelor Thesis, for their patience, motivation, and immense knowledge. Their guidance helped me in all the time of research and writing of this thesis.

Besides my advisor, I would like to thank the CFD Group that with their suggestions and encouragement helped me to finish the thesis.

I thank my classmates for their support and for all the fun we have had in the last four years. With a special mention to those who have turned into true friends because they made the hours spent in the library more pleasant and they helped me to grow as a person.

Last but not the least, I would like to thank my family for supporting me spiritually throughout the four years of the degree and my life in general.
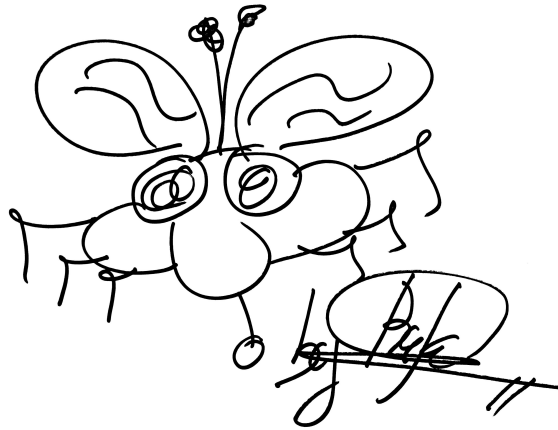
Abstract

In this thesis a new aerodynamic model of insect-like flapping flight for micro air vehicles has been developed. The New Predicted Aerodynamic Model (*NPAM*) was based on the model described by Weis-Fogh model in *Energetics of Hovering Flight in Hummingbirds and Drosophila*. In order to achieved the NPAM some variations were introduced regarding the geometry of the problem under study and also some improvements was done to the theory developed by Weis-Fogh. To have the required inputs for the model, a fitting from a DNS database for lift and drag coefficient, and aerodynamic efficiency was performed. Finally, the DNS database was also used to determine the accuracy and validity of the New Predicted Aerodynamic Model.

Contents

List of Figures

List of Tables

INTRODUCTION

1.1 State of the art

In this part it is going to be discussed the main aerodynamic modelling methodologies that are found in the literature for the development of micro air vehicle.

For this purpose the main division carried out by S.A. Ansari in its work *Aerodynamic modelling of insect-like flapping flight for micro air vehicles* [1] will be followed. The methods that are going to be reviewed are those that use theoretical aerodynamics only. These methods are divided in steady-state, quasi-steady and unsteady.

The steady-state methods are called in this way due to the fact that the analysis is performed once the steady-state is reached, however they can be considered quasi-steady.

Authors as Hoff [3] or Weis-Fogh [4] use actuator-disc-type analysis. In this theories the stroke planes described by insect wings beat are approximated to be an actuator disc. An actuator disc is an idealised surface that imparts momentum to a fluid to maintain a pressure difference. Following Momentum Theory, they derived an equation for the downwash velocity generated at the actuator disc ($w_i = \sqrt{W/2\pi\rho R^2}$). Ellington [5] further developed these theories by introducing a partial actuator disc instead of a circular disc since, rarely, the stroke amplitude was 180°. The difference between a partial actuator disc and a circular disc is shown in *figure 1.1*. Furthermore, Ellington noted that a pulse actuator disc could be more characteristic of flapping flight because the time-periodic nature of flapping.

Other steady-state methods are the developed by Rayner [6] based on insect flight vortex wake, and the developed by Sunada and Ellington [2] which modelled the shed vortex sheets in the wake as grid of small vortex rings (*figure 1.2*).

(a) Circular actuator disc

(b) partial actuator disc
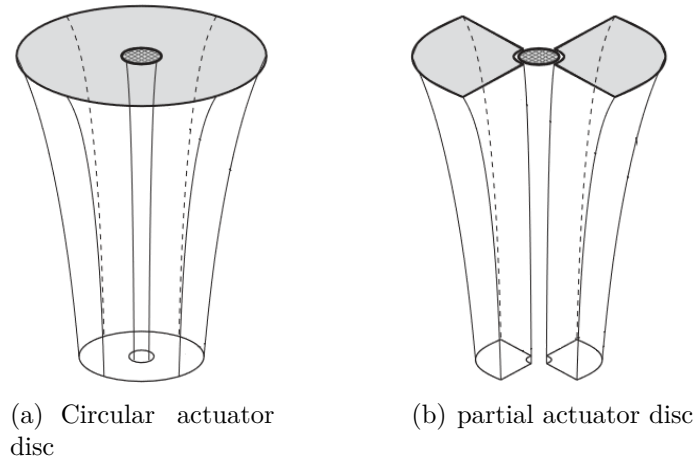
Figure 1.1: Differences between a circular and a partial actuator disc. Figure taken from the work of Ansari [1]

(a) Wake system

(b) Vortex ring arrangement on a vortex sheet
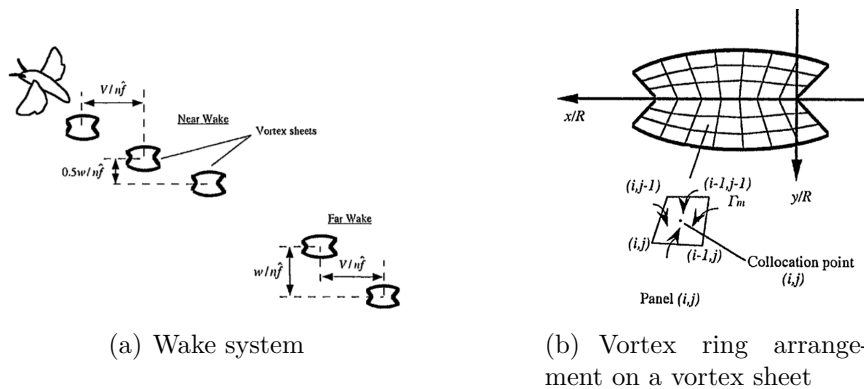
Figure 1.2: Sunada and Ellington model. Figure taken from their work [2]

Regarding the quasi-steady methods, they assume that the forces on the wing at any point in time are the steady-state values achieved by the wing at the same velocity and angle of attack.

Osborne [7] uses that the power required for wing to flap should be equal rate of change of kinetic energy passing into the slipstream to calculate mean values for the lift and drag coefficients.

Weis-Fogh [8] developed deeper its theory by coupling momentum theory with a blade-element method which enables to compute forces on chordwise wing elements. Ellington incorporates expression for lift due to translational and rotational phases also based on a blade-element method. Azuma [9], as well as Weis-Fogh, presented modelling techniques that combines momentum theory and blade-element methods.

Ansari [10] derived a quasi-steady method to model tip vortex by coupling a blade-element method with a Glauert-type analysis.

Finally, unsteady methods should be commented. They rely on unsteady aerodynamics. The most relevant characteristic of these methods is that they model the wake. They model the separation from the leading and trailing edge so as to model the conventional wake. Some authors that proposed unsteady methods are Azuma [9], Wu [11] or Żbikowski [12].

1.2   Objectives

The aim of this work is to find a simple method for modelling, as accurate as possible, the aerodynamic forces created during flapping flights. The word simple must be emphasise since the purpose of finding a model is to integrated it on Micro Air Vehicles (MAVs) that mimic insect-like flapping flight. The interest in these kind of vehicles has increased due to the multiple missions they can commit. MAVs usually have small size and are able to fly at low velocities.

There are already ways, such as Direct Numerical Simulations (DNS), that accurately find the aerodynamic forces. They solved numerically the complete set of Navier Stokes equations. The main drawback of DNS is their high computational cost. Moreover, the time needed to calculate the forces along a period can take X hours. The need of finding a model for the calculation of the forces arises from these two problems of DNS.

If at the end of the work we have been able to find this model, it can be considered a huge step for the development of Micro Air Vehicles.

FROM WEIS-FOGH TO THE NEW MODEL

In this work a new model to calculate the aerodynamic forces generated in flapping flight is going to be developed.

After reviewing the state of the art of the aerodynamic modelling of insect-like flight, it has been decided to base the model on the theory developed by Torkel Weis-Fogh in 1972 [4].

The aim of the model is to keep the simplicity of Weis-Fogh model but include new features to increase the reliability of the results.

In the following sections Weis-Fogh theory is going to be explained, as well as the modifications performed in order to obtain the improved model.

2.1 Torkel Weis-Fogh Theory

The aim that Weis-Fogh had in *Energetics of Hovering Flight in Hummingbirds and Drosophila*[4] was to offer a quantitative estimation of the force, work and power in large and small animals in hovering flight instead of providing a detailed analysis.

If the aerodynamic forces produced in hovering flight are integrated over cycle, the resultant force is vertical and equal to the weight. One cycle is composed by two strokes, downstroke plus upstroke (*figure 2.1*). The stroke plane, in which the motion of the long wing-axis is constrained, can be titled an angle β with respect to the horizontal. This is illustrated in *figure 2.2*.

The motion of the long wing-axis is considered to be almost sinusoidal relative to the angular displacement. For the calculations the movements normal to this stroke plane are neglected.

The angular movement is defined by *equation 2.1*.

$$\phi = \frac{1}{2}\pi + \frac{1}{2}\phi_0 \sin(\frac{2\pi t}{t_0})$$ (2.1)

Where ϕ is the instantaneous positional angle of the long wing-axis in the stroke
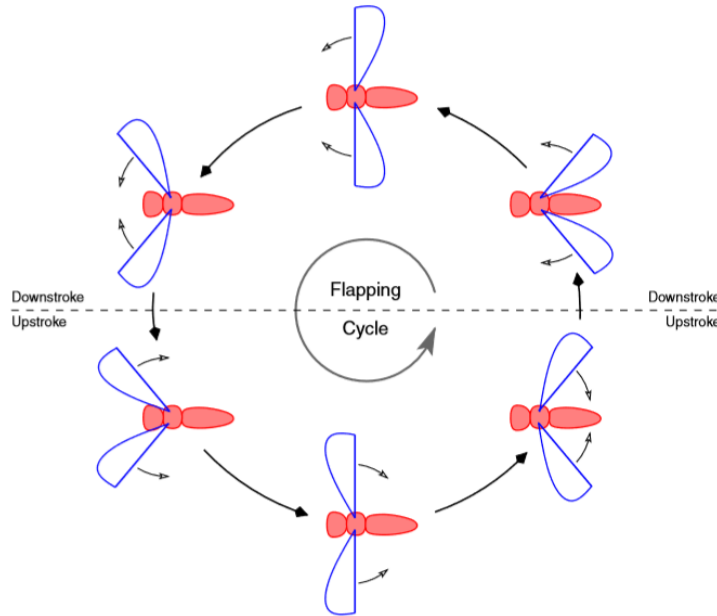
Figure 2.1: Flapping cycle. Taken from the work of Ansari [1]
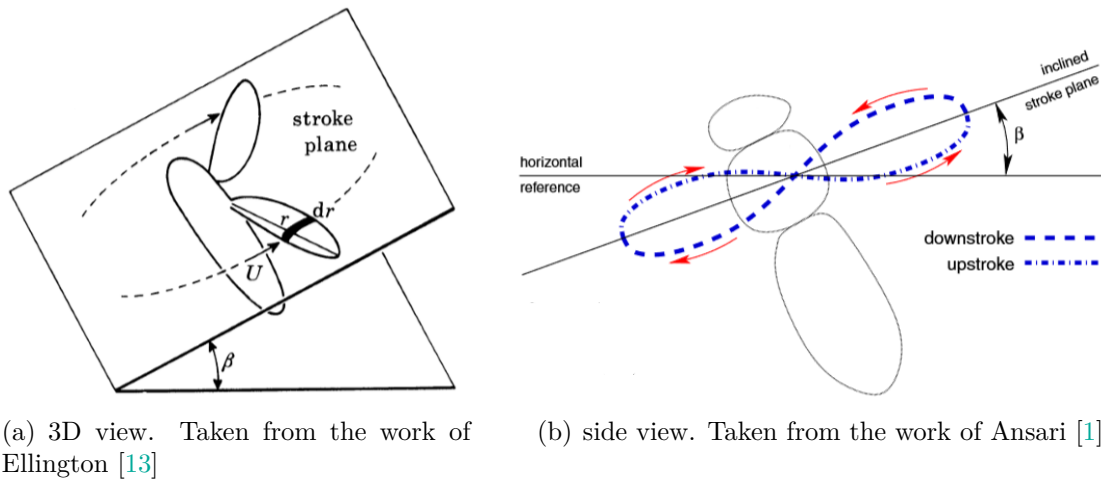
(a) 3D view. Taken from the work of Ellington [13]

(b) side view. Taken from the work of Ansari [1]

Figure 2.2: Stroke angle

plane, ϕ_0 is the stroke amplitude, t is time and t_0 is the period, therefore $t_0 = 1/f$ being f the wing-stroke frequency. In *figure 2.3* the definition of ϕ and ϕ_0 is pictured.

The angular velocity, $\dot{\phi}$, is found by taking the first derivative of the angular displacement with respect to time:

$$d\phi/dt = \dot{\phi} = \pi\phi_0 n \cos(2\pi nt) \tag{2.2}$$

Weis-Fogh defines the wing velocity, $\dot{h}$, for different wing elements (*figure 2.4*) multiplying the angular velocity by the distance of the specific wing element to the
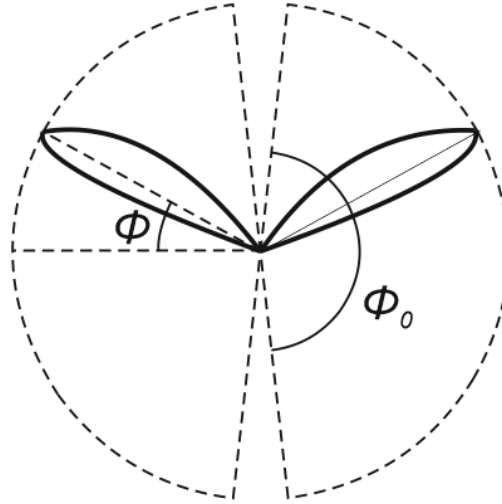
Figure 2.3: Illustration of ϕ and ϕ_0

fulcrum.

$$\dot{h}_i = r_i\dot{\phi} = r_i\pi\phi_0 f \cos(2\pi nt) \tag{2.3}$$
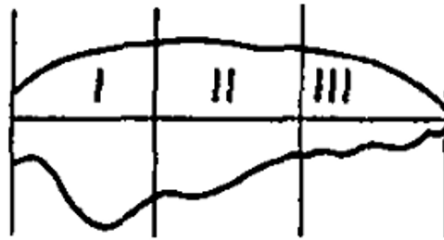
Figure 2.4: Wing elements

The second derivative with respect to time of the angular displacement gives the angular acceleration (*equation 2.4*).

$$d^2\phi/dt^2 = \ddot{\phi} = -2\phi_0\pi^2 n^2 \cos(2\pi nt) \tag{2.4}$$

The acceleration of the wing-mass causes a bending moment defined by:

$$Q_i = I\ddot{\gamma} = -2I\phi\pi^2 n^2 \cos(2\pi nt) \tag{2.5}$$

Being I the moment of inertia of the wing element i mass with respect to the fulcrum.

To compute the total aerodynamic force it must be known:

– The aerodynamic properties of the wing, given by the Lift and Drag coefficient.

   – The actual speed and direction of the flow seen by the wing, from now on referred as relative wind. The relative wind velocity (U_{eff}) is composed by the flapping velocity and the induced velocity. The induced velocity calculation is based on Momentum Theory (Actuator Disk Theory). The Momentum Theory is explained in *section 2.1.1*. And the flapping velocity from geometric calculations.

Once the expression for the induced velocity is gotten, the process to find the aerodynamic forces can be continued.

The resultant instantaneous force, F, is dependent on the square of the relative wind, the area of the wing element (A_r), and on Drag and Lift coefficients.

$$F = \frac{1}{2}\rho U_{eff}^2 A_r (C_L^2 + C_D^2)^{\frac{1}{2}} \tag{2.6}$$
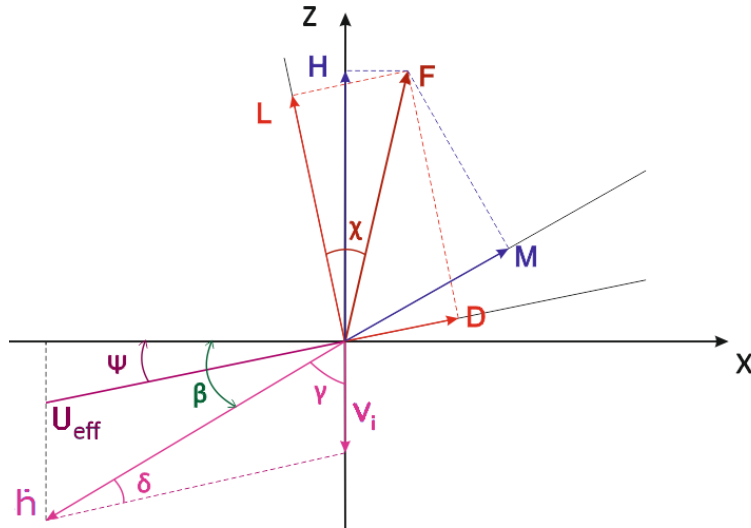
Figure 2.5: Weis-Fogh instantaneous forces and velocities

Figure 2.5 shows the outline of the forces generated during the downstroke for a section of the wing.

Besides it can be seen that Lift is measured normal to U_{eff} and Drag parallel to it. Nevertheless, the force that really matters is the vertical, or hovering force, H.

In order to calculate these forces the angle of tilt, β, and the value of Lift to Drag ratio, commonly called aerodynamic efficiency (E), must be known.

Looking at *figure 2.5*, an expression for the relative wind velocity can be obtained by applying cosine theorem to the triangle form by the induced velocity, v_i, the wing velocity $\dot{h}$, and the relative wind U_{eff}.

$$U_{eff}^2 = \dot{h}^2 + v_i^2 - 2\dot{h}v_i \cos\gamma \tag{2.7}$$

Being $\gamma = 90 - \beta$, and from trigonometry $\cos(90 - \beta) = \sin\beta$, *equation 2.7* consequently change to be:

$$U_{eff}^2 = \dot{h}^2 + v_i^2 - 2\dot{h}v_i\sin\beta \tag{2.8}$$

The angles δ and ψ are given by equations *2.9 and 2.10* respectively.

$$\sin\delta = \frac{v_i\cos\beta}{U_{eff}} \tag{2.9}$$

$$\psi = \delta - \beta \tag{2.10}$$

The aerodynamic efficiency, E, gives the equation for the angle χ.

$$\tan\chi = \frac{C_D}{C_L} \tag{2.11}$$

With the previous formula, *equation 2.6* can be worked out to be dependent on the Lift coefficient and on the input parameter χ.

$$F = \frac{1}{2}\rho U_{eff}^2 A_r (C_L^2 + C_L^2\tan\chi^2)^{\frac{1}{2}} \;\rightarrow\; F = \frac{1}{2}\rho U_{eff}^2 A_r C_L(1 + \tan\chi^2)^{\frac{1}{2}} \tag{2.12}$$

Using trigonometry:

$$\sin^2\chi + \cos^2\chi = 1 \;\rightarrow\; tan^2\chi + 1 = \frac{1}{cos^2\chi} \tag{2.13}$$

Conclusively, the resultant of the instantaneous force is:

$$F = \frac{1}{2}\rho U_{eff}^2 A_r \frac{C_L}{\cos\chi} \tag{2.14}$$

Weis-Fogh in order to calculate the forces expresses each wing element as a vortex with constant circulation. Therefore, there are some variables that change sign depending whether the upstroke or downstroke is being considered. They will change sign due to the fact that the circulation, Γ, is positive during the downstroke and negative in the upstroke. These variables are the angle χ and the lift coefficient C_L. They are defined to be positive when the circulation is too.

$$\chi = \chi_0 sign(\Gamma) \tag{2.15}$$

$$C_L = C_{L_0} sign(\Gamma) \tag{2.16}$$

χ_0 will be an input parameter and C_{L_0} is going to be obtained from the integration of the force in the z-direction over a period. The period is $T_p = \frac{2\pi}{k}$.

Projecting the resultant force into the vertical axis, the hovering force is found.

$$H = \frac{1}{2}\rho U_{eff}^2 A_r C_L \frac{\cos(\chi + \psi)}{\cos\chi} \tag{2.17}$$

As it has been mention, from the integration of this force over a period C_{L_0} is found.

$$\bar{H} = C_{L_0} \frac{1}{T_p} \int_0^{T_p} \frac{1}{2} \rho U_{eff}^2 A_r \frac{\cos(\chi + \psi)}{\cos \chi} dt \qquad (2.18)$$

Where $\bar{H}$ will be an input parameter.

Once it has been explained how to achieved the resultant force, we must take up the calculation of the induced velocity using momentum theory.

2.1.1   Momentum theory for hovering flight

Momentum theory was developed for marine propellers by W. J. M. Rankine in 1865 and R. E. Froude in 1885 [14]. This theory has also been applied to helicopters. The core of the theory is the application of basic conservation laws.

The objective of the analysis is to determine the influence of the rotor in the flow, specifically, to find the induced velocity. The induced velocity is the downward velocity produced by the wind load on the rotor disc. The rotor is modelled as an actuator disc. It is an infinitely thin disk with circular area, A, which can support a pressure difference, Δp, and consequently accelerates the air across itself.

During hover, the flow of air passing through the disc is defined by a streamtube above and below the disc. Outside the streamtube there is still air. No rotation is imparted to the flow [15]. This has been illustrated in *figure 2.6.*
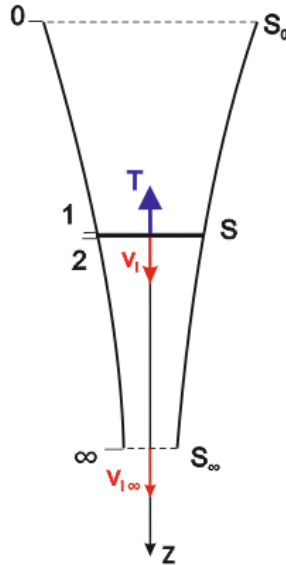
Figure 2.6: Flow model of a rotor in hovering flight

Since air is sucked into the disc, pressure drops until the flow reaches the disc. As mentioned, an increase of pressure equal to Δp occurs at the actuator disc. After

it the pressure falls again, eventually arriving back at the atmospheric level, p_∞. Velocity in the streamtube increases from zero at upstream infinity to a value v_i (induced velocity) at the disc and continues increasing until it reaches v_{i_∞} at downstream infinity.

Bernoulli's equation can be applied independently to the flow before disk and after it. Incompressible flow is assumed during the analysis. Before the disk it is obtained that:

$$p_\infty = p_i + \frac{1}{2}\rho v_i^2 \tag{2.19}$$

and after:

$$p_i + \Delta p + \frac{1}{2}\rho v_i^2 = p_\infty + \frac{1}{2}\rho v_{i_\infty}^2 \tag{2.20}$$

Rearranging *equations 2.19* and *2.20*, it is possible to obtain that:

$$\Delta p = \frac{1}{2}\rho v_{i_\infty}^2 \tag{2.21}$$

The next step is to apply in the z-axis momentum equation, from which *equations 2.22* is found. Fa is the force that the rotor exert on the fluid. This force is equal and opposite sign to the Thrust, T. Hence the minus sign only point out that the Thrust has contrary direction to the velocity downstream infinity.

$$\rho v_{i_\infty}^2 S_\infty = Fa = -T \tag{2.22}$$

The mass flux across any section parallel to the rotor is constant.

$$\dot{m} = \rho S v_i = \rho S_\infty v_{i_\infty} \tag{2.23}$$

Using *equation 2.23* and doing the modulus of *equation 2.22*, it changes to be:

$$\rho S v_i v_{i_\infty} = T \tag{2.24}$$

Where S is the area of the actuator disc.

Furthermore, the pressure different across the disc (Δp) is the Thrust divided by the disc area.

$$\Delta p = \frac{T}{S} = \rho v_i v_{i_\infty} \tag{2.25}$$

Equating the two expressions of the pressure different, *equations 2.21* and *2.25*, the relation between the induced velocity and the velocity downstream infinity is obtained.

$$v_{i_\infty} = 2v_i \tag{2.26}$$

Finally, the induced velocity is found by substituting this relation in *equation 2.24*.

$$T = 2\rho S v_i^2 \;\rightarrow\; v_i = \sqrt{\frac{T}{2\rho S}} \tag{2.27}$$

As it was previously said, the aerodynamic force produced as a result of hovering flight is vertical and equal to the weight. This means $T = W$, thus *equation 2.27* turns to be:

$$v_i = \sqrt{\frac{W}{2\rho S}} \tag{2.28}$$

2.2   Geometry adaptation

In order to have the required input parameters for the model, a direct numerical simulation database provided by my Bachelor Thesis' supervisor is going to be used. This database is going to be further explained in *section 3.2.1*.

So that, these first changes are more focused in defining, accordingly to the database, the geometry and the kinematics of the model.

First and foremost, rather than dividing the wing in different elements (*figure 2.4*) in order to calculate the total force, which gives a three-dimensional analysis to the model, it is assumed that all the wing elements produce the force since they have equal areas (A_r), therefore the wing is going to be treat as a unitary element with $A = bc$ and constant cross section defined by a *NACA 0012* airfoil. The fact that now an airfoil is considered to represent a wing element instead of a vortex with constant circulation will introduce some changes. These changes are going to be later explained.

Furthermore, instead of having the actuator disc located in the x-axis, it is placed in the z-axis. Consequently, all the angles must be redefined, as well as, the direction of the induced velocity, v_i, and the wing velocity.

(a) Downstroke

(b) Upstroke
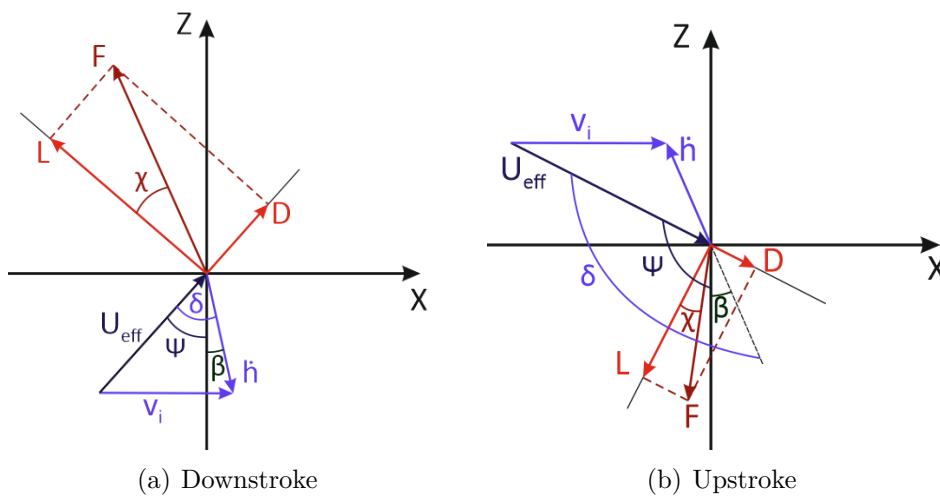
Figure 2.7: Outline of the model when the actuator disc is placed in z-axis

Figure 2.7 illustrates an outline of the forces, velocities and angles when the actuator disc is located in the vertical direction.

Consequently with the change of location of the actuator disc, the induced velocity is produced in the x-axis, as illustrated in *figure 2.8*.
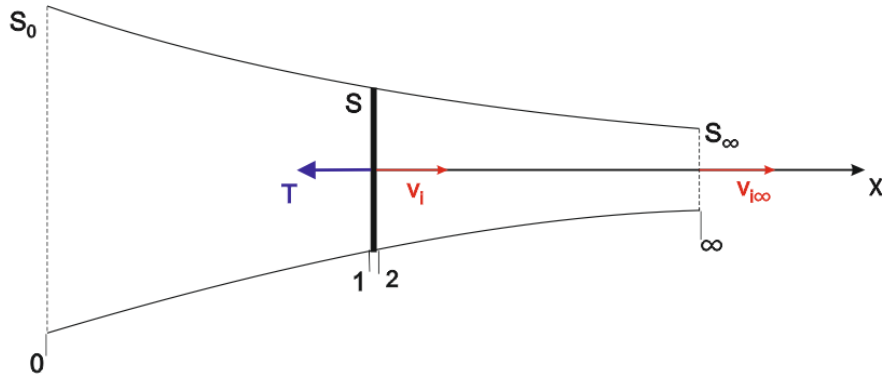
Figure 2.8: Control volume in hovering flight with a z-oriented actuator disc.

A part from changing the orientation of the actuator disc, the definition of its area is also changed. Previously it was defined by a circle due to the fact that the animal was assumed to be sweeping (for and aft motion of its wings) describing this geometry (*figure 2.3*). Since in the database the airfoil is plunging (up and down motion) and pitching (varying incidence), the area described by the motion of the wing will be a rectangle. Thus, the area of the actuator disc is $S = 2h_0 b$. Where h_0 is the semi-amplitude of the plunge and b is the wing span. This is pictured in *figure 2.9*.
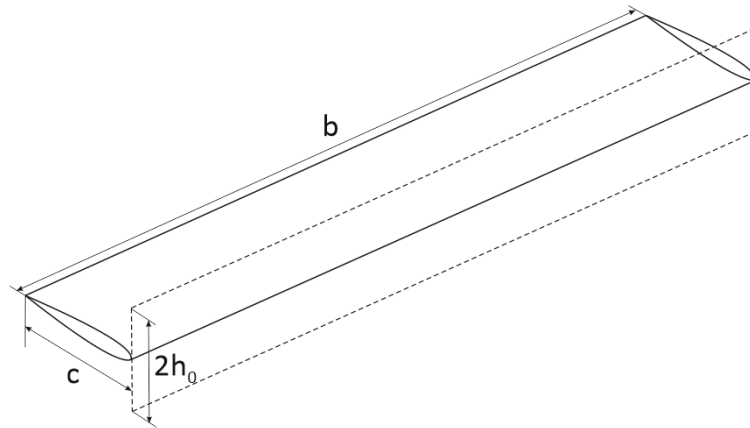
Figure 2.9: Wing geometry and amplitude of the heaving

Moreover, the wing velocity is given by the plunge velocity, $\dot{h}$. The up or down displacement of the wing, h, is governed by a sinusoidal law.

$$h = h_0 \sin(2\pi f t) \tag{2.29}$$

Being the reduced frequency $k = \frac{2\pi f c}{U_\infty}$, *equation 2.29* can also be expressed as:

$$h = h_0 \sin(k\frac{tU_\infty}{c}) \tag{2.30}$$

The plunging velocity is given by the first derivative with respect to time of h.

$$\dot{h} = h_0 k \frac{U_\infty}{c} \cos(k\frac{tU_\infty}{c}) \tag{2.31}$$

To ease the calculations, all the parameters in the model will expressed dimensionless. The dimensionless variables are going to be designated by ˆ. The characteristic variables used to acquire them are c, b, ρ and U_∞. The formulas for $\hat{h}$ and $\hat{\dot{h}}$ are:

$$\hat{h} = \frac{h_0}{c} \sin(k\hat{t}) \tag{2.32}$$

$$\hat{\dot{h}} = k\frac{h_0}{c} \cos(k\hat{t}) \tag{2.33}$$

Being $\hat{t} = \frac{tU_\infty}{c}$, $\hat{h} = \frac{h}{c}$ and $\hat{\dot{h}} = \frac{\dot{h}}{U_\infty}$. Besides, in the database, the ratio $\frac{h_0}{c}$ is set to be 1. This means that the maximum up or down displacement of the wing is equal to its chord.

To obtain a dimensionless formula for the effective velocity or relative wind velocity, U_{eff}, firstly, $\hat{v}_i$ must be defined.

$$\hat{v}_i{}^2 = \left(\frac{v_i}{U_\infty}\right)^2 = \frac{T}{2\rho U_\infty^2 2h_0 b} \tag{2.34}$$

Defining $\hat{T} = \frac{T}{\rho U_\infty^2 bc}$ and being $h_0 = c$, *equation 2.34* finally is:

$$\hat{v}_i = \sqrt{\frac{\hat{T}}{4}} \tag{2.35}$$

Where $\hat{T}$ is the mean value of the Thrust in a period. To denote that it is a mean value $\bar{\hat{T}}$ is used. Moreover, it must an input for the model. Actually, it is not an outcome of the database, but it can be calculated.
Therefore, the equation for $\hat{U}_{eff}$ can be achieved.

$$\hat{U}_{eff}^2 = \hat{\dot{h}}^2 + \hat{v}_i{}^2 - 2\hat{\dot{h}}\hat{v}_i \sin\beta \tag{2.36}$$

In addition, the angle ψ is defined by *equation 2.37* instead of *equation 2.10*.

$$\psi = atan\left(\frac{\hat{v}_i + \hat{\dot{h}}\sin\beta}{-\hat{\dot{h}}\cos\beta}\right) \tag{2.37}$$

Equation 2.37 will be valid for both, upstroke and downstroke.

As previously mentioned, for a correct definition of some variables, the motion of the wing must be considered. These variables are χ and C_L. Before, it was set that the sign of these parameters is given by the sign of the constant circulation of the vortex Γ. Since, instead of a vortex, an airfoil is being considered, the sign of the variables will be determined by the sign of the effective angle of attack of the airfoil. When α_{eff} is positive both parameters will be too. Therefore, *equations 2.15* and *2.16* are changed.

$$\chi = \chi_0 sign(\alpha_{eff}) \tag{2.38}$$

$$C_L = C_{L_0} sign(\alpha_{eff}) \tag{2.39}$$

As already mentioned, χ_0 will be an input parameter. C_{L_0} is going to be obtained from the integration of the force in the x-direction rather than the force in the z-direction over a period since the actuator disc has been placed vertically. The period is $T_p = \frac{2\pi}{k}$.

Although the calculation of the resultant force has been explained before, a deeper explanation is, herein, provided.

Firstly, a unitary lift coefficient should be defined, $C_{L_{UNIT}} = sign(\alpha_{eff})$. Thereon, the unitary instantaneous resultant force, $\hat{F}_{UNIT}$, is found.

$$\hat{F}_{UNIT} = \frac{1}{2}\left(\frac{U_{eff}}{U_\infty}\right)^2 \frac{C_{L_{UNIT}}}{\cos\chi} \tag{2.40}$$

The projection of the previous force onto x-axis and z-axis will give the unitary forces in the respectively axes.

$$\hat{F}_{x_{UNIT}} = -\hat{F}_{UNIT}\cos(\chi+\psi) \tag{2.41}$$

$$\hat{F}_{z_{UNIT}} = \hat{F}_{UNIT}\sin(\chi+\psi) \tag{2.42}$$

Then, from the force in the x-direction, C_{L_0} is achieved.

$$\bar{\hat{F}}_{x_{TUCAN}} = C_{L_0}\frac{1}{T_p}\int_0^{T_p}\hat{F}_{x_{UNIT}}dt \tag{2.43}$$

$\bar{\hat{F}}_{x_{TUCAN}}$ is the mean value of the force in the x-direction. It is an input parameter taken from the database. Once C_{L_0} is solved from *equation 2.43*, the total force in both directions can be calculated.

$$\hat{F}_x = C_{L_0}\hat{F}_{x_{UNIT}} \tag{2.44}$$

$$\hat{F}_z = C_{L_0}\hat{F}_{z_{UNIT}} \tag{2.45}$$

Noticed that, the above formulas express non-dimensional forces and no coefficient of forces in the corresponding direction. The coefficient of forces are computed dividing the forces by $\frac{1}{2}\rho U_\infty^2 bc$:

$$C_x = \frac{F_x}{\frac{1}{2}\rho U_{eff}^2 bc} = 2\hat{F}_x \qquad (2.46)$$

$$C_z = 2\hat{F}_z \qquad (2.47)$$

2.3   Axial Flight

The following step was the adaptation of Momentum Theory to axial flight. Hence, there will be a new definition for the induced velocity and, also, for some of the variables in the model.

The variables that change are the effective velocity and the angle ψ, which can be easily redefined by taking a look at *figure 2.10*.

(a) Downstroke   (b) Upstroke
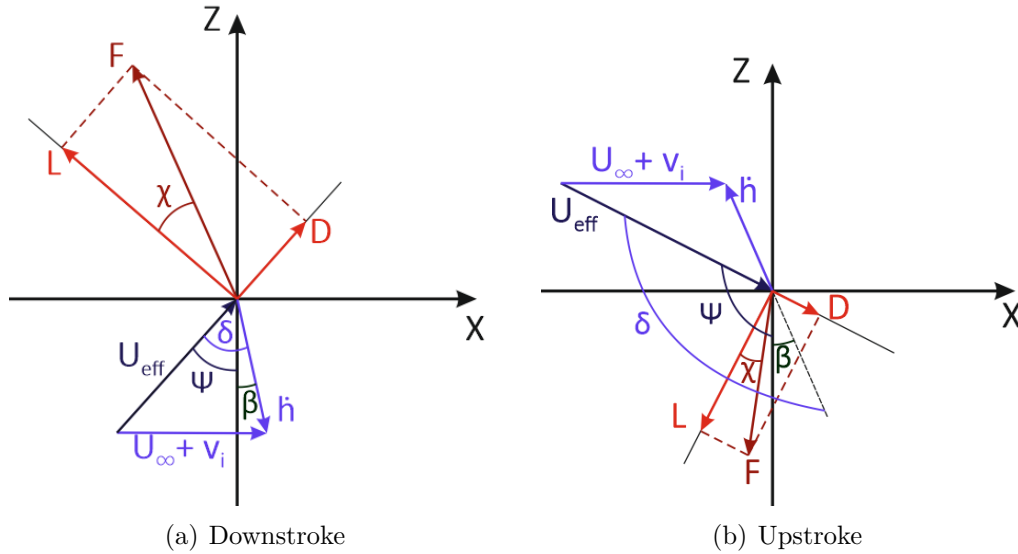
Figure 2.10: Outline of the model when axial flight is considered

The definition of this variables is affected by the introduction of a free stream velocity, U_∞.

$$U_{eff}^2 = (U_\infty + v_i)^2 + 2(U_\infty + v_i)\,\dot{h}\sin\beta + \dot{h}^2 \qquad (2.48)$$

$$\psi = atan\left(\frac{U_\infty + v_i + \dot{h}\sin\beta}{-\dot{h}\cos\beta}\right) \qquad (2.49)$$

Doing them non-dimensional;

$$\hat{U}_{eff}^2 = (1 + \hat{v}_i)^2 + 2(1 + \hat{v}_i)\,\hat{\dot{h}}\sin\beta + \hat{\dot{h}}^2 \qquad (2.50)$$

$$\psi = atan \left(\frac{1 + \hat{v}_i + \hat{\hat{h}} \sin \beta}{-\hat{\hat{h}} \cos \beta} \right) \tag{2.51}$$

In order to compute the force coefficient the procedure that must be followed is the same than in hovering flight (*equations 2.38 to 2.47*).

2.3.1 Momentum Theory for Axial Flight

As in Momentum Theory for hovering flight, mass, momentum and energy conservation equations are applied. However, in this case there is a free stream at the inlet of the streamtube that defines the control volume considered for the application of the equations.

The control volume is illustrated in *figure 2.11*.
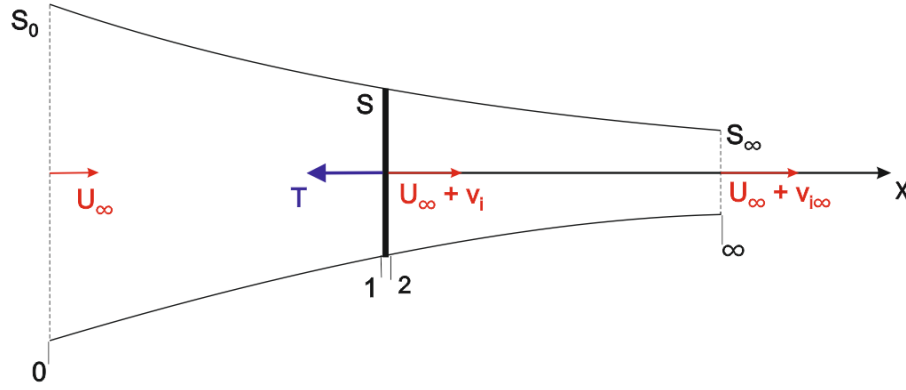
Figure 2.11: Control volume for axial flight

Equation 2.53 is obtained from mass conservation. Besides, it must bear in mind that mass flux is null across the lateral wall of the control volume (ref: teoria helicopteros).

$$\iint\limits_{S(z)} \rho \left(\bar{v} \cdot \bar{n} \right) d\sigma = \dot{m} \tag{2.52}$$

$$\rho S \left(V_x + v_i \right) = \rho S_\infty \left(V_x + v_{i_\infty} \right) = \rho S_0 V_x \tag{2.53}$$

In the axial direction of momentum conservation equation no viscous forces nor gravity forces are taken into account. Moreover, the resultant pressure force in the axial direction that act over the lateral, upper and lower surfaces, by first approximation, is null. Thus, the only pressure force that acts in the control volume is the exerted by the actuator disc, due to the fact that the pressure is different in the faces 1 and 2.

$$\iint\limits_{S_0} \rho V_x \left(\bar{v} \cdot \bar{n} \right) d\sigma + \iint\limits_{S_\infty} \rho \left(V_x + v_{i_\infty} \right) \left(\bar{v} \cdot \bar{n} \right) d\sigma = - \iint\limits_{S_1} p\bar{n} d\sigma - \iint\limits_{S_2} p'\bar{n} d\sigma \tag{2.54}$$

The right hand side terms of *equation 2.54* are equal to the force that the rotor produces on the fluid, which is, as previously mentioned, equal but with opposite sign to Thrust. So that, *equation 2.54* leads to:

$$-\rho S_0 V_x^2 + \rho S_\infty \left(V_x + v_{i_\infty}\right)^2 = F_a = -T \tag{2.55}$$

The relation obtained in *equation 2.53* between the mass flow at the entrance of the control volume and at the end must be substituted in *equation 2.55*.

$$-\rho S_0 V_x^2 + \rho S_0 V_x \left(V_x + v_{i_\infty}\right) = -T \tag{2.56}$$

$$\rho S_0 V_x v_{i_\infty} = -T \tag{2.57}$$

Where the minus sign indicates that the Thrust is oriented in the negative x-axis.

The energy equation expresses that the induced power consumed by the rotor is used to augment the kinetic energy of the flow. This increment is evaluated between the inlet and outlet of the control volume.

$$P_i = \frac{1}{2}\dot{m}\left[(V_x + v_{i_\infty})^2 - V_x^2\right] \tag{2.58}$$

Another form of defining the induced power is by the work that Thrust does on the fluid.

$$P_i = -\vec{T}\left(\vec{V}_x + \vec{v}_i\right) \tag{2.59}$$

Equalising *equation 2.58* and *2.59*, the relation between the induced velocity at the actuator disc and the induced velocity at downstream infinity achieved for hovering flight, *equation 2.26*, is again obtained for axial flight.

$$\dot{m}v_{i_\infty}\left(V_x + v_i\right) = \frac{1}{2}\dot{m}\left[(V_x + v_{i_\infty})^2 - V_x^2\right] = \frac{1}{2}\dot{m}\left[V_x^2 + 2v_{i_\infty}V_x + v_{i_\infty}^2 - V_x^2\right]$$
$$\left(V_x + v_i\right) = \frac{1}{2}\left(2V_x + v_{i_\infty}\right) \tag{2.60}$$
$$2v_i = v_{i_\infty}$$

Therefore, the modulus of the Thrust is given by:

$$T = 2\rho S_0 V_x v_i = 2\rho S \left(V_x + v_i\right) \tag{2.61}$$

Expressing the above equation into dimensionless form and knowing that T is the mean value over a period, *equation 2.62* is found. The actuator disc area is $A = 2h_0 c$.

$$\bar{\hat{T}} = 2\frac{h_0}{c}\left(\hat{v}_i^2 + \hat{v}_i\right) \tag{2.62}$$

Equation 2.62 is a second order equation, therefore two results for $\hat{v}_i$, one positive and another negative, are obtained. From the situation illustrated in *figure 2.11*, it is known that the induced velocity goes in the positive direction of x-axis, so that, the positive result for $\hat{v}_i$ is chosen.

2.4 Any possible orientation for the actuator disc

The final step was the application of Momentum Theory for an actuator disc that is not necessarily placed in the vertical or horizontal axis. Once again, the definition of the induced velocity will variate together with some variables of the model.

Due to the fact that the actuator disc can have any orientation, the induced velocity too, and it is perpendicular to the actuator disc. Therefore, the induced velocity will have components in x and z-axis, u_i and w_i respectively. This change is illustrated in *figure 2.12*.

(a) Downstroke   (b) Upstroke
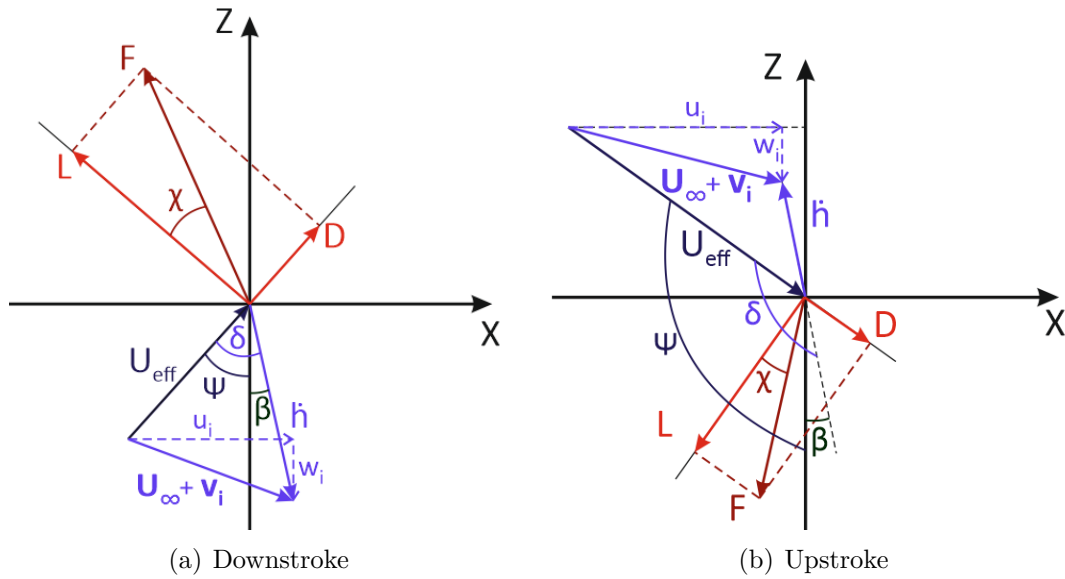
Figure 2.12: Outline of the model when the actuator disc is placed at any orientation

As for axial flight, the variables that change are U_{eff} and ψ.

$$U_{eff}^2 = \left(U_\infty + u_i + \dot{h}\sin\beta\right)^2 + \left(w_i + \dot{h}\cos\beta\right)^2 \tag{2.63}$$

$$\psi = atan\left(\frac{U_\infty + u_i + \dot{h}\sin\beta}{-\left(w_i + \dot{h}\cos\beta\right)}\right) \tag{2.64}$$

The dimensionless expressions for the equations above are:

$$\hat{U}_{eff}^2 = \left(1 + \hat{u}_i + \hat{\dot{h}}\sin\beta\right)^2 + \left(\hat{w}_i + \hat{\dot{h}}\cos\beta\right)^2 \tag{2.65}$$

$$\psi = atan\left(\frac{1 + \hat{u}_i + \hat{\dot{h}}\sin\beta}{-\left(\hat{w}_i + \hat{\dot{h}}\cos\beta\right)}\right) \tag{2.66}$$

Then, the method followed to calculate the force coefficients will be maintained. Equations from *2.38* to *2.47* must be computed.

2.4.1 Momentum Theory for any position of the actuator disc

The control volume that is considered to apply mass, momentum and energy equations is show in *figure 2.13*.
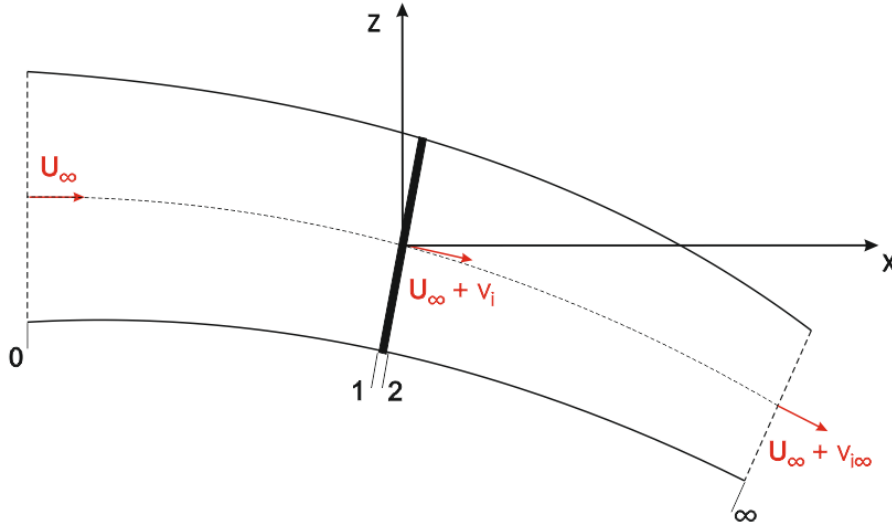
Figure 2.13: Control volume for an actuator disc

Since the exact direction of the induced velocity is not known, the vectorial notation should be kept while applying the equations for the described control volume.

Mass conservation equation gives:

$$\dot{m} = \rho\|\vec{U}_\infty\|S_0 = \rho\|\vec{U}_\infty + \vec{v}_{i_\infty}\|S_\infty = \rho\|\vec{U}_\infty + \vec{v}_i\|S \tag{2.67}$$

Where

$$\begin{aligned}\vec{U}_\infty &= U_\infty \vec{e}_x \\ \vec{v}_i &= u_i\vec{e}_x + w_i\vec{e}_z \\ \vec{v}_{i_\infty} &= u_{i_\infty}\vec{e}_x + w_{i_\infty}\vec{e}_z\end{aligned} \tag{2.68}$$

Equation 2.69 is obtained from momentum conservation equation.

$$-\rho S_0 U_\infty^2 \vec{e}_x + \rho S_\infty \|\vec{U}_\infty + \vec{v}_{i_\infty}\| \left(\vec{U}_\infty + \vec{v}_{i_\infty}\right) = -\vec{F} \tag{2.69}$$

Previous equation can be simplified using *equation 2.67*.

$$\vec{F} = -\rho S \vec{v}_{i_\infty}\|\vec{U}_\infty + \vec{v}_i\| \tag{2.70}$$

There are two alternatives in order to defined the induced power (*equation 2.71* and *2.72*). Equalising them a relation between the induced velocity at the actuator disc and downstream infinity is achieved (*equation* **??**).

$$P_i = \frac{1}{2}\dot{m}\left[\|\vec{U_\infty} + \vec{v}_{i_\infty}\|^2 - \|\vec{U}_\infty\|^2\right] \tag{2.71}$$

$$P_i = -\vec{F}\left(\vec{U_\infty} + \vec{v}_i\right) = \dot{m}\vec{v}_{i_\infty}\left(\vec{U_\infty} + \vec{v}_i\right) \tag{2.72}$$

So that,

$$\vec{v}_{i_\infty} = 2\vec{v}_i \tag{2.73}$$

This relation is substituted into *equation 2.70.*

$$\vec{F} = -2\rho S\vec{v}_i\|\vec{U}_\infty + \vec{v}_i\| \tag{2.74}$$

Decomposing it in the contributions to x and z-axis, a system of two equations with two unknowns is found.

$$\begin{aligned}
\bar{F}_x &= -4\rho h_0 b u_i\sqrt{\left(U_\infty + u_i\right)^2 + w_i^2} \\
\bar{F}_z &= -4\rho h_0 b w_i\sqrt{\left(U_\infty + u_i\right)^2 + w_i^2}
\end{aligned} \tag{2.75}$$

In non-dimensional form:

$$\begin{aligned}
\bar{\hat{F}}_x &= -4\frac{h_0}{c}\hat{u}_i\sqrt{\left(1 + \hat{u}_i\right)^2 + \hat{w}_i^2} \\
\bar{\hat{F}}_z &= -4\frac{h_0}{c}\hat{w}_i\sqrt{\left(1 + \hat{u}_i\right)^2 + \hat{w}_i^2}
\end{aligned} \tag{2.76}$$

For each of the unknowns, the system of equation gives 4 solutions. Two real solutions and one pair of complex conjugates. Accordingly with how the axis has been defined, the positive real solution will be chosen for u_i and the negative real solution for w_i.

2.5   Summary of the main differences

In *table 2.1* the main differences between the Weis-Fogh model and the new predicted aerodynamic model are remarked.

Weis-Fogh Model	NPAM
3D analysis $\rightarrow$ wing is divided wing elements	2D analysis $\rightarrow$ wing is a single element
Point vortex with constant Γ	Airfoil (NACA 0012)
Actuator disc located in x-axis	Actuator disc can be placed in any direction
Wing is sweeping	Wing is plunging and pitching
Actuator disc area: $S = \pi R^2$	Actuator disc area: $S = 2h_0 c$

Table 2.1: Main differences between the models

NEW PREDICTED AERODYNAMIC MODEL

This chapter is devoted to explain deeper how the new predicted aerodynamic model works and which are the needed inputs for the model, as well as which are the outputs obtained from it.

In the first place, an outline of the steps that were followed from Weis-Fogh model until the New Predicted Aerodynamic Model (*NPAM*) was reached is, herein, done.

- Geometric adaptation (*section 2.2*):

    - Actuator disc is placed in the vertical axis.
    - Consider the wing as a single element with $A = bc$.
    - Cross section of the wing given by an airfoil NACA 0012.
    - The wing is plunging and pitching.
    - Change of the area of the actuator disc ($S = 2h_0b$).

- Axial Flight (*section 2.3*): Addition of a free stream in x-direction.

- Actuator disc can be oriented in any direction (*section 2.4*).

Once the main steps followed has been reviewed, it is time to set which are the inputs that the model must have.

The inputs required are listed below.

- Kinematics: h_0/c, k, ϕ, θ_0 and θ_m.

- C_l and C_d to obtain E. The definition of the possible models and the model selection is explained in *section 3.2*.

- $\bar{\hat{F}}_x$ and $\bar{\hat{F}}_z$ to be able to calculate the induced velocity. They are gotten from the DNS database.

After the calculations, the obtained outputs of the model are the evolution along a period of $\hat{F}_x$ and $\hat{F}_z$.

3.1 Modes of the New Predicted Aerodynamic Model

In this section, the two alternatives for the model are going to be presented. The main difference between them is that one of the options is based on an iterative process.

The first option (Option 1) is a non-iterative process. First the inputs of the model are set, then, the calculations that described the model are done, and, finally, the forces in the x and z-direction are found. In *figure 3.1* the flowchart of Option 1 is described.
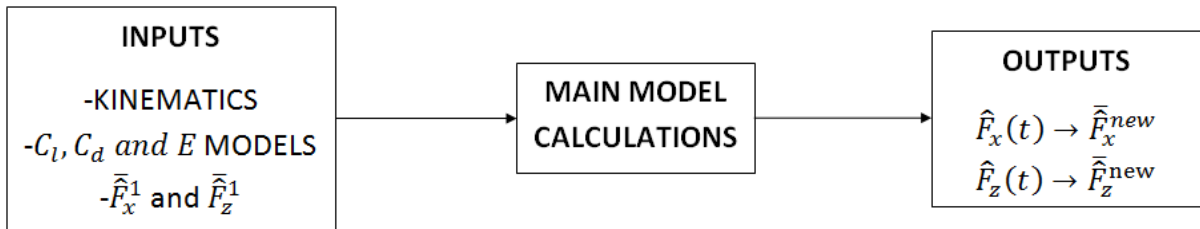
Figure 3.1: Option 1 flowchart

The second option (Option 2) to be studied perform an iterative process with the purpose to obtain the same value for the inputs $\hat{\bar{F}}_x$ and $\hat{\bar{F}}_z$ than for these parameters when calculating from the output forces.

An initial guess for $\hat{\bar{F}}_x$ and $\hat{\bar{F}}_z$ is needed. The guess in this case is given by the available data form the DNS. When all the calculations are done the new values for $\hat{F}_x$ and $\hat{F}_z$ are calculated. If the difference between this value and the input is greater than 10^{-8} the iterations will continue until the error is reduced to that value.

Since in this option $\hat{\bar{F}}_x$ and $\hat{\bar{F}}_z$ are not known beforehand, we have are only an initial guess, another variable must be assumed to be known. In this case, the known parameter will be the lift coefficient. The lift coefficient is found in *section 3.2*.

In *figure 3.2* a flowchart of the option 2 is shown.

3.2 Selection of C_l, C_d and E models for the inputs

As it has been said, the aerodynamic efficiency E is an input for the new predicted aerodynamic model. Therefore, in order to obtain a model for E, firstly, models for the lift and drag coefficients must be determined. Besides, the lift coefficient must be known when the model is working with the Option 2.
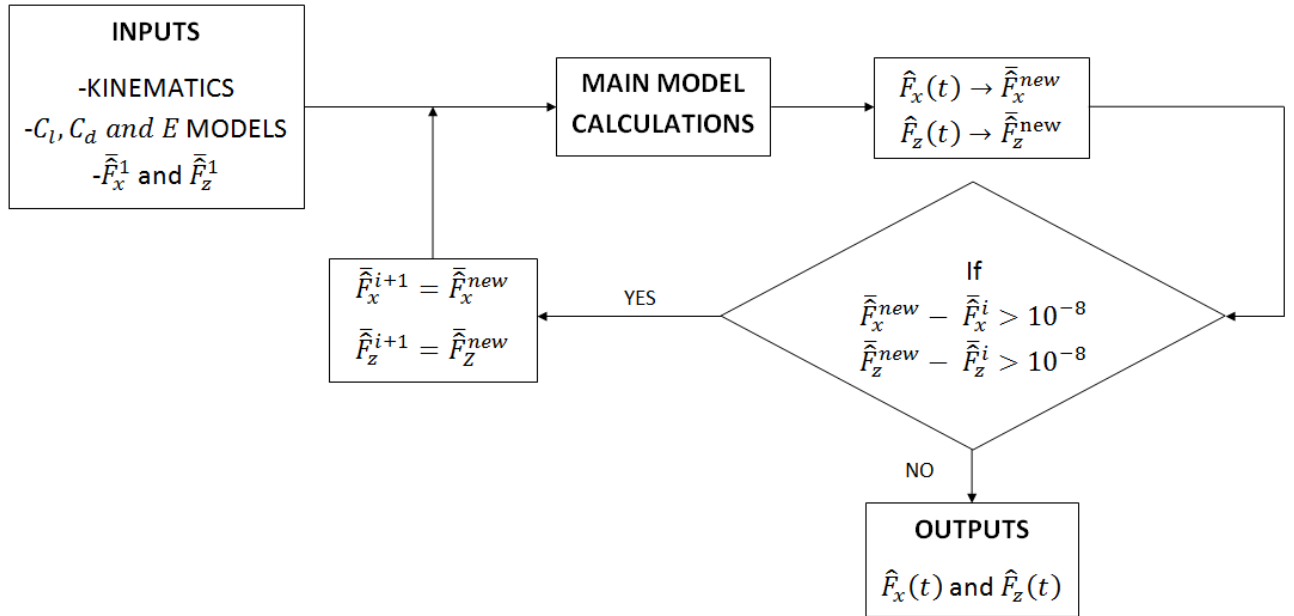
Figure 3.2: Option 1 flowchart

In order to select the most suitable model, the DNS database is going to be used as reference. In *section 3.2.1* the Direct Numerical Simulation is explained.

3.2.1   Direct Numerical Simulation Database

As previously mentioned, a Direct Numerical Simulation (DNS) database is used to measure the accuracy of the predicted aerodynamic forces by the new model.

The aim of Direct Numerical Simulations is to solve numerically Navier Stokes equations without using a model. The problem is spatially and temporarily discretized. For the spatial discretization a second order finite difference scheme on a staggered grid is used. For the temporal discretization a third order Runge Kutta method is applied. With the use of DNS the values of the two velocity components and the pressure are available.

The problem under study is the flow around an aerodynamic airfoil (NACA 0012) in plunging and pitching motion. Incompressible flow is assumed. The Reynolds number of the flow is $Re = \frac{cU_\infty}{\nu} = 1000$. Where c is the chord of the airfoil, U_∞ is the free stream velocity and ν is the kinematic viscosity.

The motion of the airfoil is illustrated in ,*figure 3.3*. Pitching and plunging are defined by *equations 3.1* and *3.2* respectively. Where θ_0 is the pitching amplitude, k is the reduced frequency and h_0 is the plunging semi-amplitude.

$$\theta = \theta_m + \theta_0 \sin\left(k\hat{t} + \phi\right) \tag{3.1}$$

$$h = h_0 \sin\left(k\hat{t}\right) \tag{3.2}$$
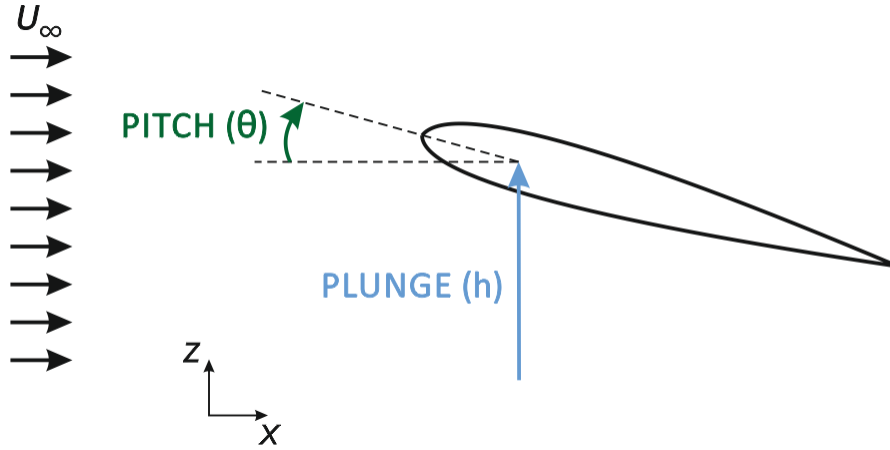
Figure 3.3: Problem description

The database provided has 18 simulations. The different simulations were obtained by varying the mean pitch value, θ_m, and the phase shift, ϕ.

The fixed parameter of the problem are $k = \frac{2\pi c f}{U_\infty} = 1.41$, $\theta_0 = 30°$ and $h_0/c = 1$. Moreover, θ_m can take the values $\theta_m = 0°, 10°, 20°$ and $\phi = 30°, 50°, 70°, 90°, 110°, 130°$.

MAS	$\theta_m\,[°]$	$\phi\,[°]$
0000*		30
0001		50
0002	0	70
0003		90
0004		110
0005		130
1000		30
1001		50
1002	10	70
1003		90
1004		110
1005*		130
2000*		30
2001*		50
2002*	20	70
2003*		90
2004*		110
2005*		130

Table 3.1: MAS data

In *table 3.1* the values of the variables for each simulation is specified. Each simulation is called MAS (*Moving Airfoil Simulation*) and followed by 4 digits. The first two digits indicate the mean pitch value and the last two indicate the variation of the phase shift.

The motion of the airfoil is always periodic, but the flow can be periodic or non-periodic. For the periodic cases any period can be taken to calculate the coefficients. However, when the case is non-periodic five periods have been taken to do the average of the forces. In order to see if they are periodic or not, the forces of two periods are plotted together and if they coincide the case will be periodic, and if not, the case is non-periodic. The cases that are non-periodic are marked with * in *table 3.1*.

Figure 3.4 illustrated $\hat{F}_x = \frac{F_x}{\rho U_\infty^2 c}$ along a period for a periodic case (MAS 1003) and for a case that it is not periodic (MAS 0000).

(a) Periodic case (MAS 1003)   (b) Non-periodic case (MAS 0000)
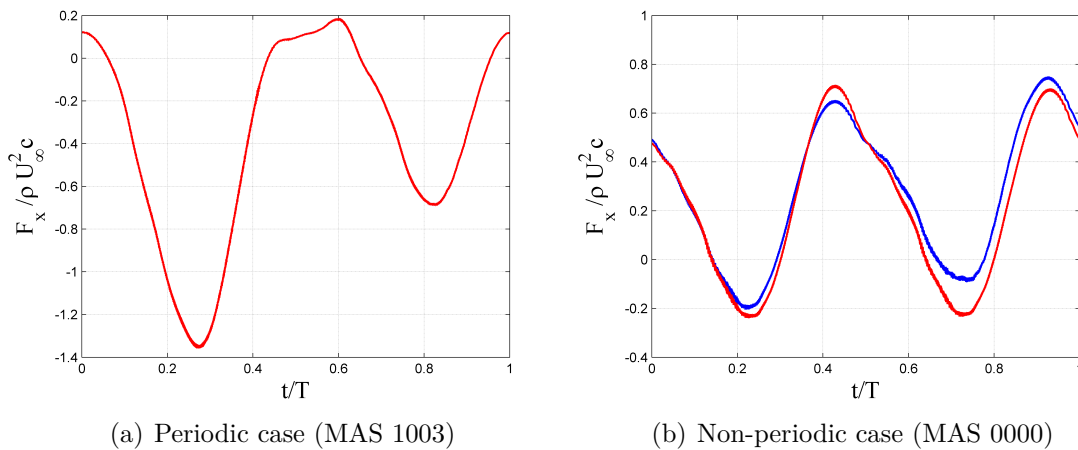
Figure 3.4: $\hat{F}_x$ over a period. First period (——) and second period (——)

Figure 3.5 shows for the same cases than *figure 3.4* the non-dimensional force in z-axis $\hat{F}_z = \frac{F_z}{\rho U_\infty^2 c}$.

The non-dimensional force in x and z-direction are outputs obtained from the simulations. So that, the Lift and Drag can be calculated from them. In addition, to find the lift and drag coefficient it must bear in mind that what it is available are non-dimensional forces and them must be transform to coefficients $C_{F_x} = \frac{F_z}{\frac{1}{2}\rho U_\infty^2 c} = 2\hat{F}_x$. Moreover, the characteristic velocity used to do the forces non-dimensional is the free stream, whereas the incidence velocity used in order to obtain the lift and drag coefficient is the effective velocity.

Observing *figure 3.6* and taking into account what it was previously said, the

3. NEW PREDICTED AERODYNAMIC MODEL

(a) Periodic case (MAS 1003)   (b) Non-periodic case (MAS 0000)
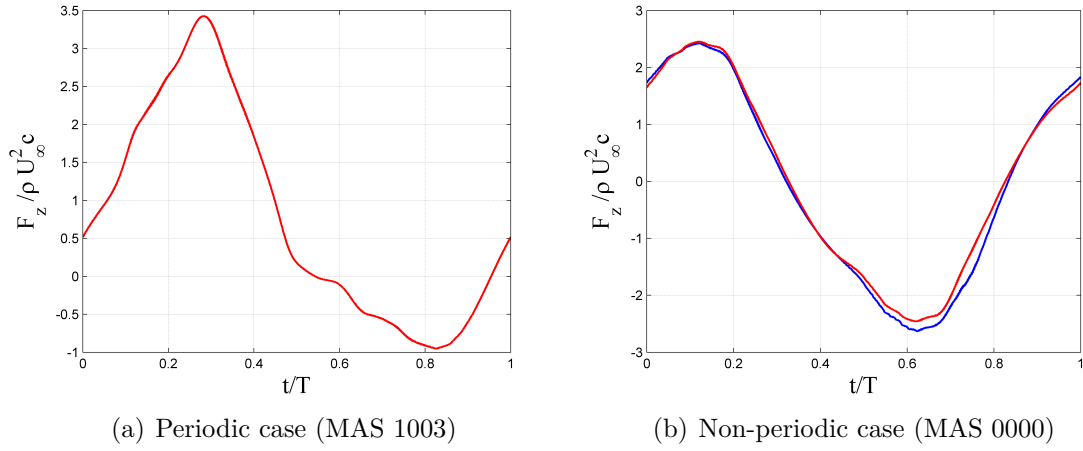
Figure 3.5: $\hat{F}_z$ over a period. First period (—) and second period (—)

equations for the lift and drag coefficient are determined.
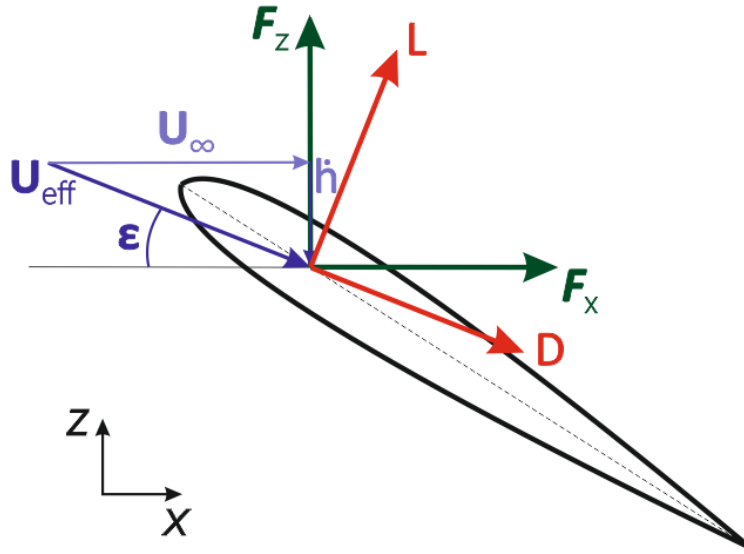
Figure 3.6: Outline of the forces

Figure 3.6 illustrates that drag is parallel to the effective velocity, U_{eff} and that lift is perpendicular to U_{eff}. The angle between the effective velocity and the horizontal has been denoted with the Greek letter ε. Therefore, the equations for lift and drag coefficients are obtained.

$$C_l = \frac{L'}{\frac{1}{2}\rho U_{eff}^2 c}\frac{U_\infty^2}{U_\infty^2} = 2\left(\hat{F}_x \sin\varepsilon + \hat{F}_z \cos\varepsilon\right)/\hat{U}_{eff}^2 \tag{3.3}$$

$$C_d = 2\left(\hat{F}_x \cos\varepsilon - \hat{F}_z \sin\varepsilon\right)/\hat{U}_{eff}^2 \tag{3.4}$$

Where

$$\varepsilon = atan\left(\hat{\dot{h}}\right) \tag{3.5}$$

$$\hat{U}_{eff} = \sqrt{1+\hat{\dot{h}}^2} \tag{3.6}$$

Being $\hat{\dot{h}} = k\frac{h_0}{c}\cos\left(k\hat{t}\right)$ and $\hat{t} = \frac{tU_\infty}{c}$

In the following figures it is possible to appreciate how the found lift and drag coefficients evolve during a period, as well as, the effective angle of attack. The effective angle of attack is defined by $\alpha_{eff} = \theta - \varepsilon$.

They are plotted first fixing the value of θ_m and varying ϕ and later the other way around.

Figure 3.7 represents C_l when the mean pitch value, θ_m, is fixed and the variable parameter is the phase shift ϕ.

(a) $\theta_m = 0°$

(b) $\theta_m = 10°$

(c) $\theta_m = 20°$
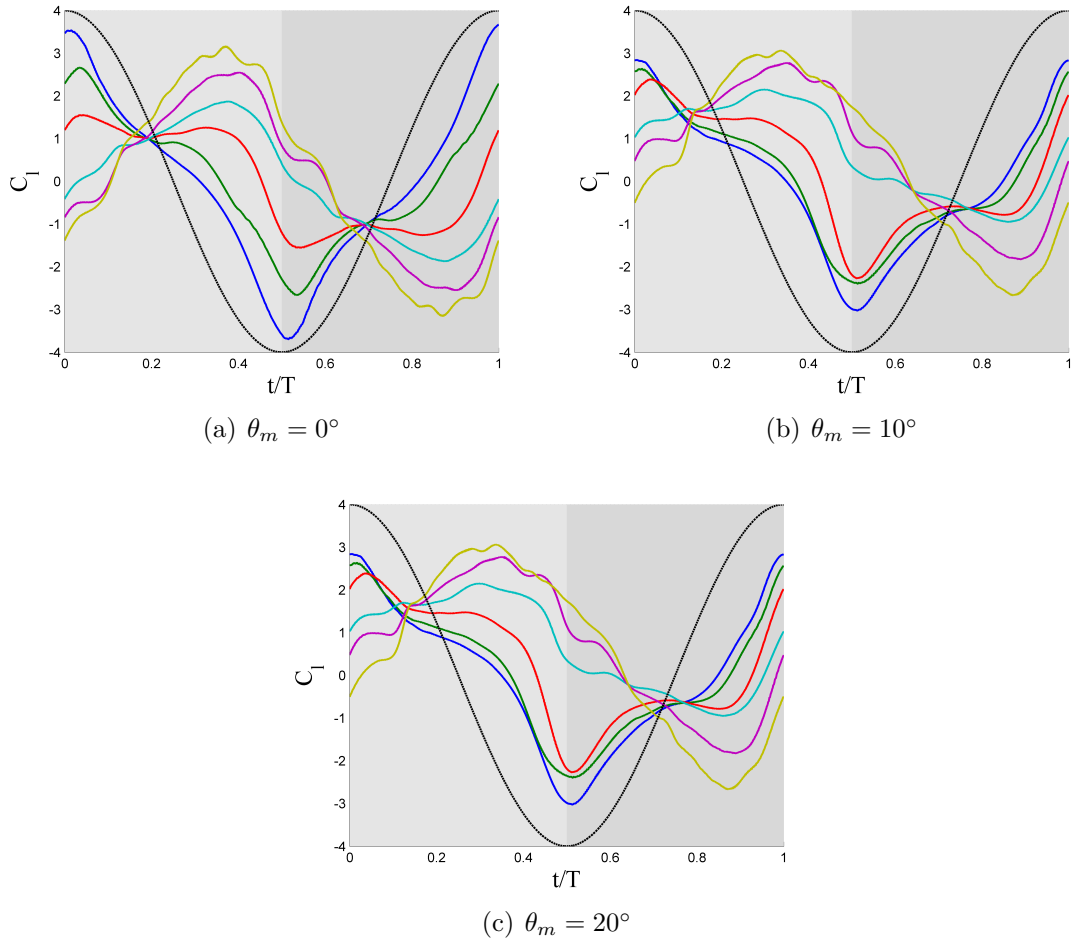
Figure 3.7: C_l with same θ_m and varying ϕ. $\phi = 30°$ (——), $\phi = 50°$ (——), $\phi = 70°$ (——), $\phi = 90°$ (——), $\phi = 110°$ (——) and $\phi = 130°$ (——)

Figure 3.8 shows how C_d changes when the mean pitch value, θ_m, is fixed and the variable parameter is the phase shift ϕ.

(a) $\theta_m = 0°$

(b) $\theta_m = 10°$

(c) $\theta_m = 20°$
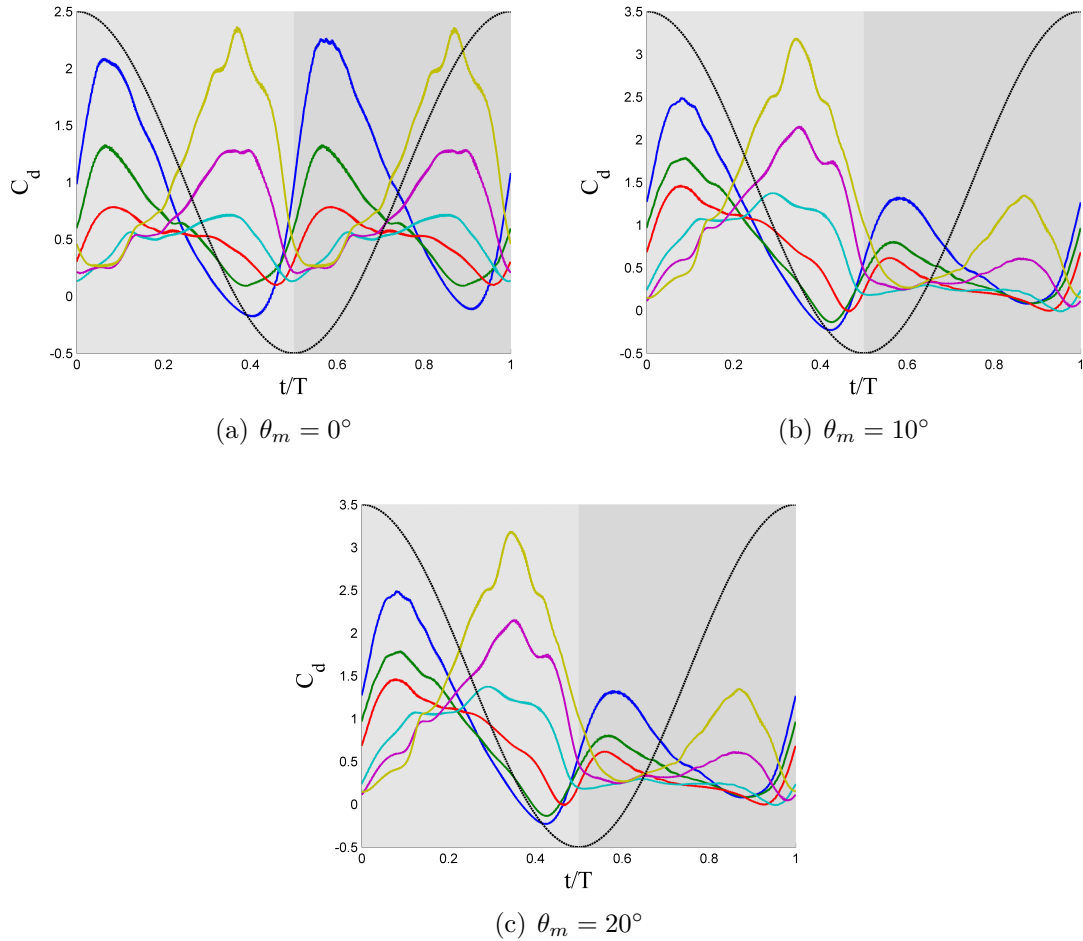
Figure 3.8: C_d with same θ_m and varying ϕ. $\phi = 30°$ (——), $\phi = 50°$ (——), $\phi = 70°$ (——), $\phi = 90°$ (——), $\phi = 110°$ (——) and $\phi = 130°$ (——)

In *figure 3.9* it is illustrated how C_d changes when θ_m is fixed and the variable parameter is ϕ.

(a) $\theta_m = 0°$

(b) $\theta_m = 10°$

(c) $\theta_m = 20°$
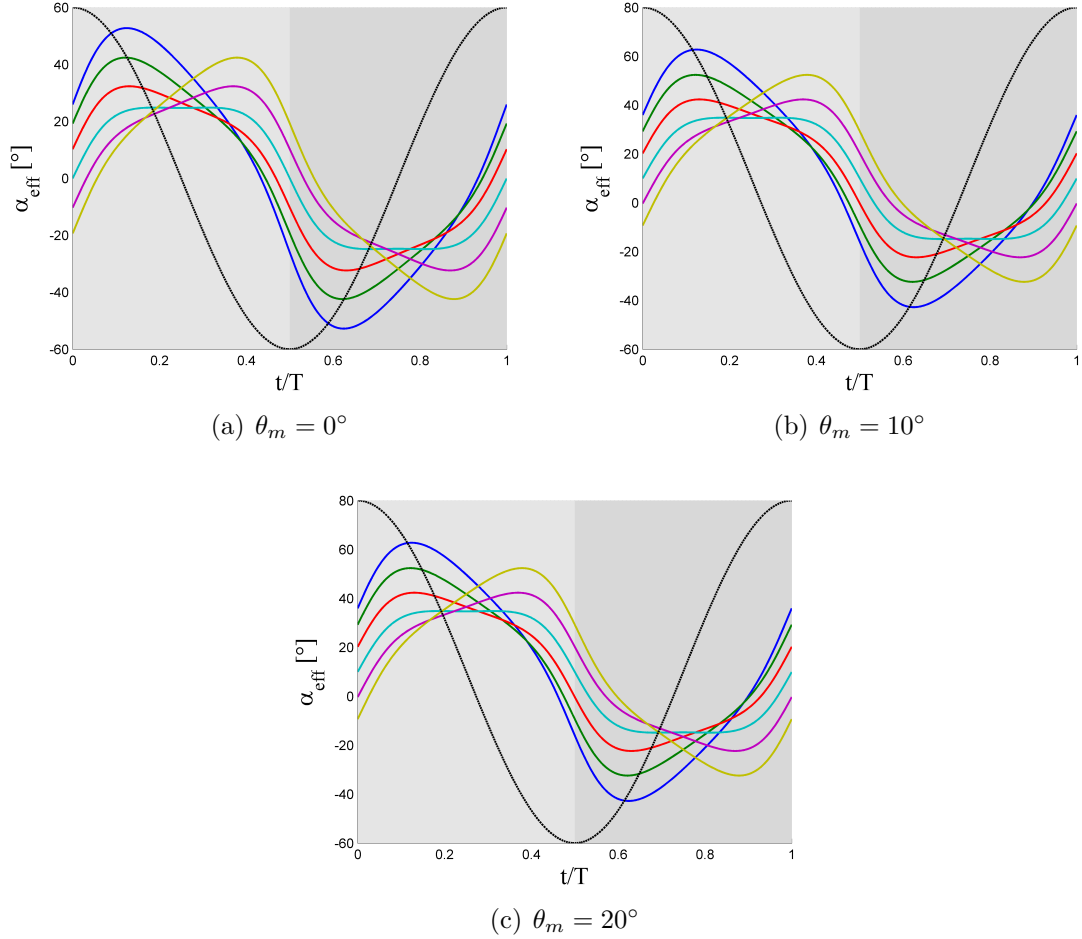
Figure 3.9: α_{eff} with same θ_m and varying ϕ. $\phi = 30°$ (——), $\phi = 50°$ (——), $\phi = 70°$ (——), $\phi = 90°$ (——), $\phi = 110°$ (——) and $\phi = 130°$ (——)

Now the variable that is fixed is the phase shift(ϕ). *Figure 3.10* shows the variation of C_l from different values of θ_m and a constant ϕ.

(a) $\phi = 30°$

(b) $\phi = 50°$

(c) $\phi = 70°$

(d) $\phi = 90°$

(e) $\phi = 110°$

(f) $\phi = 130°$
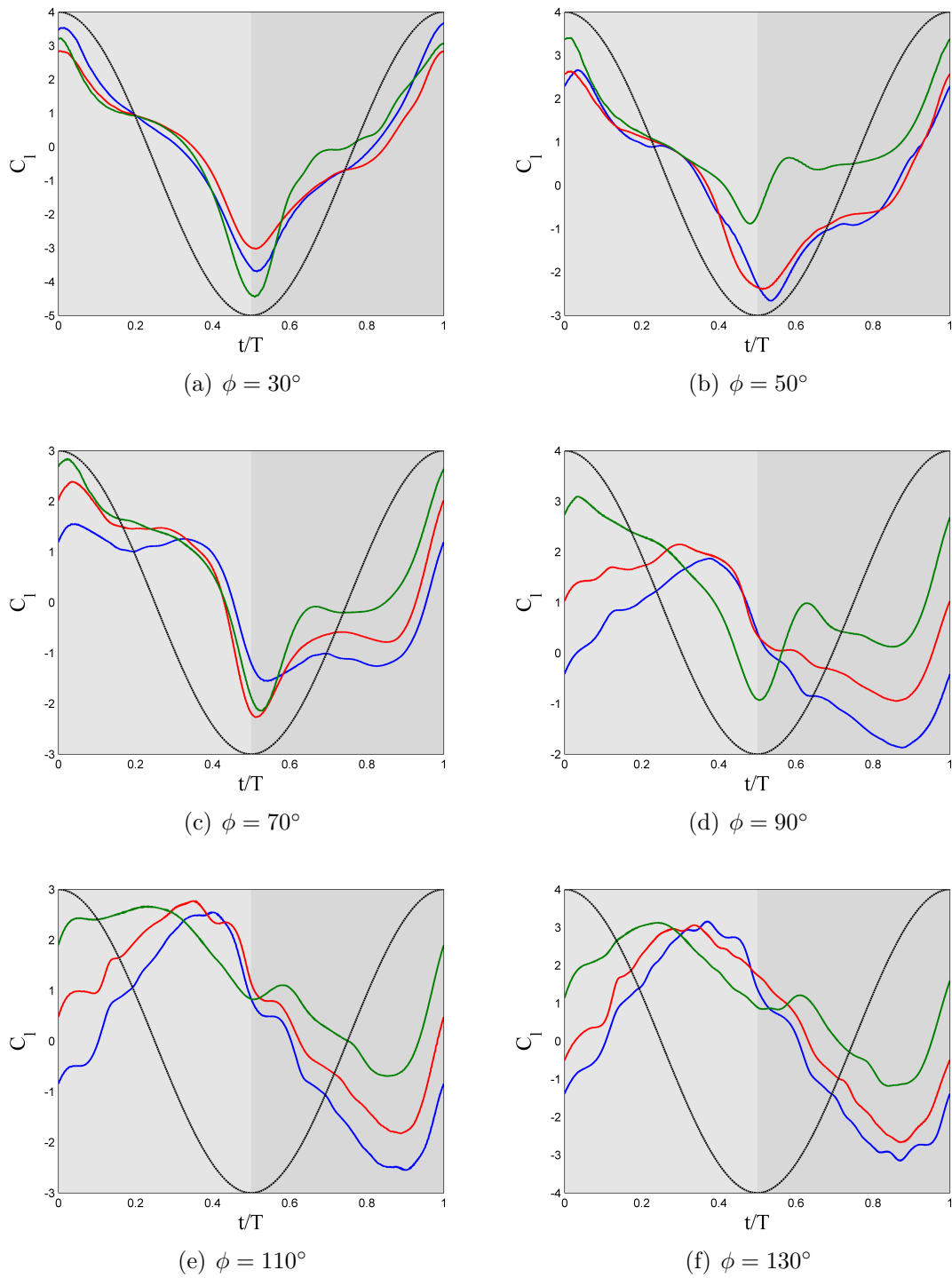
Figure 3.10: C_l with same ϕ and varying θ_m. $\theta_m = 0°$ (——), $\theta_m = 10°$ (——) and $\theta_m = 20°$ (——)

Figure 3.11 shows the change of C_d when θ_m varies and ϕ is constant.

(a) $\phi = 30°$

(b) $\phi = 50°$

(c) $\phi = 70°$

(d) $\phi = 90°$

(e) $\phi = 110°$

(f) $\phi = 130°$
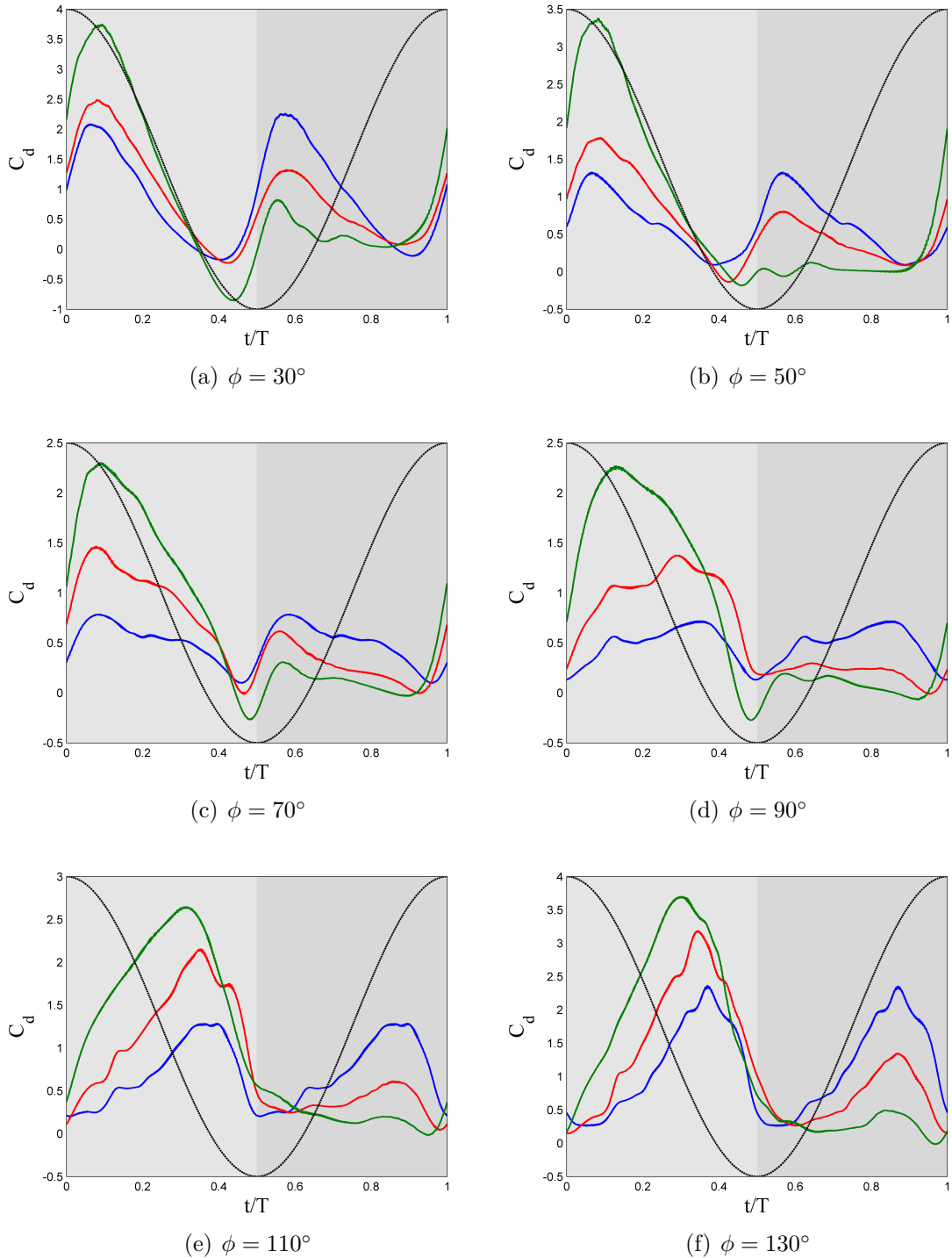
Figure 3.11: C_d with same ϕ and varying θ_m. $\theta_m = 0°$ (——), $\theta_m = 10°$ (——) and $\theta_m = 20°$ (——)

In *figure 3.12* is pictured the change of α_{eff} when θ_m varies and ϕ is constant.

(a) $\phi = 30°$

(b) $\phi = 50°$

(c) $\phi = 70°$

(d) $\phi = 90°$

(e) $\phi = 110°$

(f) $\phi = 130°$
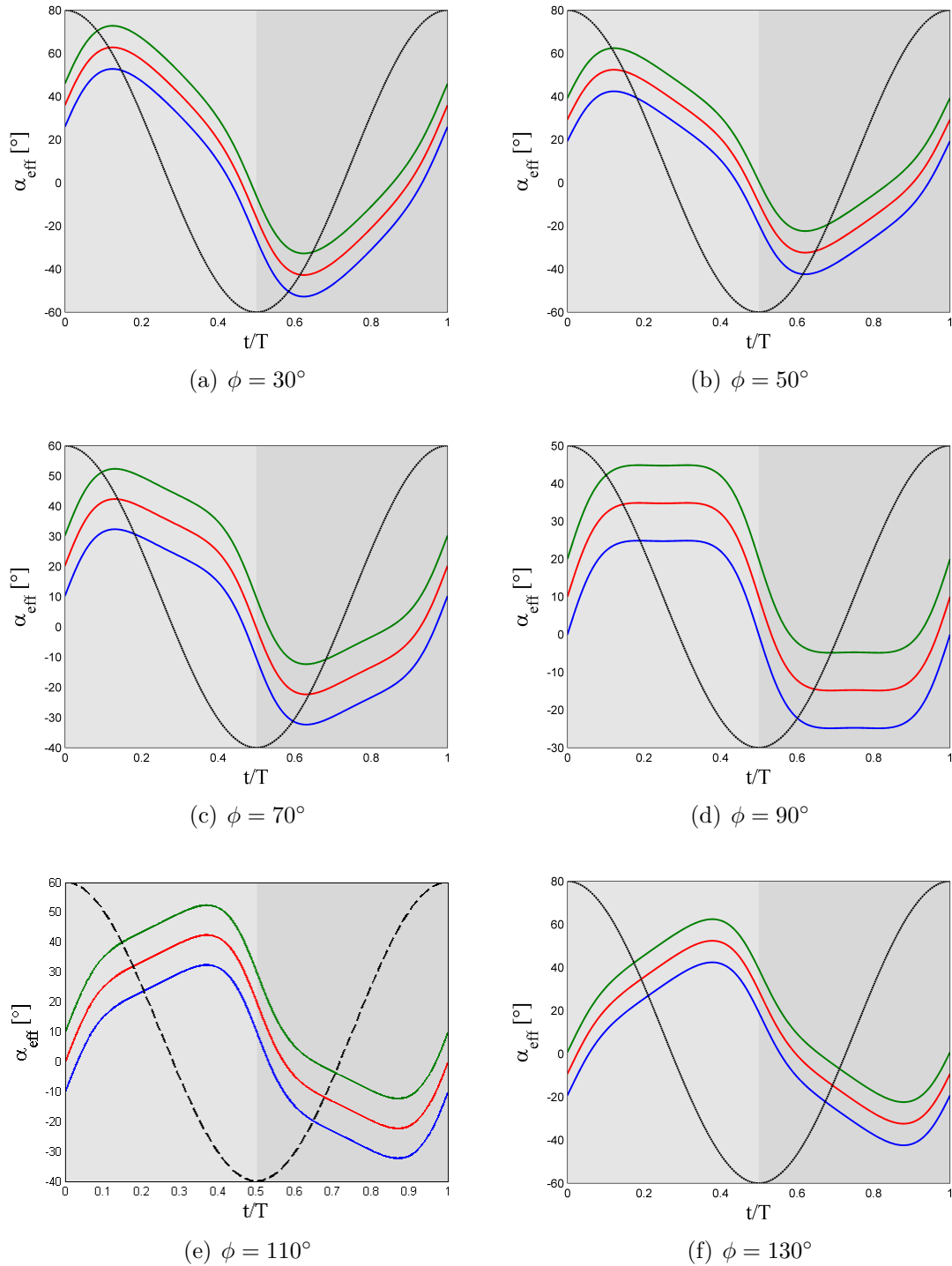
Figure 3.12: α_{eff} with same ϕ and varying θ_m. $\theta_m = 0°$ (——), $\theta_m = 10°$ (——) and $\theta_m = 20°$ (——)

3.2.2 C_l and C_d models description and models selection

Once the lift and drag coefficients of the DNS database have been determined, it can be proceed to obtain the models for them in order to have the inputs for the predicted aerodynamic model, as it was mentioned.

So as to choose the most suitable model, it is going to be studied the average value, the maximum value and the standard deviation of the absolute value of the difference between the model and the data obtained for all the cases.

They are going to be studied two models for C_l and for each one, two models of C_d are proposed.

- $C_l = 2\pi\alpha_{eff} \longrightarrow C_d = K_1 + K_2\ C_l^2$
  $$\longrightarrow C_d = K_1 + K_2\ \alpha_{eff}^2$$
- $C_l \equiv constant \longrightarrow C_d = K_1 + K_2\ C_l^2$
  $$\longrightarrow C_d = K_1 + K_2\ \alpha_{eff}^2$$

3.2.2.1 $C_l = 2\pi\alpha_{eff}$

This first model assumes that the lift coefficient increases linearly with the effective angle of attack.

Figure 3.13 illustrates the comparison between the C_l of MAS 1003 with respect to the proposed model.
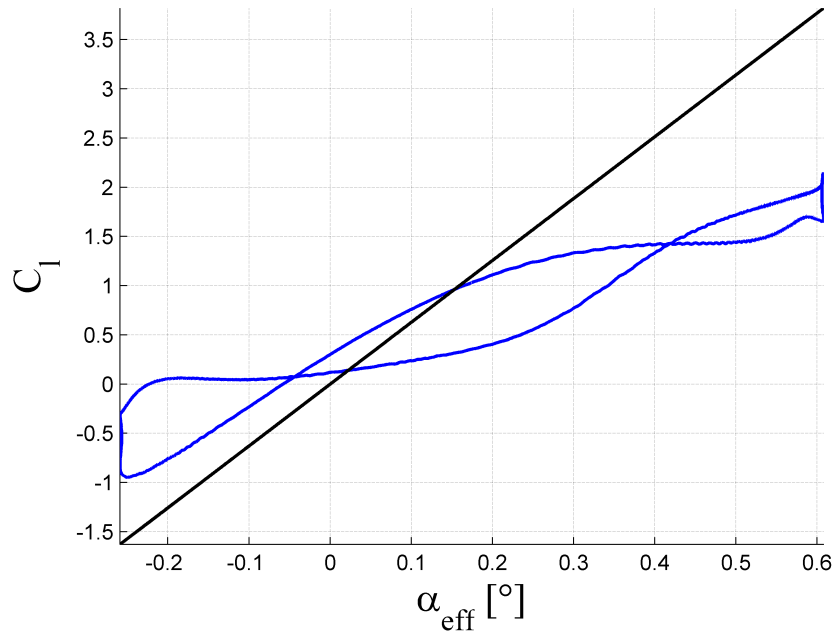
Figure 3.13: C_l comparison for $C_{l_{model}} = 2\pi\alpha_{eff}$. MAS 1003 (———) and model (———)

Moreover, in *table 3.2* the mean value, the maximum value and the standard deviation of the absolute value of the difference between the model and each case ($\epsilon = |C_{l_{model}} - C_{l_{MAS}}|$) are shown.

MAS	ϵ_{avg}	ϵ_{max}	σ
0000	2.8717	4.3692	1.1511
0001	2.0274	3.3584	0.9329
0002	1.3310	2.4357	0.7453
0003	1.1486	1.9033	0.5744
0004	1.0629	1.7420	0.4037
0005	1.1770	1.7561	0.3694
1000	2.8170	5.6469	1.5877
1001	2.1693	4.3934	1.2936
1002	1.5475	3.0989	0.9614
1003	1.2219	2.1730	0.5955
1004	1.1270	2.1814	0.5510
1005	1.3531	3.2126	0.8027
2000	3.4734	6.8510	2.0693
2001	2.6398	5.2849	1.6268
2002	1.9613	4.0495	1.4902
2003	1.7974	3.8750	1.1901
2004	1.5701	3.9516	1.1789
2005	1.9592	5.0079	1.4284

Table 3.2: Statistics $C_l = 2\pi\alpha_{eff}$

Regarding the drag coefficient, two parabolic models are proposed, one depends on C_l^2 and the other on α_{eff}^2. Due to the fact that this model of C_l depends linearly with α_{eff}, the two models proposed for C_d coincide. Therefore, there is a unique model for C_d, ($C_d = K_1 + K_2 \, \alpha_{eff}^2$).

In order to calculate the constants K_1 and K_2 a least-square curve fitting has been used. In the following table (*table 3.3*) the constants for each simulation are shown.

MAS	K_1	K_2	MAS	K_1	K_2
0000	-0.0584	2.3223	1003	0.0788	3.0640
0001	0.1579	1.7882	1004	0.1313	3.3893
0002	0.2105	1.6841	1005	0.1991	3.2622
0003	0.1436	2.4975	2000	-0.2487	2.1473
0004	0.1181	3.5312	2001	-0.1763	2.5584
0005	0.1851	3.6427	2002	-0.0128	2.5237
1000	0.0476	1.8188	2003	0.0191	2.8571
1001	0.0877	1.8768	2004	0.1749	2.8067
1002	0.1156	2.3389	2005	0.1874	2.7452

Table 3.3: Constants K_1 and K_2 for $C_{d_{model}} = K_1 + K_2\ \alpha_{eff}^2$

In *figure 3.14* the comparison between the C_d of the model and the simulation, MAS 1003, can be seen.
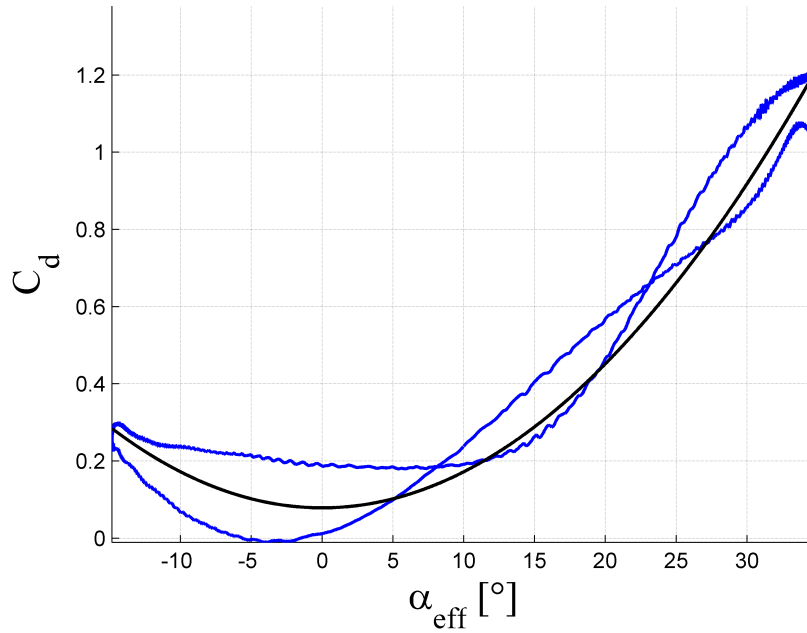
Figure 3.14: C_d comparison for $C_{d_{model}} = K_1 + K_2\ \alpha_{eff}$. MAS 1003 (──) and model (──)

As well as for the model of the lift coefficient, the mean value, the maximum value and the standard deviation of the absolute value between the model and each case is going to be determined ($\epsilon = |C_{d_{model}} - C_{d_{MAS}}|$). These values are presented in *table 3.4*.

MAS	ϵ_{avg}	ϵ_{max}	σ
0000	0.3341	0.9030	0.2166
0001	0.1628	0.4632	0.1106
0002	0.0697	0.1960	0.0516
0003	0.0546	0.1278	0.0373
0004	0.0583	0.1306	0.0356
0005	0.0666	0.1970	0.0407
1000	0.2809	0.7133	0.2018
1001	0.1663	0.4809	0.1315
1002	0.1254	0.4225	0.1014
1003	0.0724	0.1705	0.0438
1004	0.0826	0.2000	0.0487
1005	0.1128	0.3979	0.0980
2000	0.5022	1.2784	0.3295
2001	0.3413	1.2059	0.2878
2002	0.1988	0.6215	0.1760
2003	0.3069	1.0760	0.2941
2004	0.2418	0.7920	0.1900
2005	0.3694	1.2787	0.3369

Table 3.4: Statistics $C_d = K_1 + K_2 \; \alpha_{eff}^2$

3.2.2.2 $C_l \equiv constant$

The second proposed model for the lift coefficient is a C_l constant, but there will be a constant value for the period of time when the effective angle of attack is positive and another when it is negative.

This has been assumed because it is expected the same behaviour of C_l during these periods of time, a positive value for the lift coefficient is expected when $\alpha_{eff} > 0$ and a negative value when $\alpha_{eff} < 0$. These values are going to be determined for each simulation by the mean value of C_l in those periods.

Table 3.5 shows the found values for the period when $\alpha_{eff} > 0$ or $\alpha_{eff} < 0$ that have each simulation. Notice that for the cases that have a mean pitch value equals to 0°, the value of C_l when the effective angle of attack is positive is equal but opposite sing than the value when $\alpha_{eff} < 0$ ($C_{l_{\alpha_{eff}>0}} = -C_{l_{\alpha_{eff}<0}}$). This is not exactly fulfilled in MAS 0000 due to the fact that this case in non-periodic. Although for other cases where $\theta_m = 0°$ there is a difference between the absolute values, this difference can be considered negligible.

MAS	$C_{l_{\alpha_{eff}>0}}$	$C_{l_{\alpha_{eff}<0}}$	MAS	$C_{l_{\alpha_{eff}>0}}$	$C_{l_{\alpha_{eff}<0}}$
0000	1.1724	-1.2003	1003	1.5176	-0.4222
0001	1.0380	-1.0380	1004	1.7741	-0.8243
0002	1.0837	-1.0837	1005	1.8819	-1.3698
0003	1.0606	-1.0605	2000	0.7028	-1.1206
0004	1.3342	-1.3342	2001	1.2302	0.4301
0005	1.7616	-1.7557	2002	1.0482	-0.4752
1000	0.9179	-1.2834	2003	1.4754	0.4604
1001	0.8822	-1.1061	2004	1.8652	-0.1318
1002	1.1239	-0.9586	2005	1.9462	-0.3611

Table 3.5: Constants $C_{l_{\alpha_{eff}>0}}$ and $C_{l_{\alpha_{eff}<0}}$ for $C_{L_{model}} \equiv constant$

In *figure 3.15* it can be seen the difference between the model and the C_l of one simulation, MAS 1003.
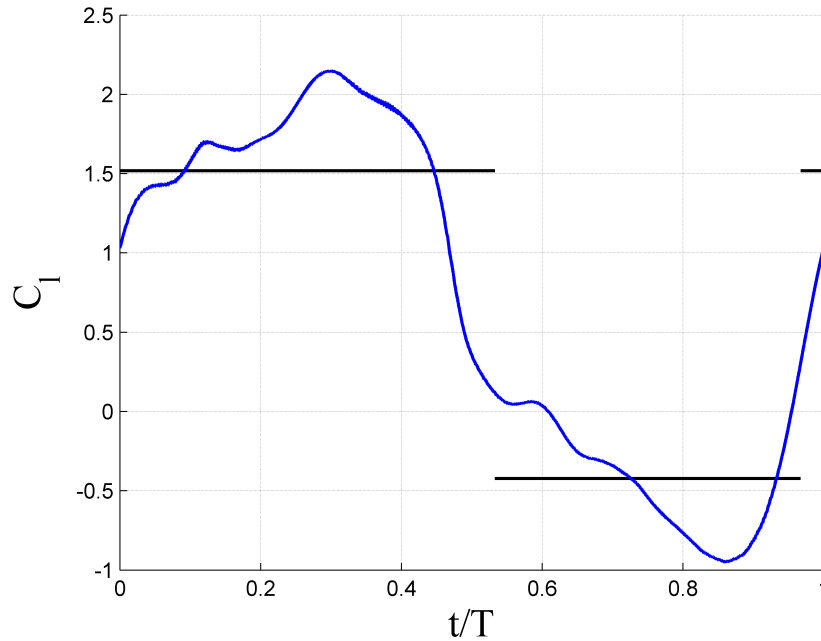
Figure 3.15: C_l comparison for $C_{l_{model}} \equiv constant$. MAS 1003 (——) and model (——)

Besides, as previously done for the models of C_l and C_d that has been explained, some statistical values must be calculated in order to choose the most suitable model. They are presented in *table 3.6*.

MAS	ϵ_{avg}	ϵ_{max}	σ
0000	1.3436	3.5099	0.8684
0001	0.7841	2.2264	0.6258
0002	0.2356	1.4886	0.2696
0003	0.5109	1.4735	0.3326
0004	0.8422	1.8409	0.5025
0005	0.9591	2.4562	0.5575
1000	0.9477	3.2984	0.7068
1001	0.7887	3.0843	0.6708
1002	0.6122	3.2991	0.6011
1003	0.3669	1.3962	0.2823
1004	0.6395	1.5732	0.3378
1005	0.7939	2.1082	0.4700
2000	1.3487	4.8777	1.0689
2001	0.6428	2.1741	0.6598
2002	0.7792	3.1902	0.7089
2003	0.7632	2.4086	0.6552
2004	0.5565	1.3187	0.2779
2005	0.6532	1.8991	0.3834

Table 3.6: Statistics $C_l \equiv constant$

Concerning the C_d, the two proposed possibilities for its model must be studied. The model for C_d proportional to α_{eff}^2 coincides with the explained in *section 3.2.2.1*. Therefore, the constants K_1 and K_2 are the presented in *table 3.3* and the statistics found for this model are shown in *table 3.4*.

Regarding the model for the drag coefficient proportional to C_l^2, the first step to be performed is the calculation of the constants K_1 and K_2. So as to, as it was done for C_d proportional to α_{eff}^2, a least square curve fitting has been used. These constants are shown in next table (*table 3.7*).

MAS	K_1	K_2	MAS	K_1	K_2
0000	-1.9096	1.9851	1003	0.1517	0.3149
0001	0.3355	0.2700	1004	0.1559	0.3102
0002	0.2910	0.1722	1005	-0.2626	0.5006
0003	0.3169	0.1461	2000	1.8910	-1.2951
0004	0.3930	0.1786	2001	-0.1383	0.8893
0005	0.7387	0.1296	2002	-0.0683	0.9586
1000	1.3681	-0.4404	2003	-0.0280	0.5161
1001	1.4527	-0.8423	2004	0.1322	0.3602
1002	-1.0518	1.4628	2005	0.2078	0.4063

Table 3.7: Constants K_1 and K_2 for $C_{d_{model}} = K_1 + K_2 \, C_l^2$

Due to the fact that the model assumes that C_d is proportional to C_l^2 and C_l is constant, C_d will also be. It will take two different values, when $\alpha_{eff} > 0$ and when $\alpha_{eff} < 0$, since it has been used the values of C_l shown in *table 3.5*. The values obtained for C_d are presented in *table 3.8*.

MAS	$C_{d_{\alpha_{eff}>0}}$	$C_{d_{\alpha_{eff}<0}}$	MAS	$C_{d_{\alpha_{eff}>0}}$	$C_{d_{\alpha_{eff}<0}}$
0000	0.8192	0.9506	1003	0.8771	0.2079
0001	0.6264	0.6264	1004	1.1323	0.3667
0002	0.4932	0.4932	1005	1.5103	0.6767
0003	0.4812	0.4812	2000	1.2513	0.2646
0004	0.7109	0.7109	2001	1.2076	0.0262
0005	1.1408	1.1381	2002	0.9850	0.1482
1000	0.9971	0.6427	2003	1.0955	0.0814
1001	0.7972	0.4223	2004	1.3853	0.1385
1002	0.7958	0.2923	2005	1.7465	0.2608

Table 3.8: Constants $C_{d_{\alpha_{eff}>0}}$ and $C_{d_{\alpha_{eff}<0}}$ for $C_{d_{model}} = K_1 + K_2\,C_l^2$

Furthermore, *figure 3.16* illustrates the differences between the drag coefficient of the model and the C_d of MAS 1003.
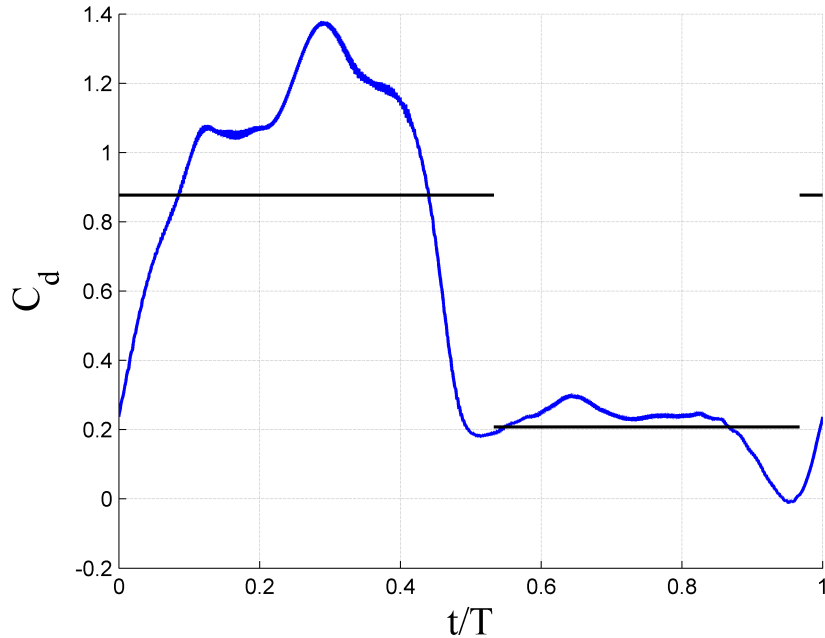
Figure 3.16: C_d comparison for $C_{d_{model}} = K_1 + K_2\,C_l^2$. MAS 1003 (——) and model (——)

Once again, the maximum value, the mean value and the standard deviation of the absolute value of the difference between the model and the simulation is calculated. They are shown in *table 3.9*.

MAS	ϵ_{avg}	ϵ_{max}	σ
0000	0.7042	1.3146	0.3627
0001	0.3307	0.7049	0.2061
0002	0.1586	0.3947	0.1138
0003	0.1456	0.3503	0.0970
0004	0.3285	0.5805	0.1768
0005	0.6221	1.2275	0.2975
1000	0.6195	1.4955	0.3986
1001	0.4048	0.9944	0.2894
1002	0.2917	0.8098	0.2230
1003	0.2161	0.8651	0.2110
1004	0.3631	1.0241	0.3044
1005	0.6222	1.6787	0.4257
2000	0.9115	2.5000	0.7876
2001	0.7107	2.1757	0.6696
2002	0.5438	1.3196	0.4610
2003	0.5585	1.3708	0.4594
2004	0.5322	1.3487	0.4510
2005	0.7605	1.9582	0.6364

Table 3.9: Statistics $C_d = K_1 + K_2 \, C_l^2$

3.2.2.3 Model selection for C_l and C_d

In order to select the model for the lift coefficient, *tables 3.2* and *3.6* must be compared.

The maximum value of ϵ_{avg} is not greater than 2 for the model of $C_l \equiv constant$, whereas for $C_l = 2\pi\alpha_{eff}$, it goes up to 3.5. Moreover, ϵ_{max} achieves a greater maximum value when the lift coefficient is proportional to α_{eff} than when it is constant. These two facts indicate that, in principle, the most suitable model is $C_l \equiv constant$.

The standard deviation should be also studied. It is a measure of the amount of dispersion of a set of data. If the standard deviation is closed to 0, it means that the data is closed to the expected value. Since the simulations of the model of constant lift coefficient have lower standard deviation, values closer to 0, it can be concluded that it is the best model.

Following the same line of thought to choose the model for the drag coefficient, it can be concluded that the most suitable model is $C_d = K_1 + K_2 \, \alpha_{eff}^2$.

In *table 3.10* the selected models have been remarked.

Lift coefficient (C_l)	Drag coefficient (C_d)
Constant	$K_1 + K_2\ \alpha_{eff}^2$

Table 3.10: Selected models

3.2.3 Aerodynamic efficiency (E) models description and selection

Once the models of the lift and drag coefficient have been chosen, the aerodynamic efficiency ($E = C_l/C_d$) can be obtained. It is, in fact, the parameter that must be found since the input needed for the new predicted aerodynamic model is $\chi = atan\left(\frac{1}{E}\right)$.

The aerodynamic efficiency is going to be defined positive when the forces have its expected sing:

For α_{eff} positive, lift and drag are expected to be positive. So that, E is defined positive when both are. On the other hand, for negative values of α_{eff}, E is considered to be positive when C_l is negative and C_d positive.

To have a reference for the aerodynamic efficiency, the C_l obtained for each MAS has been divided by the C_d. Due to the fact that C_d reaches 0 in some cases, E goes to infinity. Therefore, a cut off value for the drag coefficient has been assumed. In absolute terms, the drag coefficient cannot be smaller than one fifth of the lift coefficient ($|C_d| \leq 0.2|C_l|$) .

So as to, two models are proposed.

- $E \equiv constant = C_{l_{const}}/C_{d_{const}}$.

- $E = C_{l_{const}}/C_{d_{\propto\alpha_{eff}^2}}$

3.2.3.1 $E \equiv constant$

Two constant values for the aerodynamic efficiency are calculated, for α_{eff} positive and for α_{eff} negative.

The values of C_l used to calculate E are the presented in *table 3.5*. Moreover, the constant values of C_d are found by doing the average of the drag coefficient of the model selected ($C_d \propto \alpha_{eff}^2$) for the two conditions of the effective angle of attack. If the value of C_d obtained is smaller than the cut off value, then the assigned value is the cut off value ($0.2 * |C_l|$), indeed, it is being assumed that the maximum absolute value for the aerodynamic efficiency is 5. The results are presented in *table 3.11*.

MAS	$C_{d_{\alpha_{eff}>0}}$	$C_{d_{\alpha_{eff}<0}}$	MAS	$C_{d_{\alpha_{eff}>0}}$	$C_{d_{\alpha_{eff}<0}}$
0000	0.8849	0.8849	1003	0.8595	0.2307
0001	0.6264	0.6264	1004	1.1172	0.3868
0002	0.4932	0.4932	1005	1.4978	0.6934
0003	0.4812	0.4812	2000	1.3516	0.2241
0004	0.7109	0.7109	2001	1.2156	0.0860
0005	1.1394	1.1394	2002	1.0350	0.0950
1000	1.0798	0.5367	2003	1.1194	0.0921
1001	0.8349	0.3721	2004	1.3402	0.2351
1002	0.7960	0.2919	2005	1.6809	0.3881

Table 3.11: $C_{d_{\alpha_{eff}>0}}$ and $C_{d_{\alpha_{eff}<0}}$ coming from the average of $C_{d_{\propto\alpha_{eff}^2}}$

Therefore, the values of the aerodynamic efficiency can be obtained and they are shown in *table 3.12*.

MAS	$E_{\alpha_{eff}>0}$	$E_{\alpha_{eff}<0}$	MAS	$E_{\alpha_{eff}>0}$	$E_{\alpha_{eff}<0}$
0000	1.3250	1.3565	1003	1.7657	1.8295
0001	1.6571	1.6571	1004	1.5879	2.1314
0002	2.1974	2.1974	1005	1.2564	1.9755
0003	2.2041	2.2041	2000	0.5200	5.0000
0004	1.8768	1.8769	2001	1.0121	-5.0000
0005	1.5460	1.5409	2002	1.0128	5.0000
1000	0.8500	2.3915	2003	1.3180	-5.0000
1001	1.0567	2.9724	2004	1.3917	0.5609
1002	1.4118	3.2835	2005	1.1578	0.9306

Table 3.12: $E \equiv constant$

In *figure 3.17* can be seen how the model predicts the aerodynamic efficiency of MAS 1003.
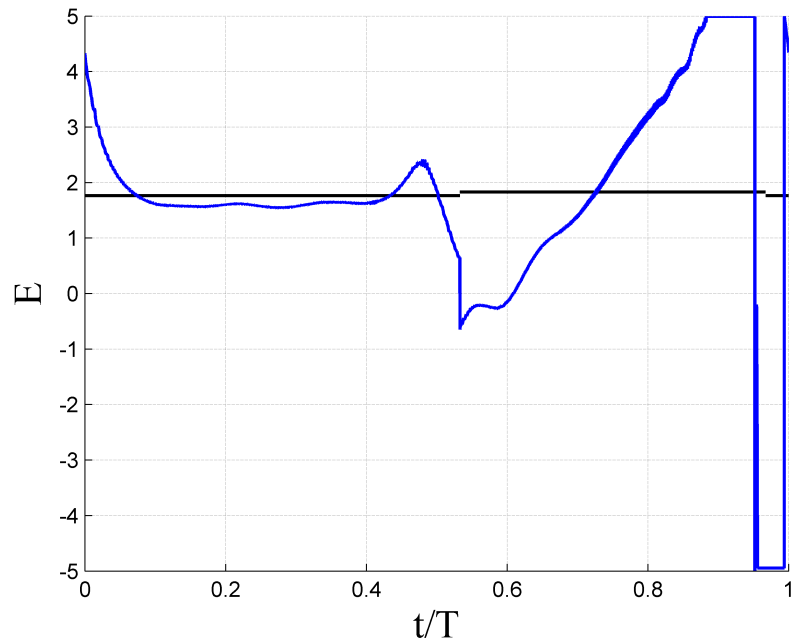
Figure 3.17: *E* comparison for $E \equiv constant$. MAS 1003 (——) and model (——)

As done with the models for the lift and drag coefficients, the mean and maximum values, as well as, the standard deviation of signal $|E_{model} - E_{MAS}|$ are going to be studied. They are shown in *table 3.13*.

MAS	ϵ_{avg}	ϵ_{max}	σ
0000	2.3586	6.2668	2.5247
0001	1.8143	6.5562	2.4930
0002	0.7009	5.8684	0.8169
0003	1.0143	5.2901	0.9890
0004	0.9113	4.0487	1.1861
0005	0.6990	4.2387	0.9836
1000	2.0409	7.3827	2.4479
1001	1.8084	7.9694	2.4068
1002	1.3575	7.9750	1.9428
1003	1.1489	6.8181	1.4968
1004	0.8834	6.4412	1.1794
1005	0.5762	4.7737	0.7882
2000	3.2507	9.9905	3.2022
2001	1.4484	9.8110	2.2208
2002	2.2530	9.9862	2.4085
2003	1.3858	6.3012	2.0268
2004	1.4401	5.8492	1.5408
2005	1.3630	5.9595	1.5008

Table 3.13: Statistics $E \equiv constant$

3.2.3.2 $\quad E = C_{l_{const}}/C_{d_{\propto \alpha^2_{eff}}}$

In this model the same assumption that was performed to achieve the aerodynamic efficiency for the simulations is going to be done, once again, to avoid that E reaches infinity.

Figure 3.18 illustrated how the model differs from the simulation, MAS 1003.
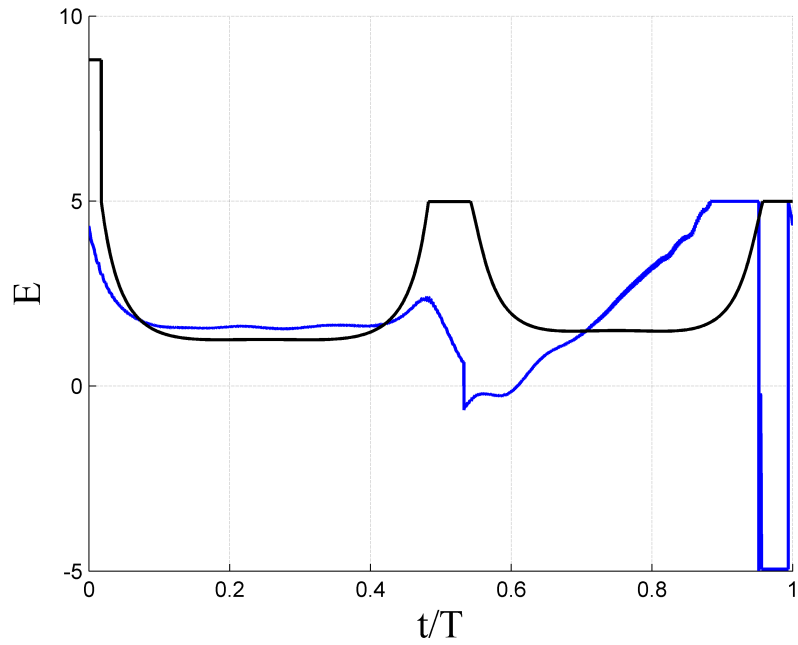
Figure 3.18: *E* comparison for $E = C_{l_{const}}/C_{d_{\propto \alpha^2_{eff}}}$. MAS 1003 (——) and model (——)

Table 3.14 presents the values of the studied parameters for the difference between the model and the MAS.

MAS	ϵ_{avg}	ϵ_{max}	σ
0000	3.3840	9.9061	4.1767
0001	2.5750	9.8978	3.7013
0002	0.4911	8.6689	1.2603
0003	1.2364	10.4740	1.8162
0004	1.7464	7.9388	2.1233
0005	1.4426	7.6841	1.9335
1000	2.7909	9.9847	3.8322
1001	2.5247	9.9928	3.5440
1002	1.4963	9.6836	2.9782
1003	1.6248	9.9418	2.1645
1004	1.5884	10.5870	1.8297
1005	1.3146	7.7858	1.5569
2000	2.1481	9.9887	2.9377
2001	1.6689	9.9921	2.4918
2002	2.2963	9.9635	2.9549
2003	4.8710	9.9946	4.4489
2004	1.4489	5.2112	1.5724
2005	1.3295	7.7220	1.8436

Table 3.14: Statistics $E = C_{l_{const}}/C_{d_{\propto \alpha^2_{eff}}}$

3.2.3.3 Model selection for E

For selecting the model, *tables 3.13 and 3.14* must be compared.

Both models have maximum values of ϵ quite high. Moreover, the average and the standard deviation values are not as good as the obtained for the models of the lift and drag coefficients. In principle, the best model for the aerodynamic efficiency is $E \equiv constant$.

Due to the fact that the results are not as suitable as expected, both models for the aerodynamic efficiency are going to be introduced in the new predicted aerodynamic model and then, based on the predictions that they will give, the most reliable model for the aerodynamic efficiency will be chosen.

RESULTS

In this chapter the most relevant results obtained from each of the options of the new predicted aerodynamic model are going to be commented.

4.1 Option 1 results

Firstly, it must be mention that the time needed to calculate the forces along a period is around 1.6 seconds.

In order to see how well the model predicts the forces in comparison with the database, some parameters must be studied as it was done in SECTION X to choose the most suitable model for lift and drag coefficient. Defining the error as $\epsilon = |C_{\hat{F}_{NPAM}} - C_{\hat{F}_{MAS}}|$, the parameters to evaluate the performance of NPAM are the mean and maximum value and the standard deviation.

The variables that are going to be compared with the results obtained from the simulations are the thrust coefficient ($C_t = -\frac{F_x}{\frac{1}{2}\rho U_\infty^2 c}$) and the coefficient of forces in z-direction ($C_z = \frac{F_z}{\frac{1}{2}\rho U_\infty^2 c}$). From *table 4.1* to *4.4* these results are presented.

Table 4.1 show the parameters that evaluate the accuracy of the model for C_t when the input aerodynamic efficiency is a constant.

Case	ϵ_{avg}	ϵ_{max}	σ
0000	2.4846	6.7120	1.5288
0001	0.4578	0.9451	0.2389
0002	0.1952	0.8151	0.1506
0003	0.4890	0.8397	0.2044
0004	0.7038	1.5737	0.3536
0005	0.9461	3.8789	0.8921
1000	8.1510	26.1218	5.9156
1001	0.4351	0.8084	0.2048
1002	0.2430	1.5248	0.2417
1003	0.3590	0.9205	0.2337
1004	0.5894	1.3678	0.3569
1005	1.0530	3.8593	0.6733
2000	1.2508	3.4601	0.7629
2001	2.8902	8.4688	1.8307
2002	0.5124	1.1489	0.3584
2003	0.7473	2.1891	0.6222
2004	2.0740	5.1905	1.4133
2005	0.8512	2.5762	0.7160

Table 4.1: Statistics of C_t when $E \equiv constant$

In *table 4.2* presents the parameters specified before for the same input aerodynamic efficient than *4.1* but for the C_z.

Case	ϵ_{avg}	ϵ_{max}	σ
0000	10.5505	15.5820	3.6959
0001	1.8610	3.0448	0.7845
0002	0.4907	2.0350	0.4162
0003	1.0462	2.2044	0.7098
0004	1.8521	4.0910	1.3683
0005	3.6029	6.9947	2.3240
1000	26.2422	50.1993	12.4233
1001	1.8984	3.6625	0.9675
1002	1.0030	3.4453	0.6332
1003	1.2534	2.4642	0.7103
1004	1.4709	3.3361	0.9377
1005	2.5447	6.2649	1.8670
2000	2.9360	7.3978	2.2147
2001	8.2828	20.0945	6.3558
2002	2.6110	7.1177	2.2278
2003	2.9890	9.2634	3.1781
2004	6.9659	16.5992	4.7462
2005	2.1963	8.4620	2.4860

Table 4.2: Statistics of C_z when $E \equiv constant$

Tables 4.3 and *4.4* present the parameters that measure the accuracy of the new predicted aerodynamic model when the introduced aerodynamic to the model is $E = C_{l_{const}}/C_{d_{\propto \alpha_{eff}^2}}$.

Table 4.3 shows that parameters for C_t.

Case	ϵ_{avg}	ϵ_{max}	σ
0000	6.8937	11.5232	2.8220
0001	0.5712	1.1502	0.2810
0002	0.1374	0.4644	0.1113
0003	0.4374	0.8447	0.2421
0004	1.2436	2.1362	0.6201
0005	2.3878	4.0428	1.0408
1000	5.1855	11.6990	3.4076
1001	0.4824	1.0811	0.2597
1002	0.4711	0.9735	0.2729
1003	0.3743	0.7485	0.2162
1004	0.9357	1.9237	0.5630
1005	1.9248	3.5508	0.9273
2000	1.4634	3.3414	0.9820
2001	3.4077	8.2808	2.0623
2002	0.5808	1.2525	0.3607
2003	0.7327	2.1669	0.6109
2004	1.1878	3.3319	0.8854
2005	1.5849	4.1177	1.0895

Table 4.3: Statistics of C_t when $E = C_{l_{const}}/C_{d_{\propto \alpha^2_{eff}}}$

And *table 4.4* shows these results for C_x.

Case	ϵ_{avg}	ϵ_{max}	σ
0000	24.7512	44.2187	11.7067
0001	1.7188	2.8961	0.7198
0002	0.6417	1.9967	0.4314
0003	1.3881	2.3330	0.7462
0004	2.4970	3.8779	1.0679
0005	5.6341	7.6257	1.6221
1000	14.2226	34.2796	9.1052
1001	1.6168	2.7068	0.7967
1002	0.9343	3.5413	0.6460
1003	1.4228	3.3480	0.9833
1004	1.7768	3.3820	0.8053
1005	4.8729	8.3715	1.7464
2000	2.8404	5.9313	1.8651
2001	10.5182	30.5913	9.4820
2002	2.9665	8.1237	2.5154
2003	3.1402	9.9163	3.4493
2004	5.1831	14.1708	4.3147
2005	7.3665	21.5626	6.4125

Table 4.4: Statistics of C_z when $E = C_{l_{const}}/C_{d_{\propto \alpha_{eff}^2}}$

Let us analyse two different cases, one where the prediction of the model is in agreement with the results from the DNS, and another where the model falls to do a good prediction of the aerodynamic forces. The remainder cases are attached in *appendices B* and *C*.

It has been chosen a case in which the prediction of the aerodynamic forces are acceptable (0002) and a case in which they are not (2000).

In *figures 4.1* and *4.2* the comparison for the thrust coefficient C_t and C_z between the model and the results from the DNS is shown.

Figure 4.1 illustrates this comparison when the inpunt aerodynamic efficiency to the model is $E \equiv constant$.

(a) C_t (b) C_z

Figure 4.1: Comparison for case 0002 ($\theta_m = 0°$ and $\phi = 70°$) of C_t and C_z between the model and the DNS with $E \equiv constant$. Model (—), DNS (—) and the vertical position h of the airfoil (- - -)

Whereas *figure 4.2* pictures the comparison when $E = C_{l_{const}}/C_{d_{\propto \alpha^2_{eff}}}$.

(a) C_t (b) C_z

Figure 4.2: Comparison for case 0002 ($\theta_m = 0°$ and $\phi = 70°$) of C_t and C_z between the model and the DNS with $E = C_{l_{const}}/C_{d_{\propto \alpha^2_{eff}}}$. Model (—), DNS (—) and the vertical position h of the airfoil (- - -)

Figures 4.3 and *4.4* show the comparison for case 2000 of C_t and C_z between the new predicted aerodynamic model and the DNS. *Figure 4.3* illustrates the comparison when the aerodynamic efficiency used is $E \equiv constant$.
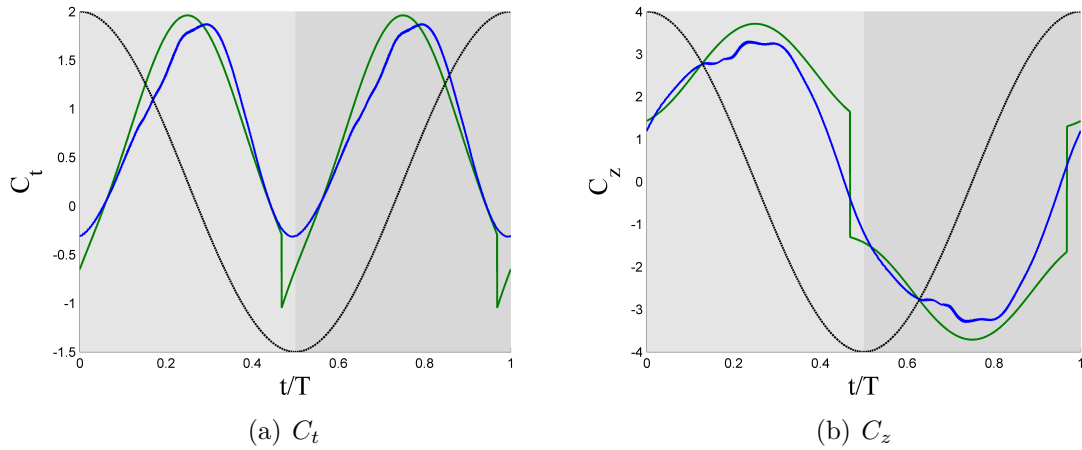
(a) C_t (b) C_z

Figure 4.3: Comparison for case 2000 ($\theta_m = 20°$ and $\phi = 30°$) of C_t and C_z between the model and the DNS with $E \equiv constant$. Model (——), DNS (——) and the vertical position h of the airfoil (- - -)

And in *figure 4.4* is pictured the comparison when the input aerodynamic efficiency is $E = C_{l_{const}}/C_{d_{\propto \alpha^2_{eff}}}$.

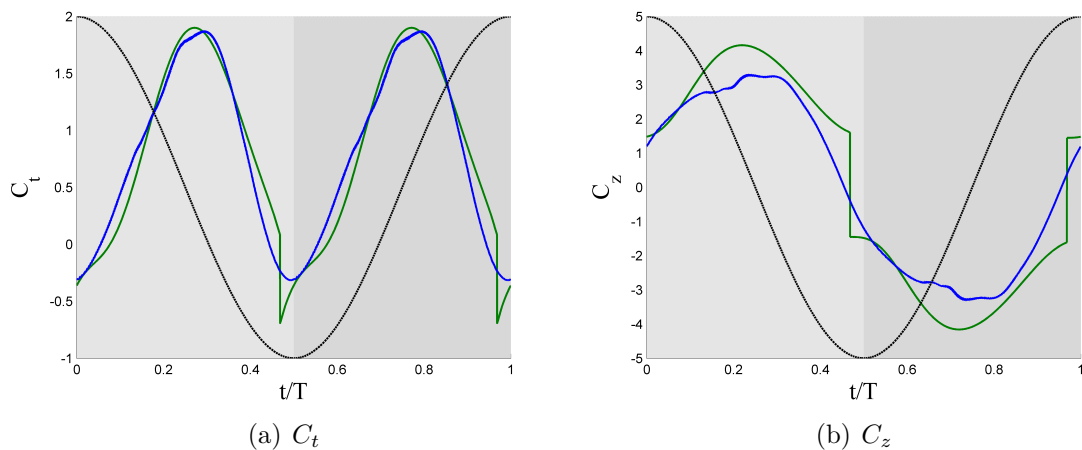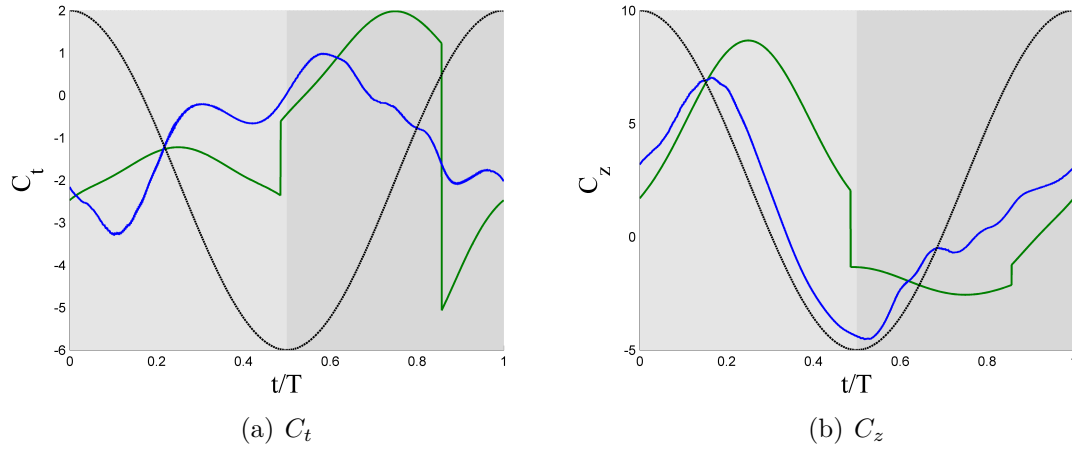(a) C_t (b) C_z
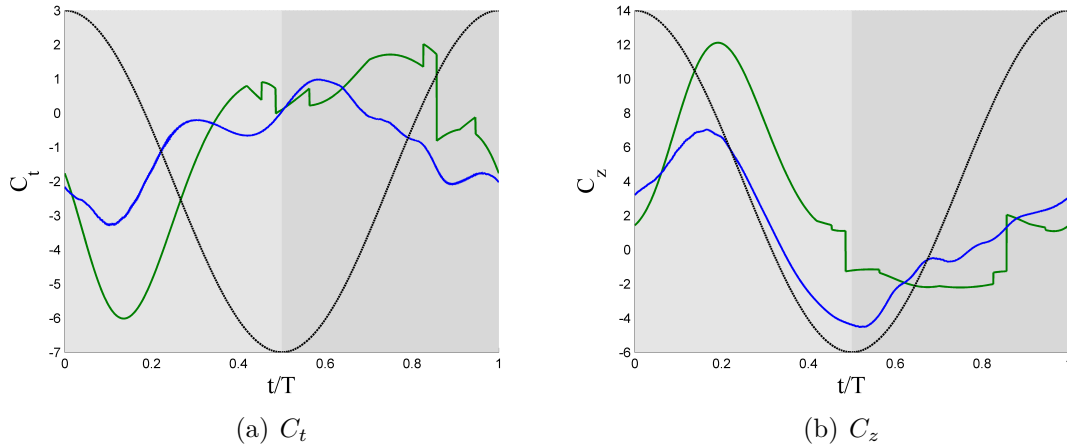
Figure 4.4: Comparison for case 2000 ($\theta_m = 20°$ and $\phi = 30°$) of C_t and C_z between the model and the DNS with $E = C_{l_{const}}/C_{d_{\propto \alpha^2_{eff}}}$. Model (——), DNS (——) and the vertical position h of the airfoil (- - -)

From *figure 4.1* to *4.3* it can be seen that for both C_t and C_z of the model there are two sudden changes. This occurs due to the change in sign of the effective angle of attack. However, in *figure 4.4* it can be seen more than 2 changes. These extra sudden changes are introduced by the fitting of the drag coefficient from the database. Due to the fact that one of the constant that were found to fit C_d for the

case 2000 is negative (see *table 3.3*), more changes a part from the corresponding to the change of sign of α_{eff} might appear.

4.2   Option 2 results

In this option it has been done an iteration in order to have as the output mean forces equal to the mean forces that are needed as input of the model to calculate the induced velocities. The time needed to calculate the forces is 2.9 seconds.

As well as for option 1, some statistics parameters that evaluate the performance of the NPAM are studied. These are presented from *table 4.5* to *table 4.8*.

Tables 4.5 and *4.6* show ϵ_{avg}, ϵ_{max} and σ when the input aerodynamic efficiency is $E \equiv constant$.

Table 4.5 presents these values for C_t.

MAS	ϵ_{avg}	ϵ_{max}	σ
0000	0.8383	1.7206	0.5064
0001	0.3783	1.1777	0.3496
0002	0.1626	0.6353	0.1254
0003	0.4835	1.0203	0.2779
0004	0.6825	1.3713	0.3490
0005	0.6512	1.6396	0.4407
1000	0.6016	1.8207	0.5268
1001	0.3839	1.4107	0.3631
1002	0.2904	1.7668	0.2908
1003	0.3733	1.3081	0.2933
1004	0.5807	1.8180	0.4122
1005	0.7716	2.8940	0.5175
2000	1.1256	3.1486	0.9153
2001	0.7034	2.8477	0.6830
2002	0.6423	3.4658	0.6243
2003	0.5521	2.2355	0.5443
2004	0.8250	4.1051	0.7079
2005	1.1640	4.6664	0.8445

Table 4.5: Statistics of C_t when $E \equiv constant$

In *table 4.6* the parameters are those for C_z.

MAS	ϵ_{avg}	ϵ_{max}	σ
0000	2.5001	4.7514	1.2297
0001	1.3250	2.8679	0.8623
0002	0.3547	1.7292	0.3487
0003	0.7825	1.5393	0.4760
0004	1.4815	2.6902	0.8236
0005	1.9882	3.7300	1.1581
1000	1.8735	3.9567	0.9482
1001	1.3898	3.5267	0.8349
1002	0.9996	3.3741	0.6365
1003	0.6528	2.1314	0.4987
1004	1.2106	3.2397	0.7551
1005	1.7551	4.8276	1.2544
2000	2.6714	5.2548	1.2324
2001	1.4490	3.1154	1.0430
2002	1.3264	3.1067	0.9070
2003	1.3557	3.4578	1.1373
2004	1.1351	3.9777	1.1337
2005	1.6088	6.2594	1.6609

Table 4.6: Statistics of C_z when $E \equiv constant$

The parameters that assess whether the model is accurate or not when the aerodynamic efficiency used is $E = C_{l_{const}}/C_{d_{\propto \alpha_{eff}^2}}$ are shown in *tables 4.7* and *4.8*.

Table 4.7 presents the parameters for C_t.

Case	ϵ_{avg}	ϵ_{max}	σ
0000	1.0582	2.7226	0.8204
0001	0.6215	1.7175	0.5095
0002	0.1537	0.3542	0.0938
0003	0.5083	1.2256	0.3838
0004	0.9907	2.0950	0.6284
0005	1.2296	2.4248	0.7507
1000	0.7188	2.2160	0.6008
1001	0.6203	1.5195	0.4032
1002	0.4515	1.0501	0.3069
1003	0.4700	1.2082	0.3409
1004	0.8030	1.8045	0.5580
1005	1.0791	2.3050	0.6857
2000	1.1201	3.8694	0.9206
2001	0.3991	1.6401	0.3405
2002	0.6467	2.1434	0.4326
2003	0.6202	1.4944	0.4029
2004	0.7563	2.8772	0.5377
2005	0.8485	2.5538	0.4957

Table 4.7: Statistics of C_t when $E = C_{l_{const}}/C_{d_{\propto \alpha^2_{eff}}}$

And *table 4.8* shows the parameters for C_z.

Case	ϵ_{avg}	ϵ_{max}	σ
0000	2.1180	4.2783	1.0048
0001	1.1379	2.5323	0.7116
0002	0.3406	1.6184	0.2941
0003	0.7335	1.5123	0.3997
0004	1.1371	2.1696	0.6193
0005	1.2974	2.9131	0.7325
1000	1.5152	3.5992	0.7972
1001	1.0932	3.1965	0.7636
1002	0.7987	3.3406	0.6218
1003	0.4690	1.4713	0.3623
1004	0.8445	1.8109	0.4428
1005	1.1363	2.7761	0.7400
2000	2.1021	4.9541	1.1517
2001	1.1724	2.4597	0.8364
2002	0.9804	3.3043	0.7347
2003	1.2173	2.4552	0.7962
2004	0.9396	2.2425	0.5557
2005	1.2632	4.1092	1.0323

Table 4.8: Statistics of C_z when $E = C_{l_{const}}/C_{d_{\propto \alpha^2_{eff}}}$

In the following figures two cases are going to be commented. The rest of the figures can be seen in *appendices D* and *E*.

Figures 4.5 and *4.6* illustrate, for case 0002, the comparison of the forces between the NPAM and the simulations.
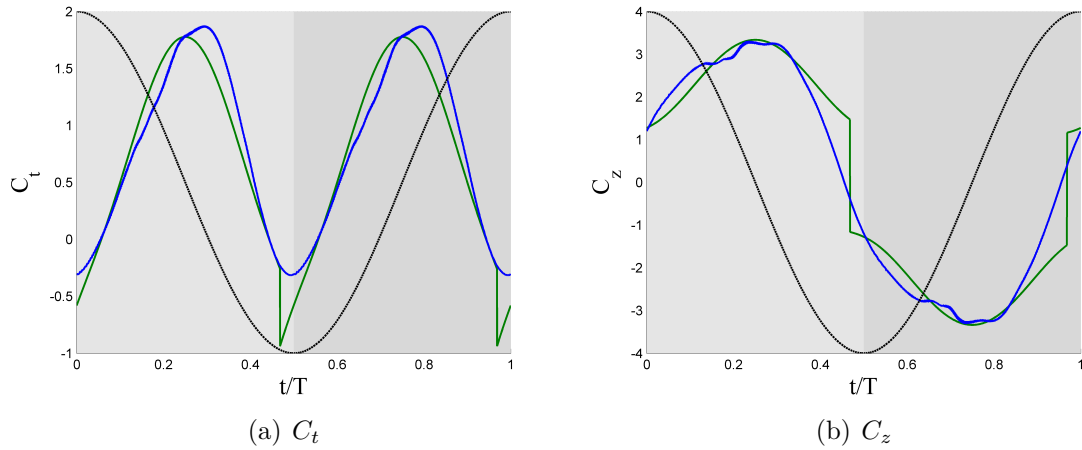
Figure 4.5 show the comparison when $E \equiv constant$.

(a) C_t (b) C_z

Figure 4.5: Comparison for case 0002 ($\theta_m = 0°$ and $\phi = 70°$) of C_t and C_z between the model and the DNS with $E \equiv constant$. Model (——), DNS (——) and the vertical position h of the airfoil (- - -)

Whereas, *figure 4.6* illustrates the comparison, for the same case than *figure 4.5*, but using the aerodynamic efficiency $E = C_{l_{const}} / C_{d_{\propto \alpha^2_{eff}}}$.
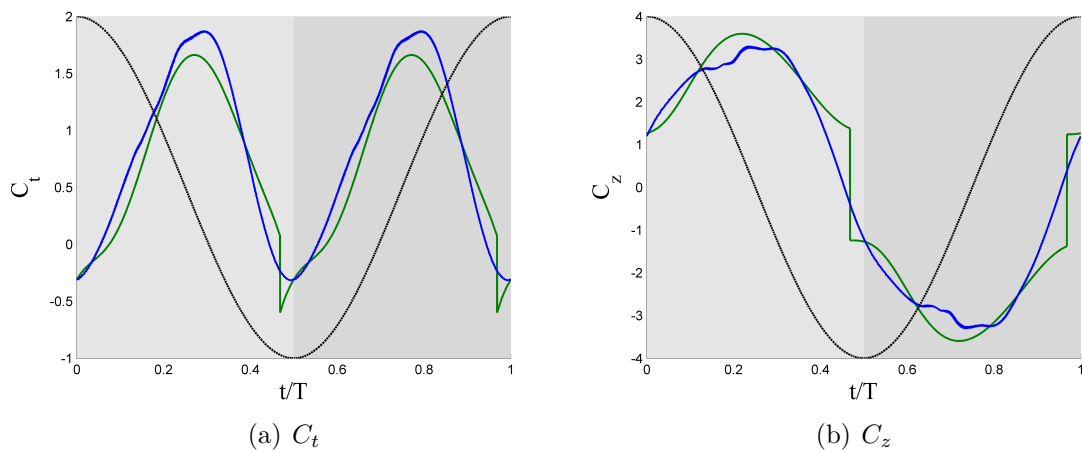

(a) C_t (b) C_z

Figure 4.6: Comparison for case 0002 ($\theta_m = 0°$ and $\phi = 70°$) of C_t and C_z between the model and the DNS with $E = C_{l_{const}} / C_{d_{\propto \alpha^2_{eff}}}$. Model (——), DNS (——) and the vertical position h of the airfoil (- - -)

In *figure 4.7* it can be seen the comparison of C_t and C_z between the NPAM and the results from the DNS for case 2000 when the aerodynamic efficiency used is $E \equiv constant$.

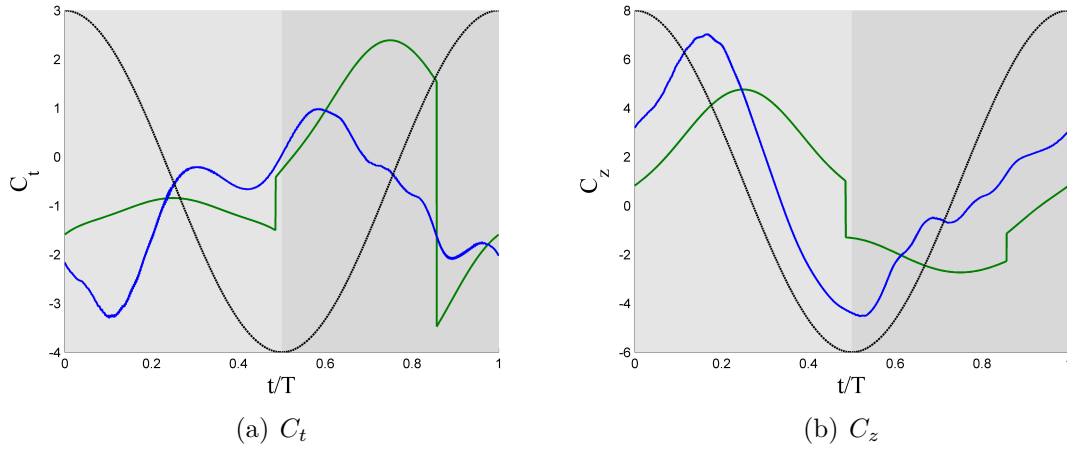(a) C_t (b) C_z

Figure 4.7: Comparison for case 2000 ($\theta_m = 20°$ and $\phi = 30°$) of C_t and C_z between the model and the DNS with $E \equiv constant$.Model (—), DNS (—) and the vertical position h of the airfoil (- - -)

On the other hand, *figure 4.8* shows for the same case than the illustrated in *figure 4.7*, but when$E = C_{l_{const}}/C_{d_{\propto \alpha^2_{eff}}}$ is used.
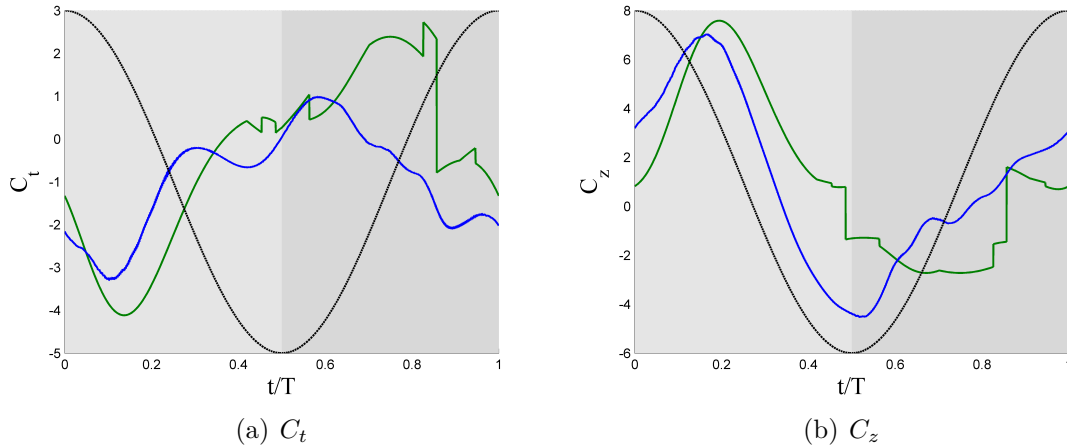

(a) C_t (b) C_z

Figure 4.8: Comparison for case 2000 ($\theta_m = 20°$ and $\phi = 30°$) of C_t and C_z between the model and the DNS with $E = C_{l_{const}}/C_{d_{\propto \alpha^2_{eff}}}$. Model (—), DNS (—) and the vertical position h of the airfoil (- - -)

Moreover, in these figures it is also seen the two sudden changes in the forces that are the result of the change of sign of α_{eff} which governs the sign of the angle χ and the sign of the lift coefficient (see *equations 2.38* and *2.39*). Besides, in *figure 4.8* the extra sudden changes introduced by the fitting of the drag coefficient from the database can be seen.

4.3 Comparison of the results for Option 1 and Option 2

In this section, some figures showing the difference in the prediction of the forces between the two options for the model are going to be present. They are added for a better extraction of the conclusion.

Figure 4.9 illustrate the comparison for the case 0002 between Option 1 and Option 2 for C_t and C_z with $E \equiv constant$.
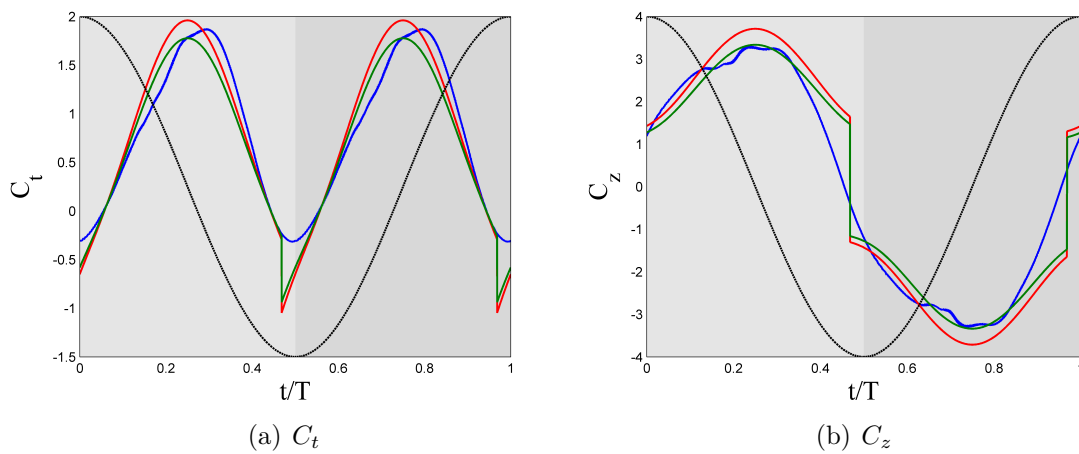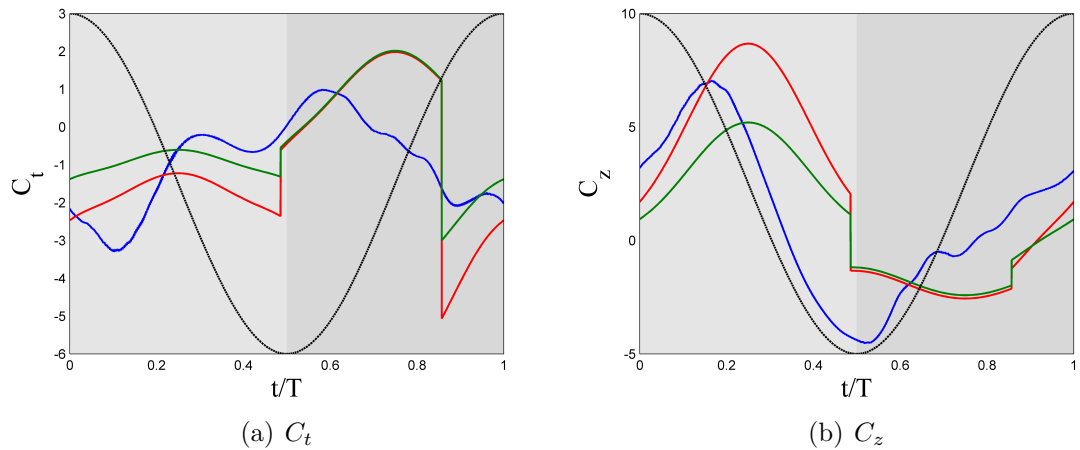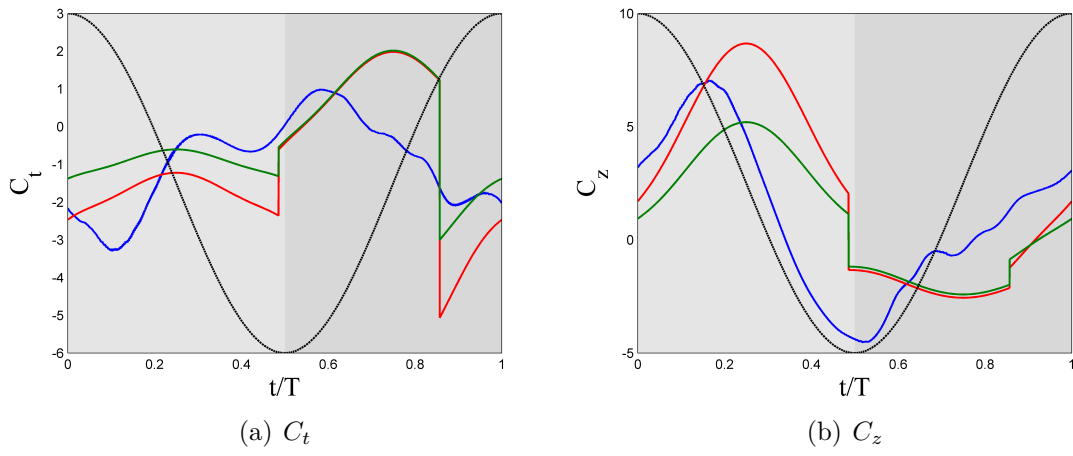

(a) C_t (b) C_z

Figure 4.9: Comparison for case 0002 ($\theta_m = 0°$ and $\phi = 70°$) of C_t and C_z between both options of the model with $E \equiv constant$. Option 1 (——), Option 2 (——), DNS (——) and the vertical position h of the airfoil (- - -)

Whereas, the difference in the prediction of the forces for this case when using $E = C_{l_{const}}/C_{d_{\propto \alpha^2_{eff}}}$ is shown in *figure 4.10*.

(a) C_t (b) C_z
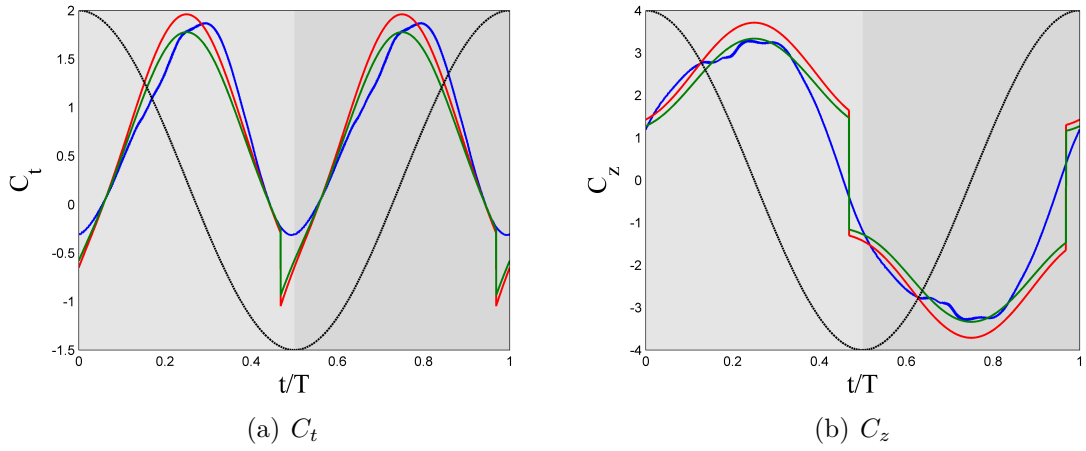
Figure 4.10: Comparison for case 0002 ($\theta_m = 0°$ and $\phi = 70°$) of C_t and C_z between both options of the model with $E = C_{l_{const}}/C_{d_{\propto\alpha^2_{eff}}}$. Option 1 (——), Option 2 (——), DNS (——) and the vertical position h of the airfoil (- - -)

In *figure 4.11* is pictured the comparison for the case 2000 between Option 1 and Option 2 for C_t and C_z with $E \equiv constant$.

(a) C_t (b) C_z

Figure 4.11: Comparison for case 2000 ($\theta_m = 20°$ and $\phi = 30°$) of C_t and C_z between both options of the model with $E \equiv constant$. Option 1 (——), Option 2 (——), DNS (——) and the vertical position h of the airfoil (- - -)

On the other hand, *figure 4.12* shows for the same case than *figure 4.11* the difference between the predicted forces of the different options, but when $E = C_{l_{const}}/C_{d_{\propto\alpha^2_{eff}}}$ is used.

(a) C_t

(b) C_z

Figure 4.12: Comparison for case 2000 ($\theta_m = 20°$ and $\phi = 30°$) of C_t and C_z between both options of the model with $E = C_{l_{const}}/C_{d_{\propto\alpha^2_{eff}}}$. Option 1 (——), Option 2 (——), DNS (——) and the vertical position h of the airfoil (- - -)

CONCLUSIONS AND FURTHER CONSIDERATIONS

In this chapter the main conclusion that can be extracted for the results obtained are going to be pointed out. Moreover, it is going to be commented future work that can be done within the aerodynamic modelling for the development of micro air vehicles.

5.1 Conclusions

Some general conclusion for both options of the new predicted aerodynamic model can be extracted.

– First of all, it must be commented that the model does better predictions for the thrust coefficient (force in the x-axis) than for the the coefficient of forces in the z-axis.

– Moreover, comparing the results obtained with the different models of aerodynamic efficiency for a specific option (option 1 or option 2), it can be conclude that more accurate results are obtained using a constant value of E. So that, it is going to be selected as the model for E.

– Generally, the NPAM does not achieve good predictions for the cases that have the lowest phase shifts ($\phi = 30°$, $50°$) and for the case that have the highest phase shift ($\phi = 130°$). Moreover, for $\theta_m = 20°$, the predictions of C_t and C_z are not acceptable for most of the cases, although they are better for the cases that have an intermediate value of ϕ.
The cases in which the new predicted aerodynamic model has worse results are the cases in which more flow separation is expected. Due to the fact that the incident flow and the airfoil is not aligned the flow is more prone to separate. The NPAM does not consider the possibility of flow separation, so that these results could have been awaited.

Taking into account what it has been above mentioned, the new predicted aerodynamic model is said to be useful for cases with mean pitch value $\theta_m = 0°$ and $\theta_m = 10°$ and phase shift $\phi = 70°, 90°$ and $110°$.

If the two options are compared, it can be conclude that Option 2 does better predictions of the forces. This imposes a huge advantage to the model since the mean value of the forces are not needed as inputs. Just with an initial guess and after an n number of iterations it could achieved the forces.

5.2   Further considerations

The following step to be done should be a flow visualization of the simulations to determine exactly in which cases the flow is more prone to separate.

It is difficult to perform further improvements to the model since a steady-state model is being consider.

In order to achieve a more accurate model some effects that are important for insect-like flapping flight should be consider. These effects are listed below.

– Wagner effect

– Wake capture

– Apparent mass effect

– Kramer effect

– Leading edge vortex (LEV)

PROJECT BUDGET

Nowadays, for an engineer, doing a budget for a project is as important as the project itself.

So that, in this section the project budget for this project is explained. The main elements that compound the budget are specified below.

- **Computer:** For carrying out the project, a computer was required. The computer used was a *HP-Pavilion* (Intel-i5) with Microsoft Windowns installed. Its price is €550.

- **MATLAB licence:** In order to do the needed computations, Matlab has been used. The academic licence of Matlab is priced in €500.

- **Working hours:** The total hours of work were, approximately, 380. A low experience engineer earn €15 per hour, which leads to a price of €5700.

The total cost of the project is detailed in *tabel A.1*.

Element	Price (€)
Computer	550
Matlab licence	500
Working hours	5700
TOTAL	**6750**

Table A.1: Project budget

Figures of the results with option 1 and $E \equiv constant$

(a) C_t

(b) C_z
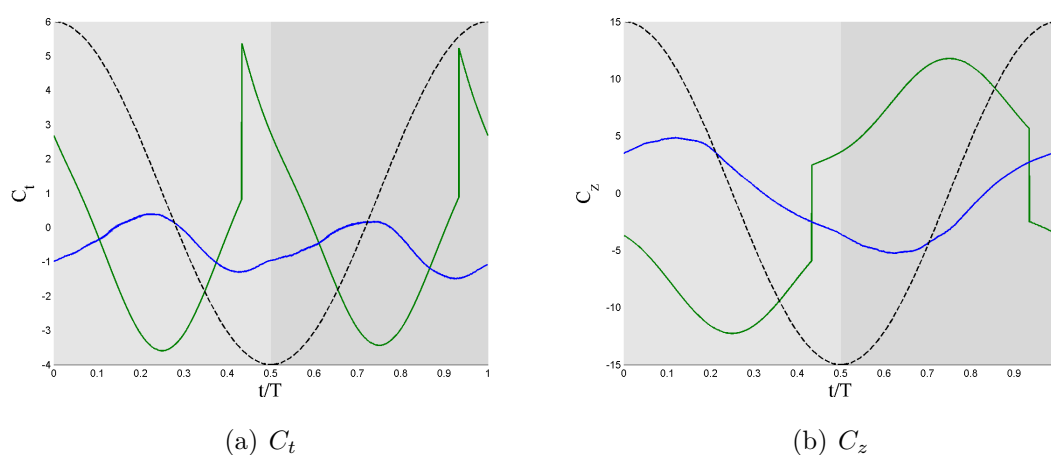
Figure B.1: Comparison for case 0000 ($\theta_m = 0°$ and $\phi = 30°$) of C_t and C_z between the model and the DNS with $E \equiv constant$. Model (——), DNS (——) and the vertical position h of the airfoil (- - -)
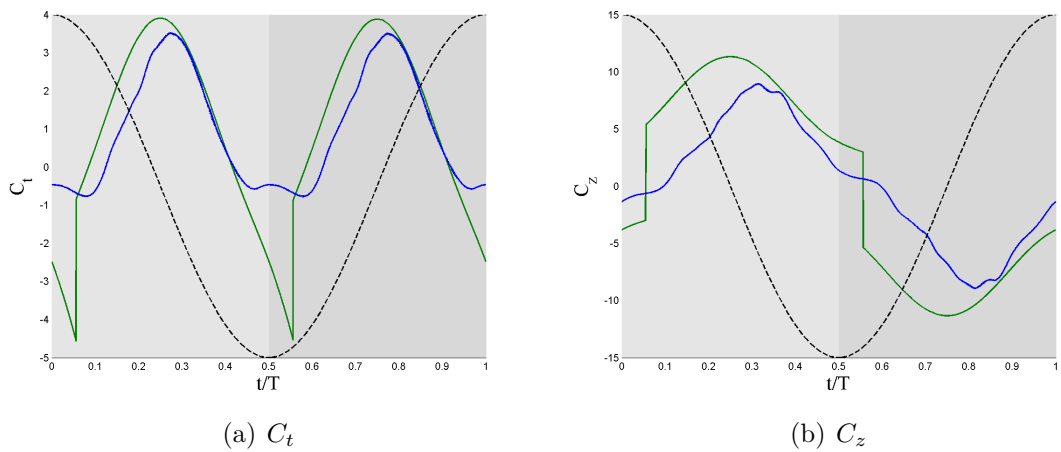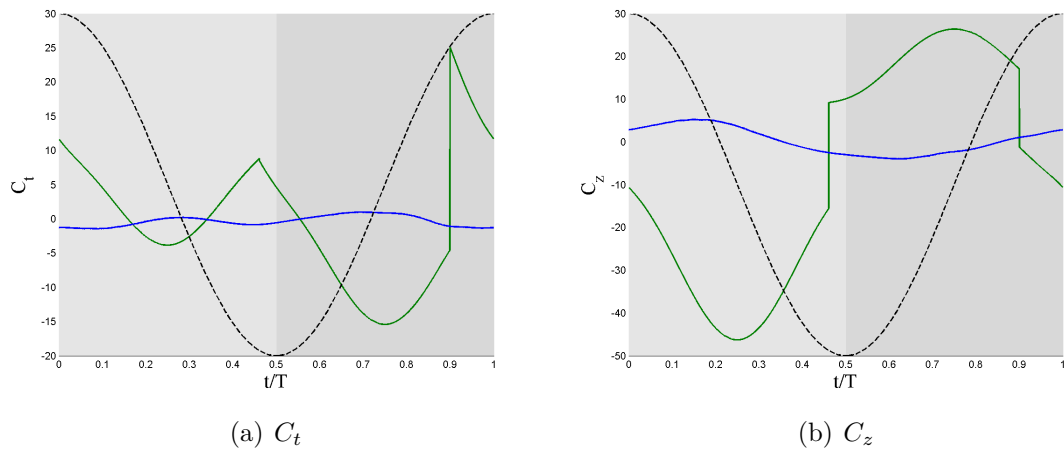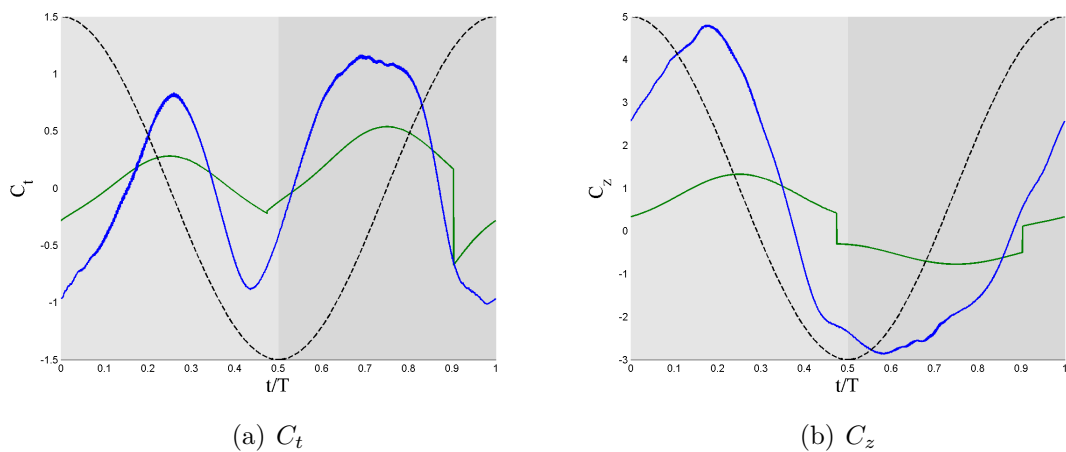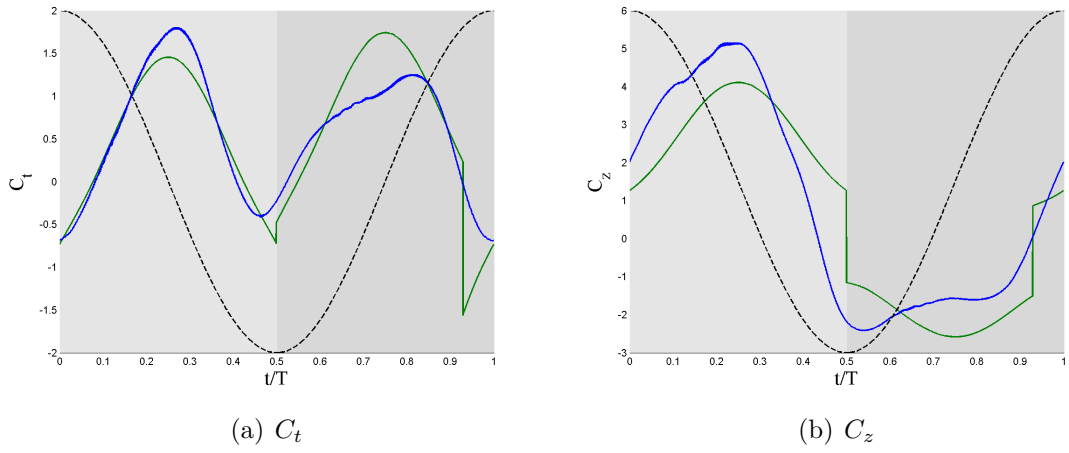
(a) C_t (b) C_z
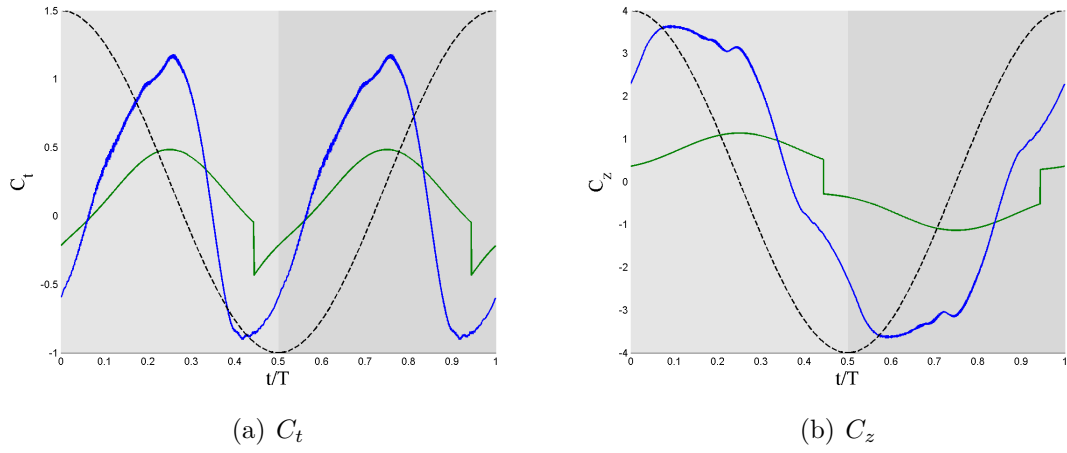
Figure B.2: Comparison for case 0001 ($\theta_m = 0°$ and $\phi = 50°$) of C_t and C_z between the model and the DNS with $E \equiv constant$. Model (——), DNS (——) and the vertical position h of the airfoil (- - -)
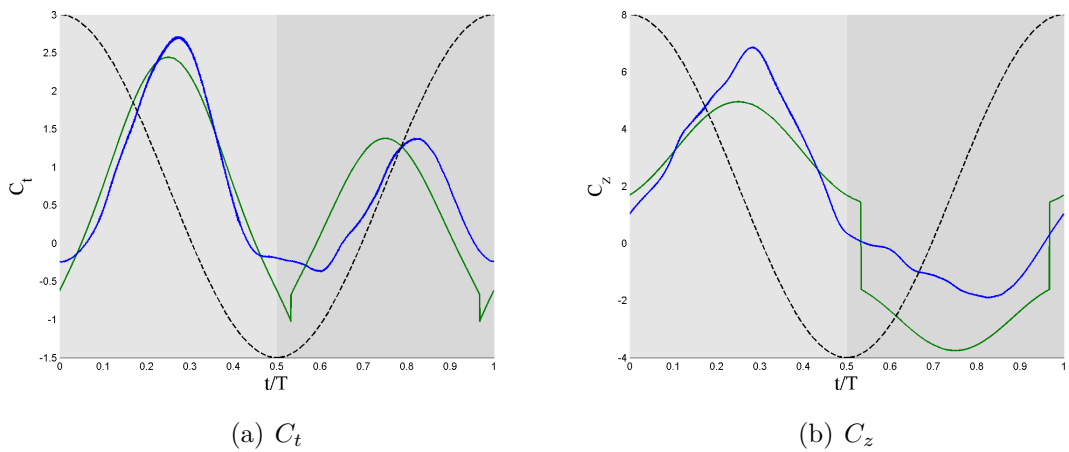

(a) C_t (b) C_z
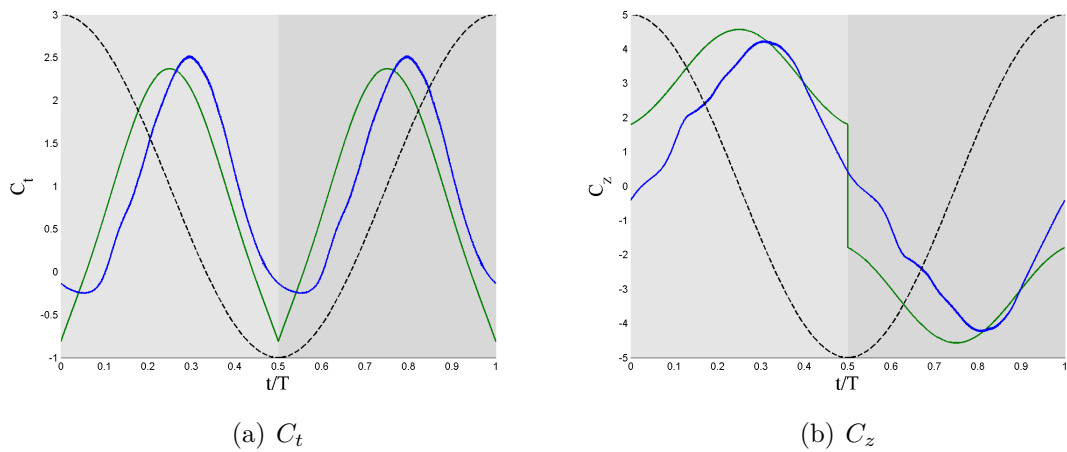
Figure B.3: Comparison for case 0003 ($\theta_m = 0°$ and $\phi = 90°$) of C_t and C_z between the model and the DNS with $E \equiv constant$. Model (——), DNS (——) and the vertical position h of the airfoil (- - -)
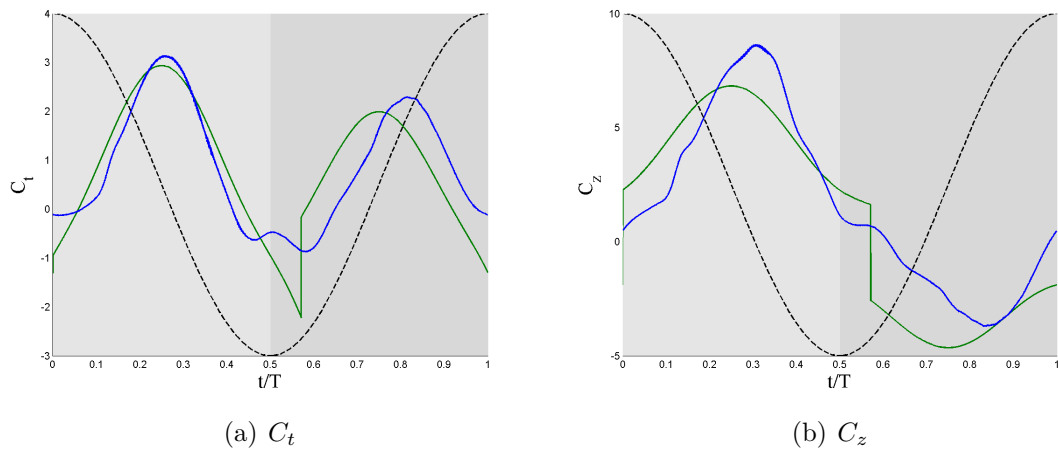
(a) C_t (b) C_z
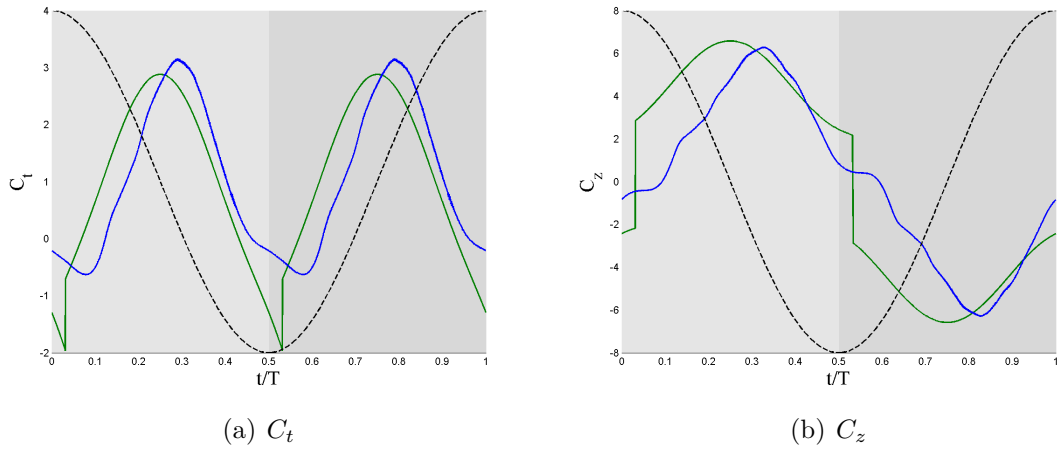
Figure B.4: Comparison for case 0004 ($\theta_m = 0°$ and $\phi = 110°$) of C_t and C_z between the model and the DNS with $E \equiv constant$. Model (——), DNS (——) and the vertical position h of the airfoil (- - -)

(a) C_t (b) C_z

Figure B.5: Comparison for case 0005 ($\theta_m = 0°$ and $\phi = 130°$) of C_t and C_z between the model and the DNS with $E \equiv constant$. Model (——), DNS (——) and the vertical position h of the airfoil (- - -)
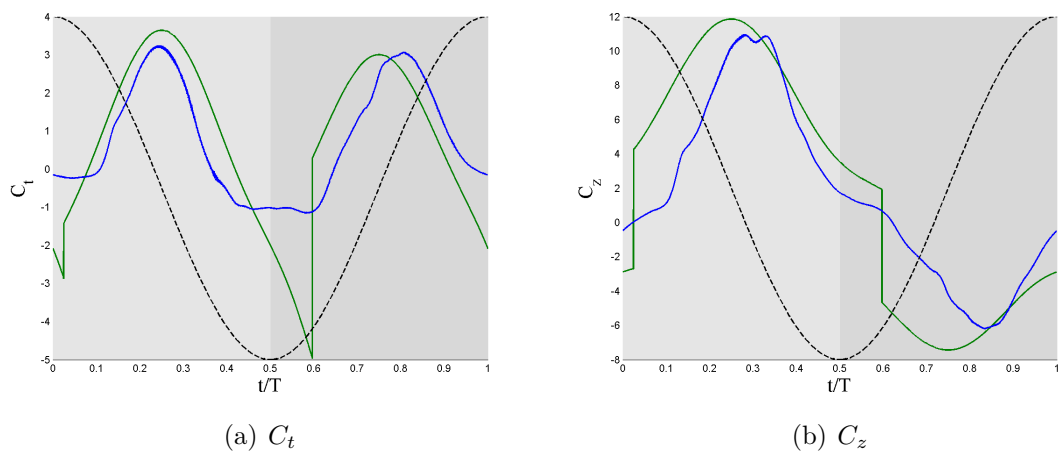
(a) C_t (b) C_z

Figure B.6: Comparison for case 1000 ($\theta_m = 10°$ and $\phi = 30°$) of C_t and C_z between the model and the DNS with $E \equiv constant$. Model (——), DNS (——) and the vertical position h of the airfoil (- - -)
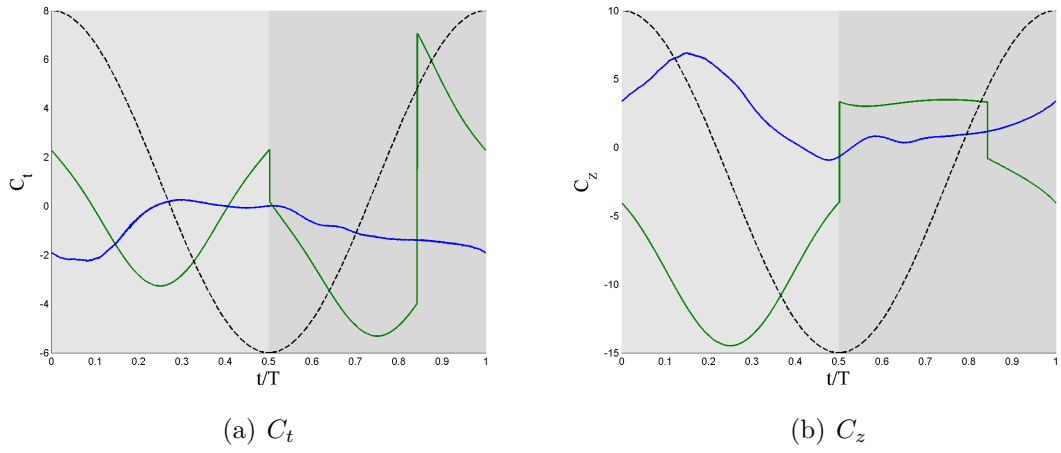

(a) C_t (b) C_z

Figure B.7: Comparison for case 1001 ($\theta_m = 10°$ and $\phi = 50°$) of C_t and C_z between the model and the DNS with $E \equiv constant$. Model (——), DNS (——) and the vertical position h of the airfoil (- - -)
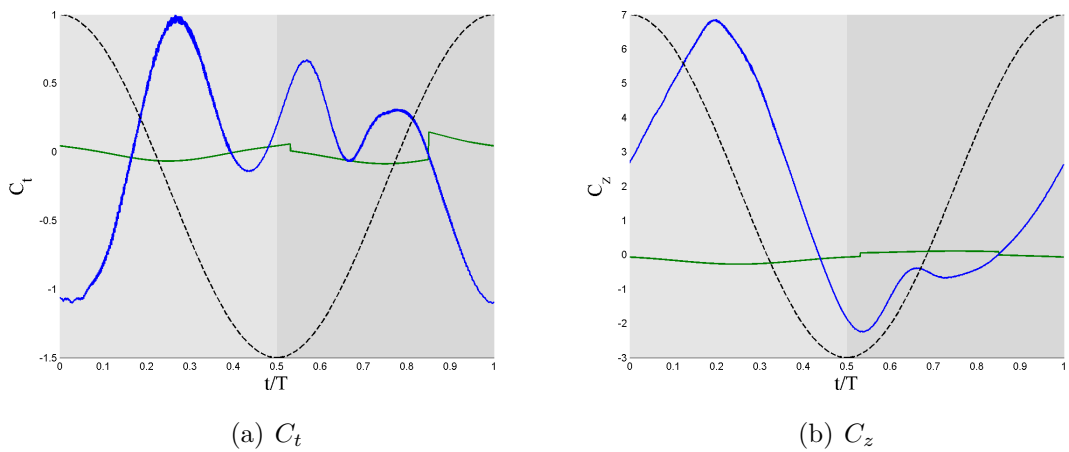
(a) C_t (b) C_z

Figure B.8: Comparison for case 1002 ($\theta_m = 10°$ and $\phi = 70°$) of C_t and C_z between the model and the DNS with $E \equiv constant$. Model (——), DNS (——) and the vertical position h of the airfoil (- - -)
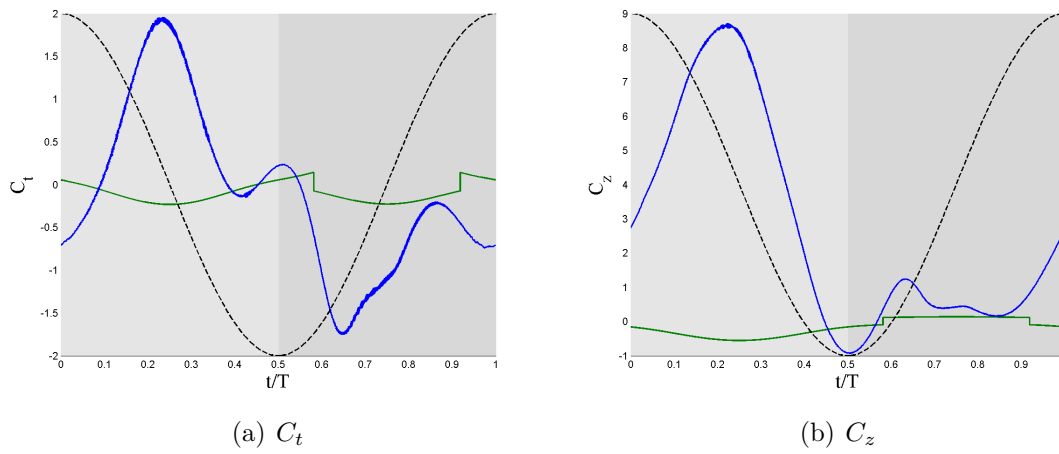

(a) C_t (b) C_z

Figure B.9: Comparison for case 1003 ($\theta_m = 10°$ and $\phi = 90°$) of C_t and C_z between the model and the DNS with $E \equiv constant$. Model (——), DNS (——) and the vertical position h of the airfoil (- - -)
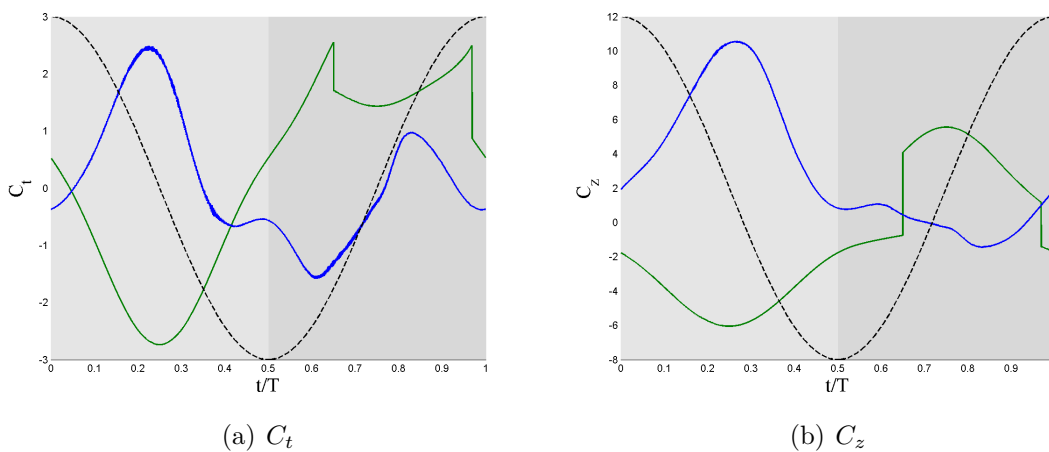
(a) C_t (b) C_z

Figure B.10: Comparison for case 1004 ($\theta_m = 10°$ and $\phi = 110°$) of C_t and C_z between the model and the DNS with $E \equiv constant$. Model (——), DNS (——) and the vertical position h of the airfoil (- - -)

(a) C_t (b) C_z

Figure B.11: Comparison for case 1005 ($\theta_m = 10°$ and $\phi = 130°$) of C_t and C_z between the model and the DNS with $E \equiv constant$. Model (——), DNS (——) and the vertical position h of the airfoil (- - -)
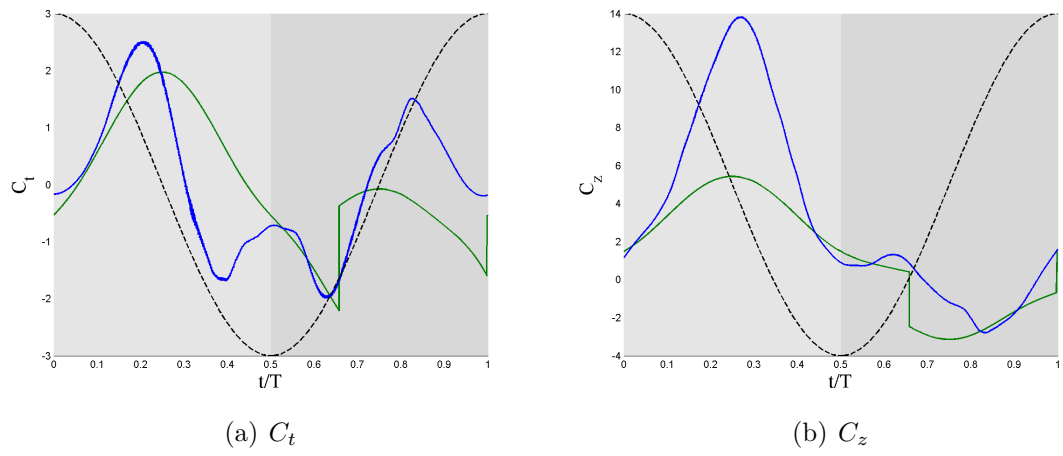
(a) C_t (b) C_z

Figure B.12: Comparison for case 2001 ($\theta_m = 20°$ and $\phi = 50°$) of C_t and C_z between the model and the DNS with $E \equiv constant$. Model (——), DNS (——) and the vertical position h of the airfoil (- - -)

(a) C_t (b) C_z

Figure B.13: Comparison for case 2002 ($\theta_m = 20°$ and $\phi = 70°$) of C_t and C_z between the model and the DNS with $E \equiv constant$. Model (——), DNS (——) and the vertical position h of the airfoil (- - -)

(a) C_t (b) C_z

Figure B.14: Comparison for case 2003 ($\theta_m = 20°$ and $\phi = 90°$) of C_t and C_z between the model and the DNS with $E \equiv constant$. Model (——), DNS (——) and the vertical position h of the airfoil (- - -)

(a) C_t (b) C_z

Figure B.15: Comparison for case 1004 ($\theta_m = 20°$ and $\phi = 110°$) of C_t and C_z between the model and the DNS with $E \equiv constant$. Model (——), DNS (——) and the vertical position h of the airfoil (- - -)

(a) C_t (b) C_z

Figure B.16: Comparison for case 2005 ($\theta_m = 20°$ and $\phi = 130°$) of C_t and C_z between the model and the DNS with $E \equiv constant$. Model (——), DNS (——) and the vertical position h of the airfoil (- - -)

Figures of the results with option 1 and $E = C_{l_{const}}/C_{d_{\propto\alpha^2_{eff}}}$

(a) C_t

(b) C_z
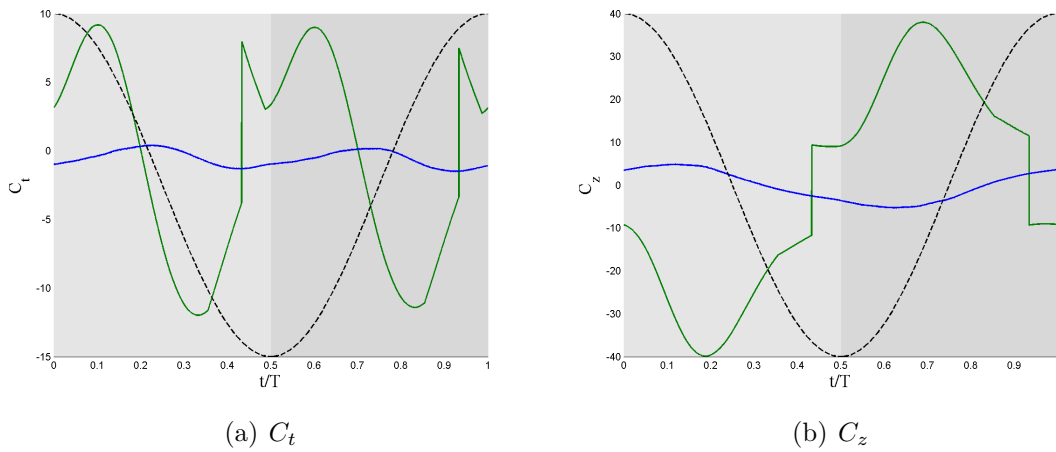
Figure C.1: Comparison for case 0000 ($\theta_m = 0°$ and $\phi = 30°$) of C_t and C_z between the model and the DNS with $E = C_{l_{const}}/C_{d_{\propto\alpha^2_{eff}}}$. Model (——), DNS (——) and the vertical position h of the airfoil (- - -)
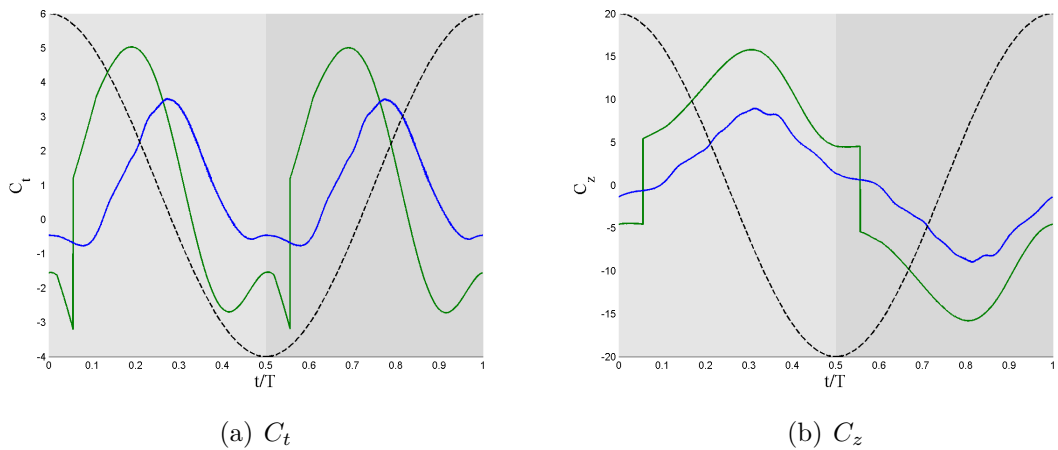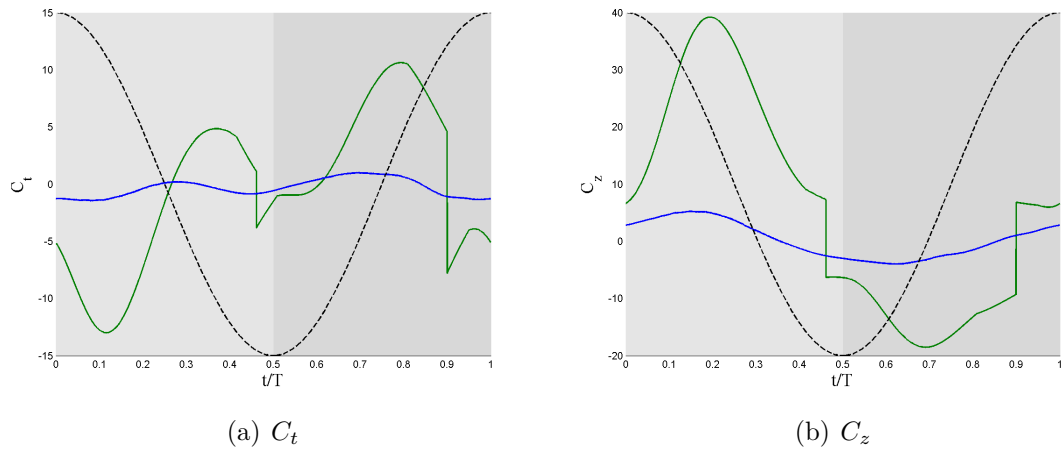
(a) C_t (b) C_z
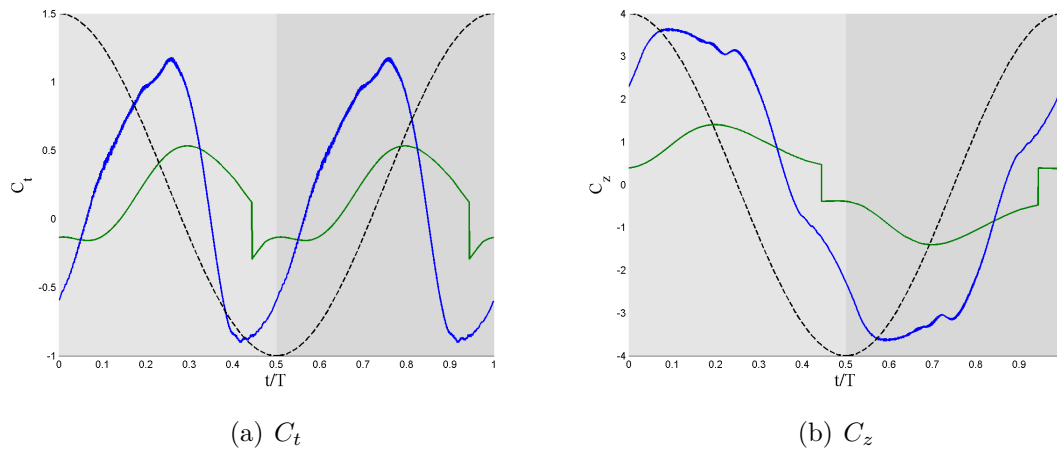
Figure C.2: Comparison for case 0001 ($\theta_m = 0°$ and $\phi = 50°$) of C_t and C_z between the model and the DNS with $E = C_{l_{const}}/C_{d_{\propto \alpha^2_{eff}}}$. Model (——), DNS (——) and the vertical position h of the airfoil (- - -)

(a) C_t (b) C_z
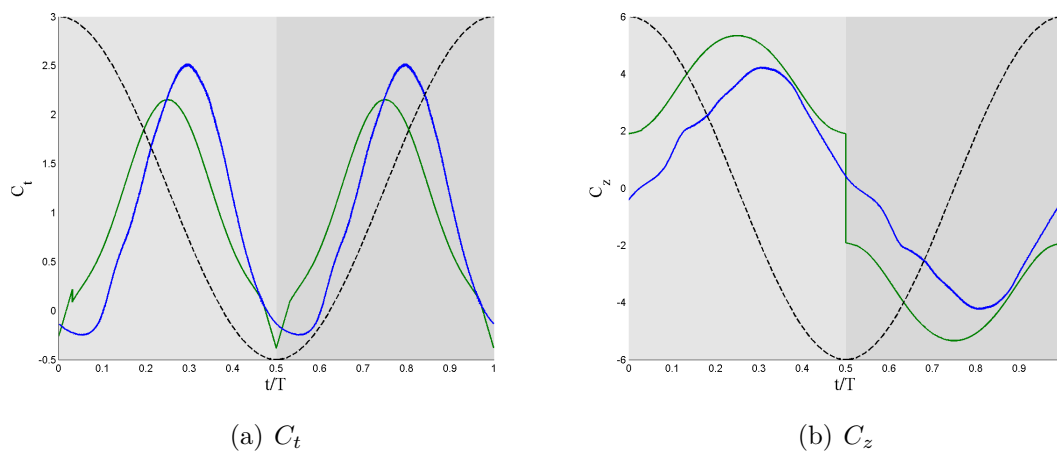
Figure C.3: Comparison for case 0003 ($\theta_m = 0°$ and $\phi = 90°$) of C_t and C_z between the model and the DNS with $E = C_{l_{const}}/C_{d_{\propto \alpha^2_{eff}}}$. Model (——), DNS (——) and the vertical position h of the airfoil (- - -)
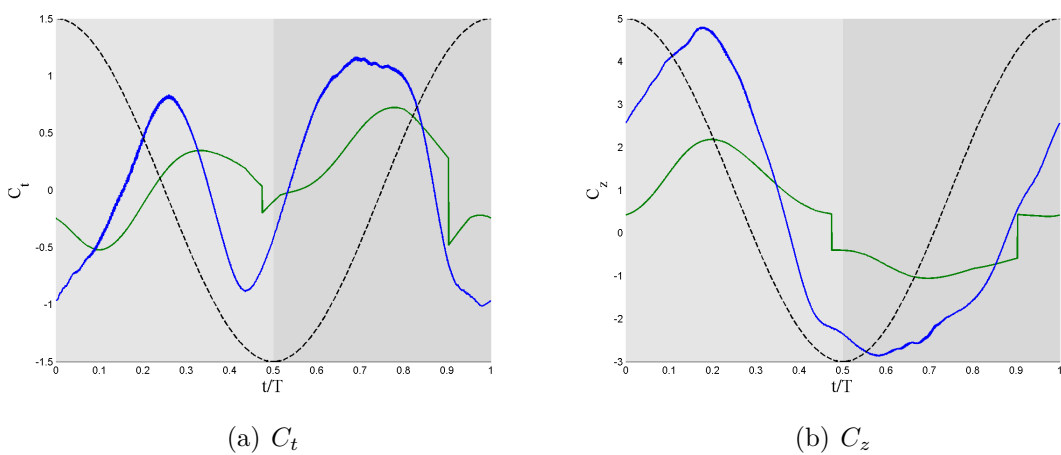
(a) C_t (b) C_z
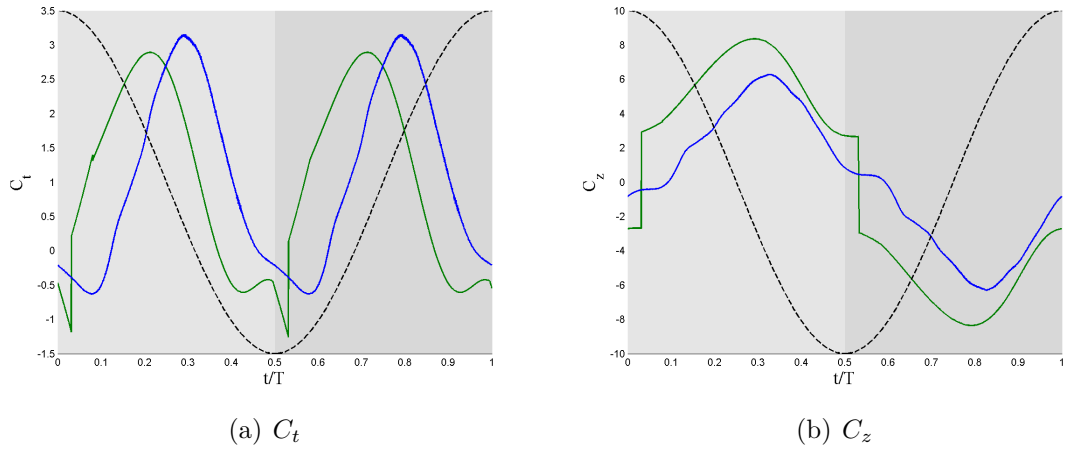
Figure C.4: Comparison for case 0004 ($\theta_m = 0°$ and $\phi = 110°$) of C_t and C_z between the model and the DNS with $E = C_{l_{const}}/C_{d_{\propto \alpha_{eff}^2}}$. Model (——), DNS (——) and the vertical position h of the airfoil (- - -)
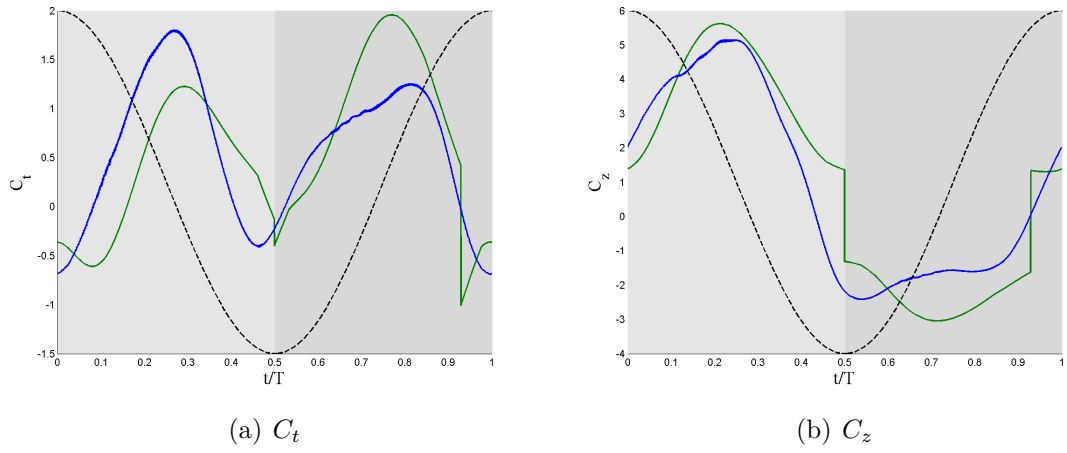

(a) C_t (b) C_z

Figure C.5: Comparison for case 0005 ($\theta_m = 0°$ and $\phi = 130°$) of C_t and C_z between the model and the DNS with $E = C_{l_{const}}/C_{d_{\propto \alpha_{eff}^2}}$. Model (——), DNS (——) and the vertical position h of the airfoil (- - -)
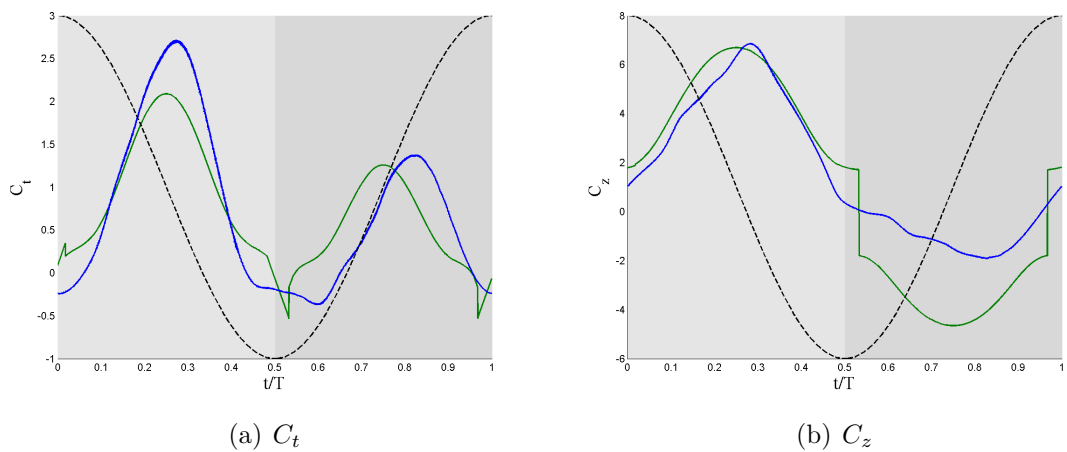
(a) C_t (b) C_z

Figure C.6: Comparison for case 1000 ($\theta_m = 10°$ and $\phi = 30°$) of C_t and C_z between the model and the DNS with $E = C_{l_{const}}/C_{d_{\propto \alpha_{eff}^2}}$. Model (——), DNS (——) and the vertical position h of the airfoil (- - -)
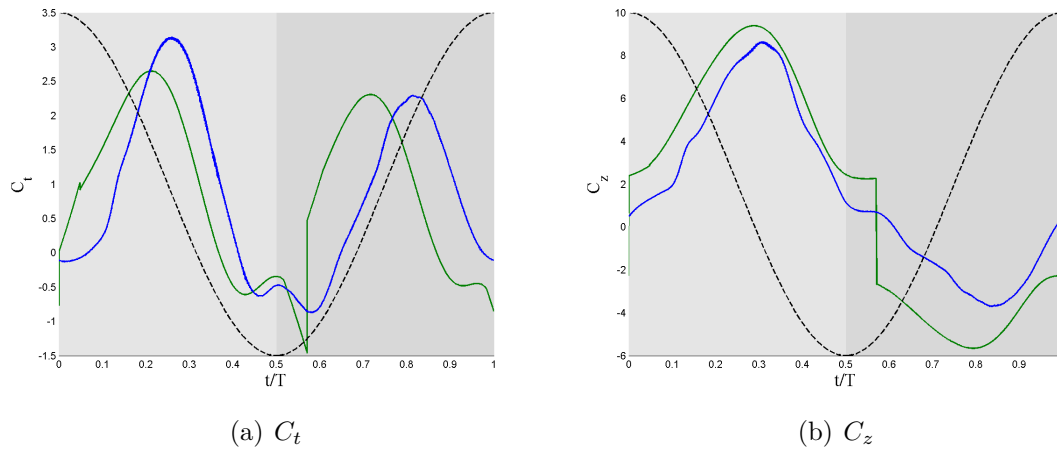

(a) C_t (b) C_z

Figure C.7: Comparison for case 1001 ($\theta_m = 10°$ and $\phi = 50°$) of C_t and C_z between the model and the DNS with $E = C_{l_{const}}/C_{d_{\propto \alpha_{eff}^2}}$. Model (——), DNS (——) and the vertical position h of the airfoil (- - -)
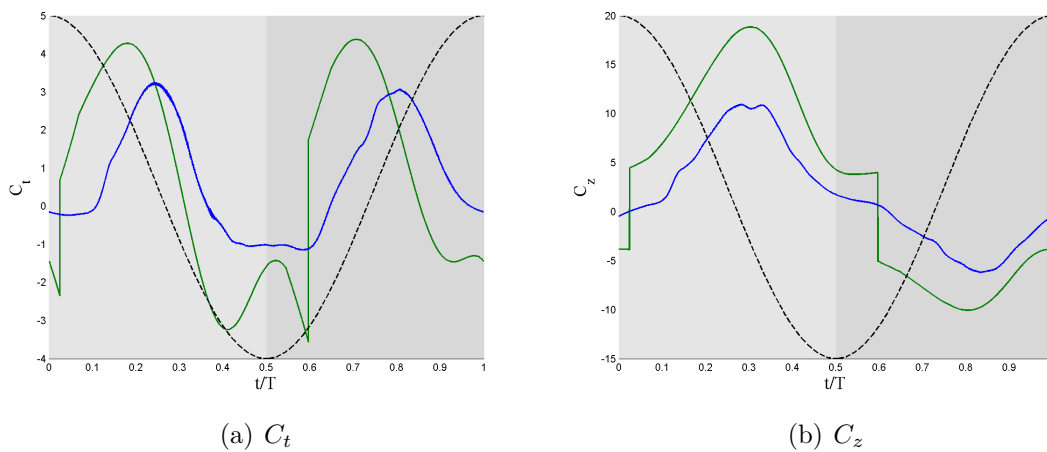
(a) C_t \quad\quad (b) C_z

Figure C.8: Comparison for case 1002 ($\theta_m = 10°$ and $\phi = 70°$) of C_t and C_z between the model and the DNS with $E = C_{l_{const}}/C_{d_{\propto\alpha^2_{eff}}}$. Model (—), DNS (—) and the vertical position h of the airfoil (- - -)
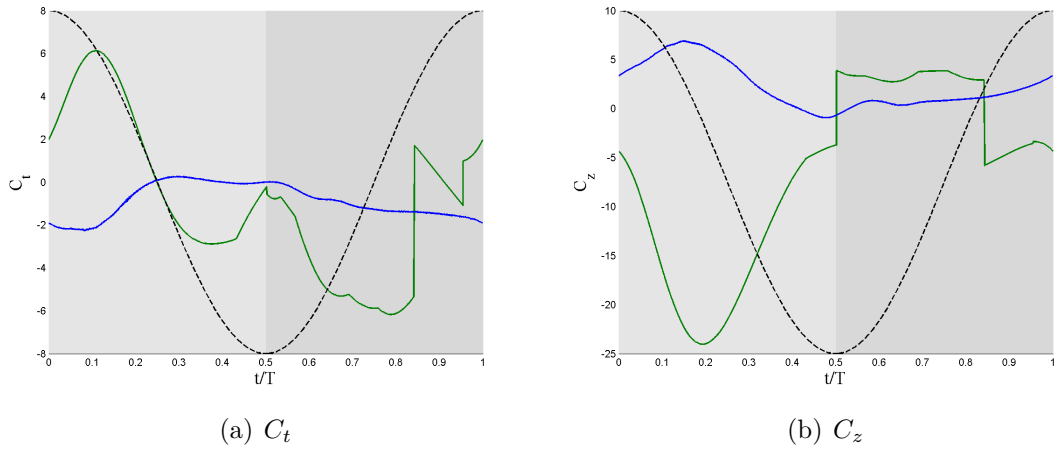

(a) C_t \quad\quad (b) C_z

Figure C.9: Comparison for case 1003 ($\theta_m = 10°$ and $\phi = 90°$) of C_t and C_z between the model and the DNS with $E = C_{l_{const}}/C_{d_{\propto\alpha^2_{eff}}}$. Model (—), DNS (—) and the vertical position h of the airfoil (- - -)
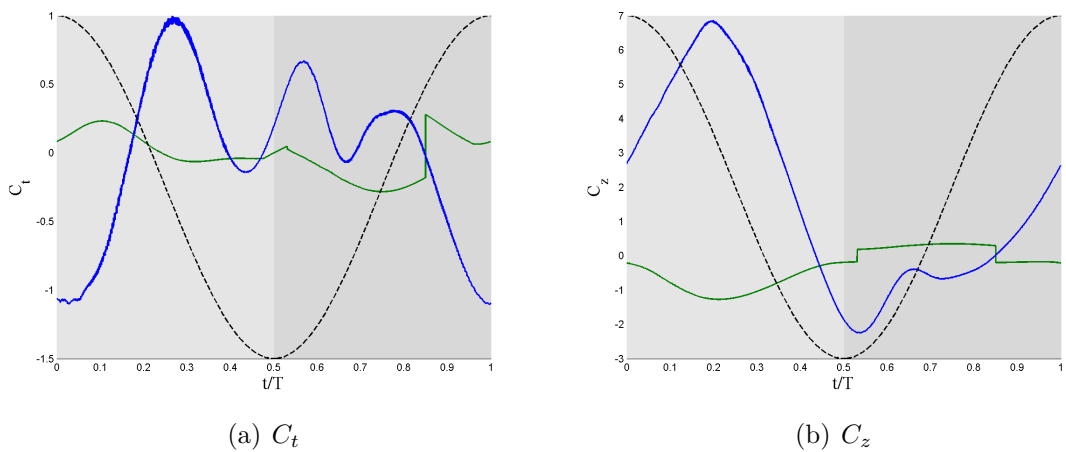
(a) C_t

(b) C_z

Figure C.10: Comparison for case 1004 ($\theta_m = 10°$ and $\phi = 110°$) of C_t and C_z between the model and the DNS with $E = C_{l_{const}}/C_{d_{\propto\alpha^2_{eff}}}$. Model (—), DNS (—) and the vertical position h of the airfoil (- - -)
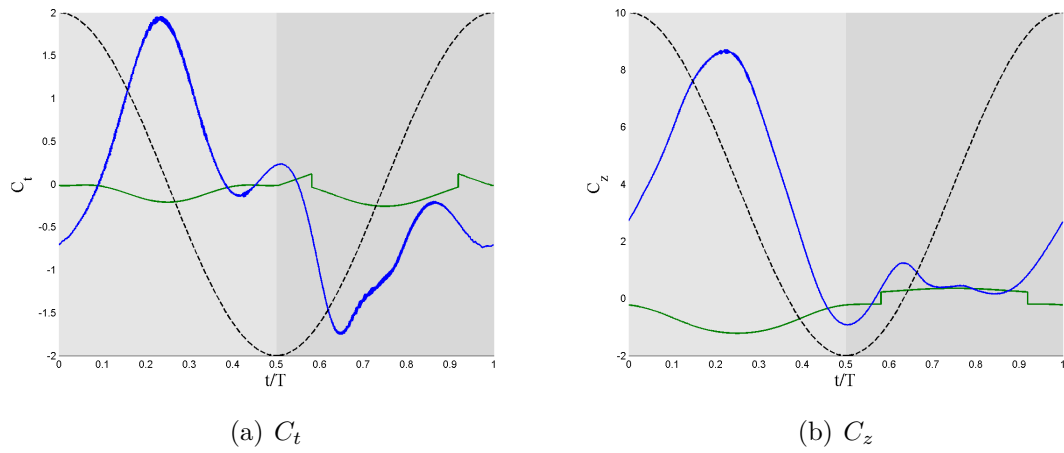

(a) C_t

(b) C_z

Figure C.11: Comparison for case 1005 ($\theta_m = 10°$ and $\phi = 130°$) of C_t and C_z between the model and the DNS with $E = C_{l_{const}}/C_{d_{\propto\alpha^2_{eff}}}$. Model (—), DNS (—) and the vertical position h of the airfoil (- - -)

(a) C_t

(b) C_z

Figure C.12: Comparison for case 2001 ($\theta_m = 20°$ and $\phi = 50°$) of C_t and C_z between the model and the DNS with $E = C_{l_{const}}/C_{d_{\propto \alpha^2_{eff}}}$. Model (——), DNS (——) and the vertical position h of the airfoil (- - -)
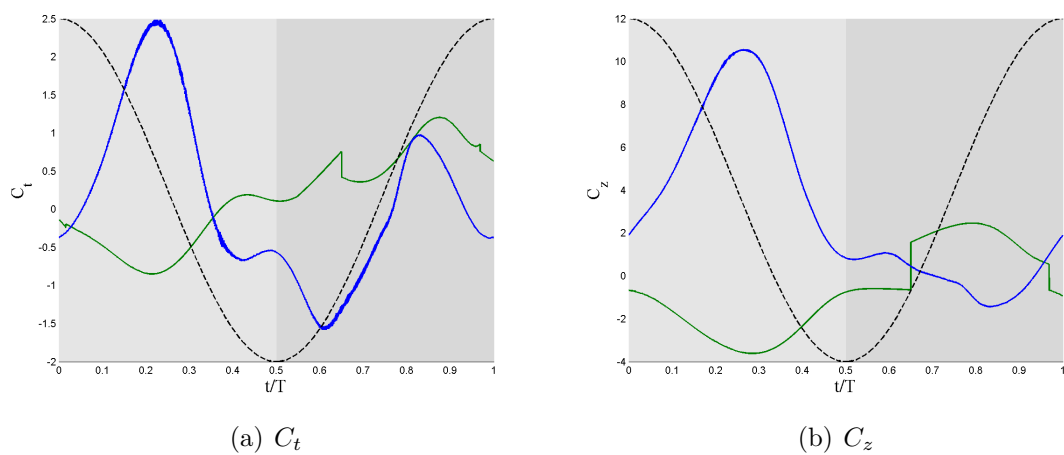

(a) C_t

(b) C_z

Figure C.13: Comparison for case 2002 ($\theta_m = 20°$ and $\phi = 70°$) of C_t and C_z between the model and the DNS with $E = C_{l_{const}}/C_{d_{\propto \alpha^2_{eff}}}$. Model (——), DNS (——) and the vertical position h of the airfoil (- - -)
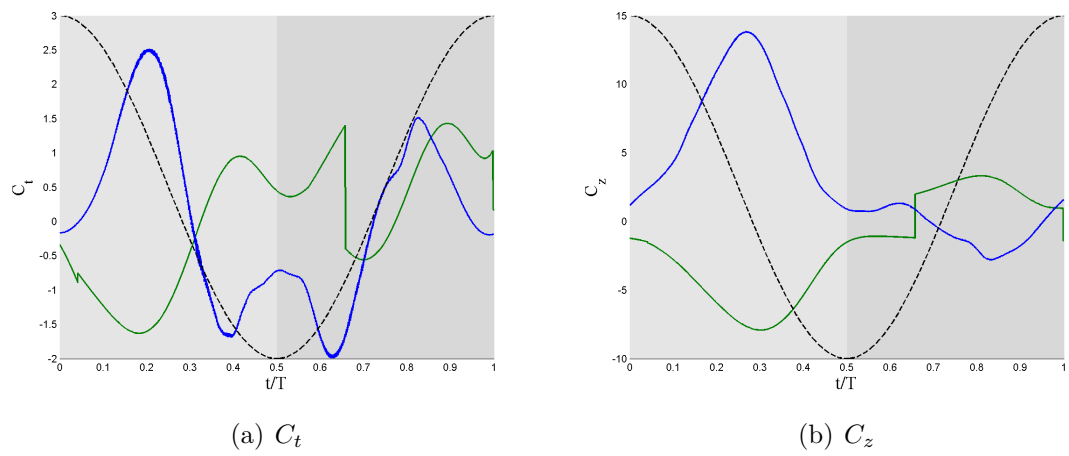
(a) C_t

(b) C_z

Figure C.14: Comparison for case 2003 ($\theta_m = 20°$ and $\phi = 90°$) of C_t and C_z between the model and the DNS with $E = C_{l_{const}}/C_{d_{\propto \alpha^2_{eff}}}$. Model (——), DNS (——) and the vertical position h of the airfoil (- - -)

(a) C_t

(b) C_z

Figure C.15: Comparison for case 1004 ($\theta_m = 20°$ and $\phi = 110°$) of C_t and C_z between the model and the DNS with $E = C_{l_{const}}/C_{d_{\propto \alpha^2_{eff}}}$. Model (——), DNS (——) and the vertical position h of the airfoil (- - -)

(a) C_t

(b) C_z

Figure C.16: Comparison for case 2005 ($\theta_m = 20°$ and $\phi = 130°$) of C_t and C_z between the model and the DNS with $E = C_{l_{const}}/C_{d_{\propto \alpha^2_{eff}}}$. Model (——), DNS (——) and the vertical position h of the airfoil (- - -)

D

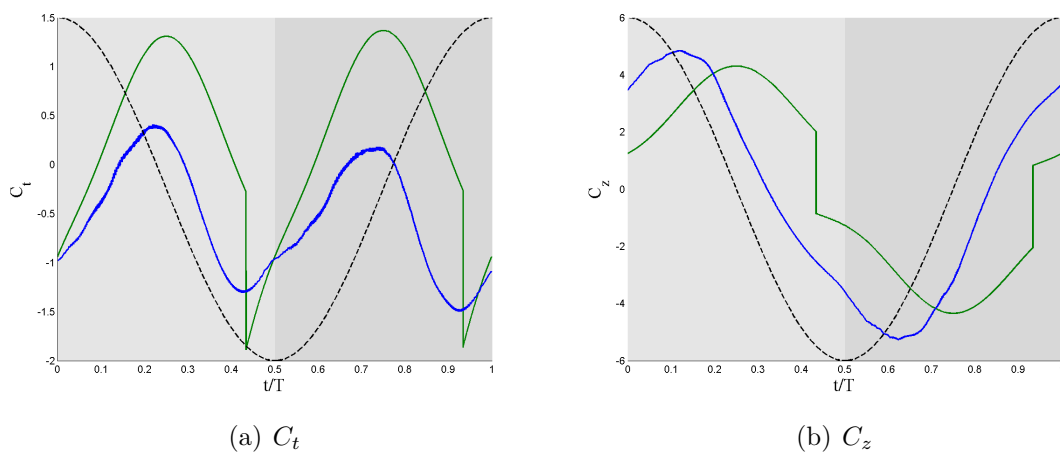# Figures of the results with option 2 and $E \equiv constant$

(a) C_t (b) C_z

Figure D.1: Comparison for case 0000 ($\theta_m = 0°$ and $\phi = 30°$) of C_t and C_z between the model and the DNS with $E \equiv constant$. Model (——), DNS (——) and the vertical position h of the airfoil (- - -)
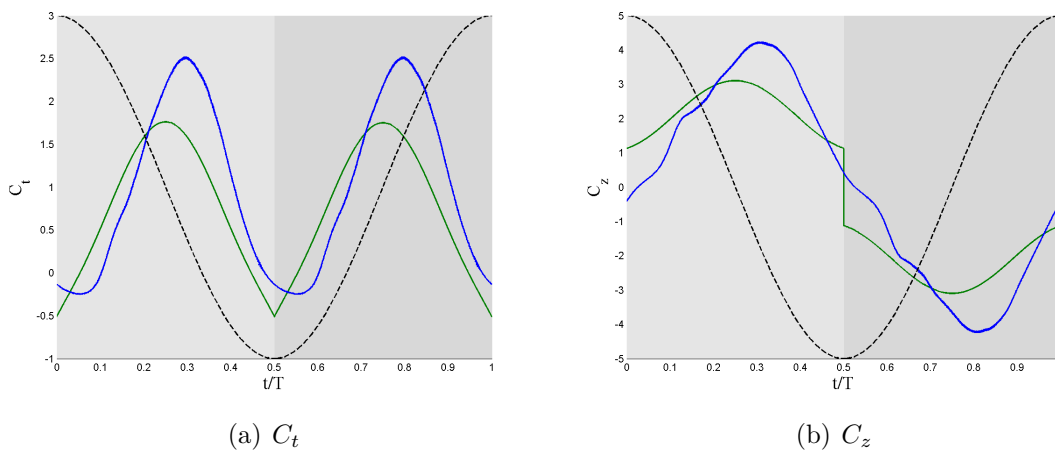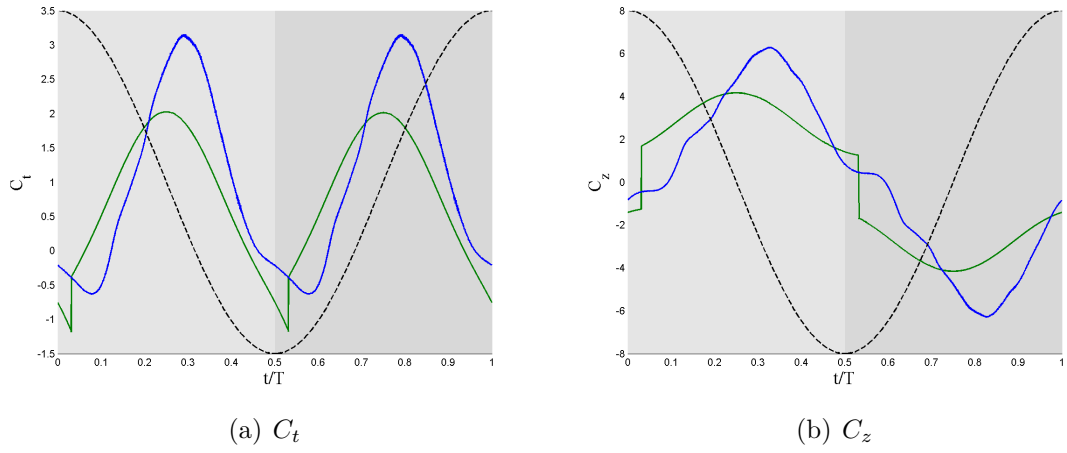
(a) C_t

(b) C_z
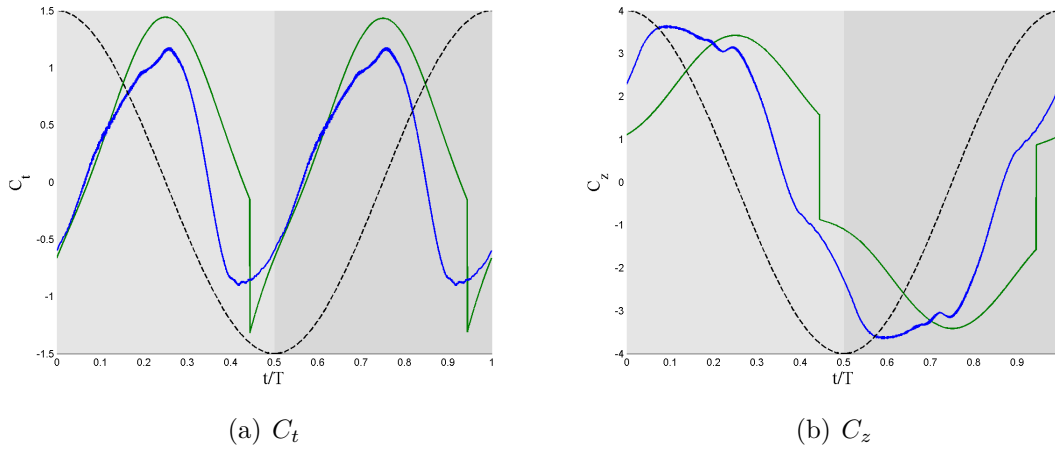
Figure D.2: Comparison for case 0001 ($\theta_m = 0°$ and $\phi = 50°$) of C_t and C_z between the model and the DNS with $E \equiv constant$. Model (——), DNS (——) and the vertical position h of the airfoil (- - -)
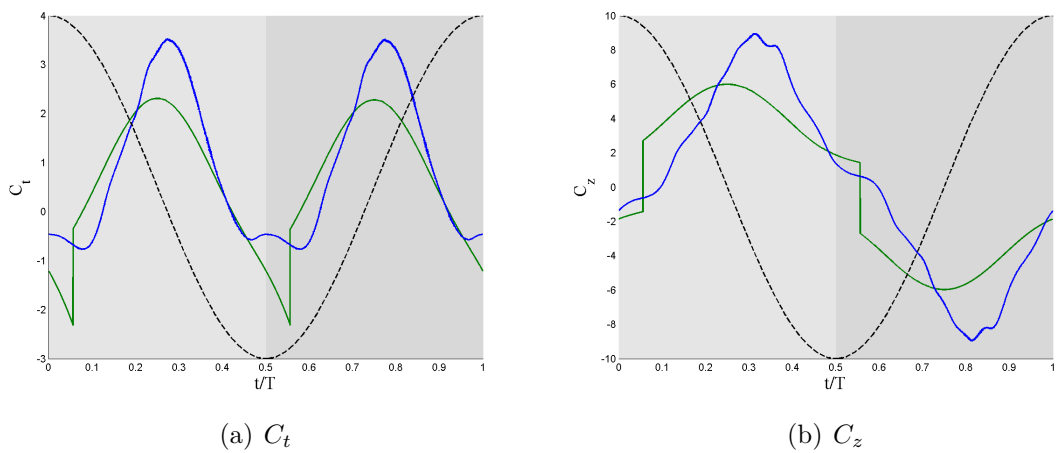

(a) C_t

(b) C_z

Figure D.3: Comparison for case 0003 ($\theta_m = 0°$ and $\phi = 90°$) of C_t and C_z between the model and the DNS with $E \equiv constant$. Model (——), DNS (——) and the vertical position h of the airfoil (- - -)

(a) C_t (b) C_z

Figure D.4: Comparison for case 0004 ($\theta_m = 0°$ and $\phi = 110°$) of C_t and C_z between the model and the DNS with $E \equiv constant$. Model (——), DNS (——) and the vertical position h of the airfoil (- - -)
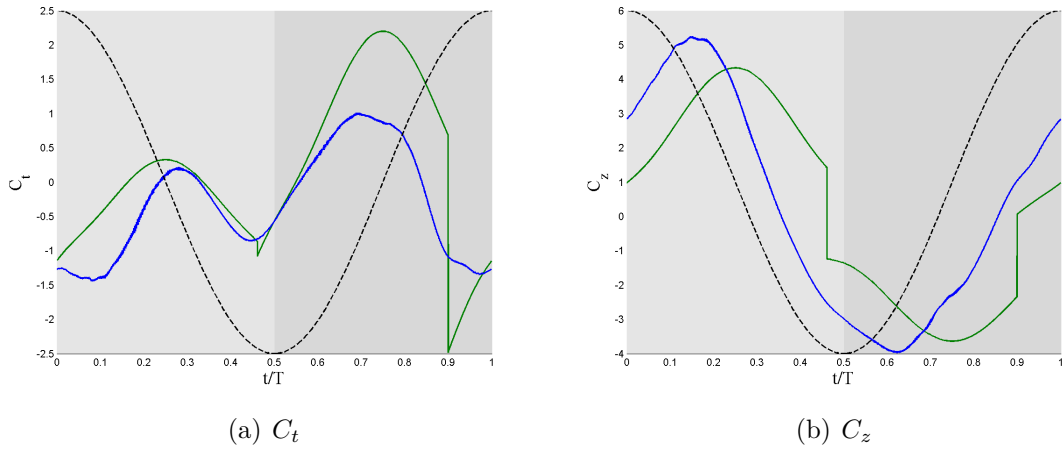

(a) C_t (b) C_z

Figure D.5: Comparison for case 0005 ($\theta_m = 0°$ and $\phi = 130°$) of C_t and C_z between the model and the DNS with $E \equiv constant$. Model (——), DNS (——) and the vertical position h of the airfoil (- - -)
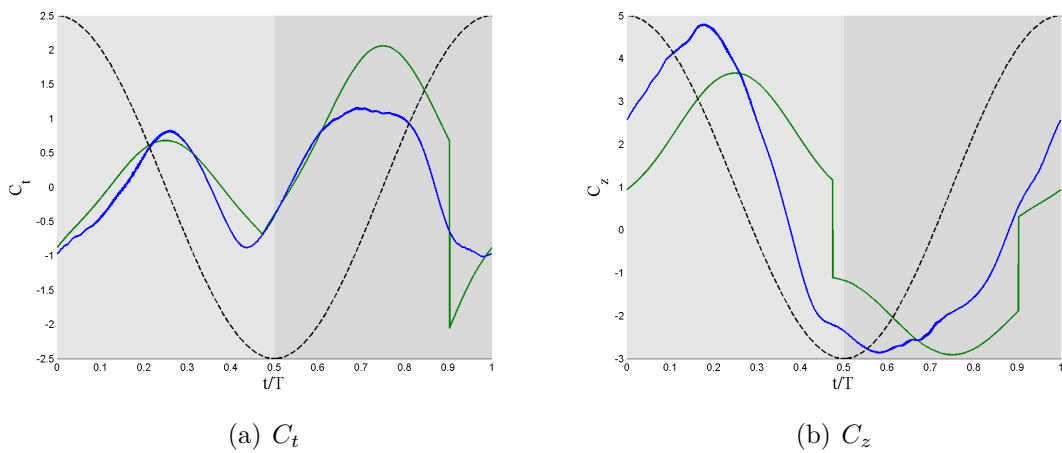
(a) C_t (b) C_z

Figure D.6: Comparison for case 1000 ($\theta_m = 10°$ and $\phi = 30°$) of C_t and C_z between the model and the DNS with $E \equiv constant$. Model (—), DNS (—) and the vertical position h of the airfoil (- - -)
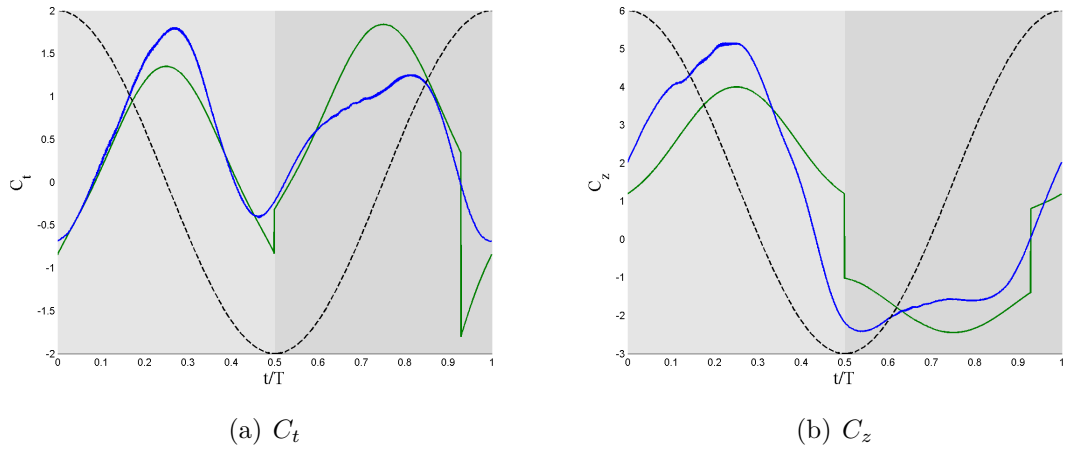

(a) C_t (b) C_z

Figure D.7: Comparison for case 1001 ($\theta_m = 10°$ and $\phi = 50°$) of C_t and C_z between the model and the DNS with $E \equiv constant$. Model (—), DNS (—) and the vertical position h of the airfoil (- - -)
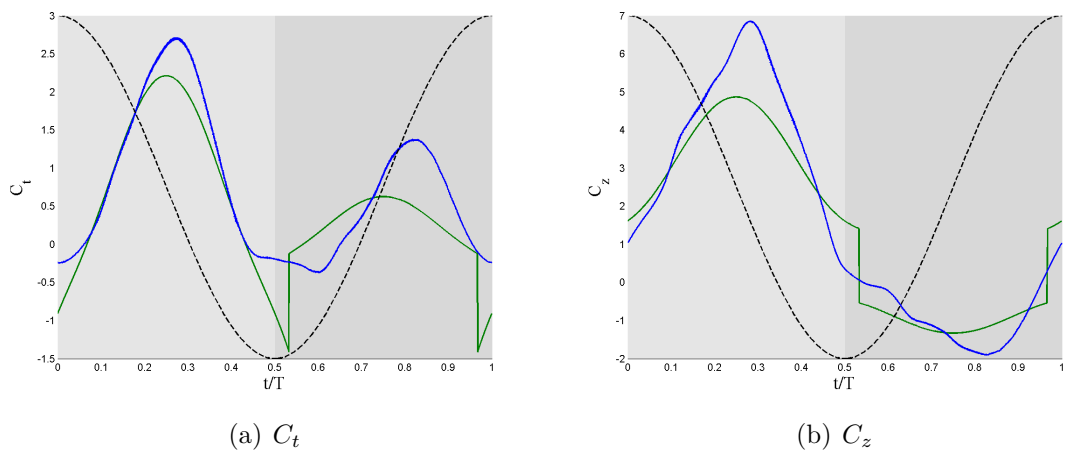
(a) C_t

(b) C_z

Figure D.8: Comparison for case 1002 ($\theta_m = 10°$ and $\phi = 70°$) of C_t and C_z between the model and the DNS with $E \equiv constant$. Model (——), DNS (——) and the vertical position h of the airfoil (- - -)

(a) C_t

(b) C_z

Figure D.9: Comparison for case 1003 ($\theta_m = 10°$ and $\phi = 90°$) of C_t and C_z between the model and the DNS with $E \equiv constant$. Model (——), DNS (——) and the vertical position h of the airfoil (- - -)
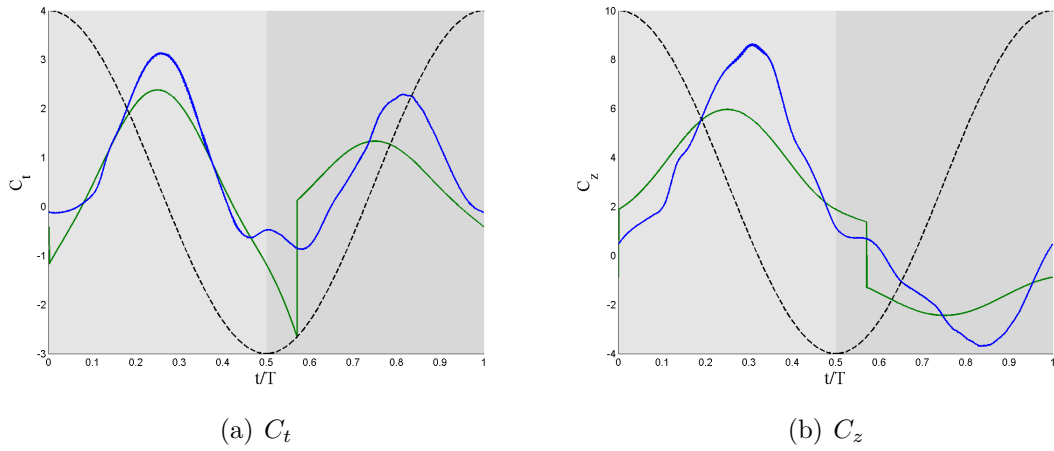
(a) C_t

(b) C_z

Figure D.10: Comparison for case 1004 ($\theta_m = 10°$ and $\phi = 110°$) of C_t and C_z between the model and the DNS with $E \equiv constant$. Model (——), DNS (——) and the vertical position h of the airfoil (- - -)
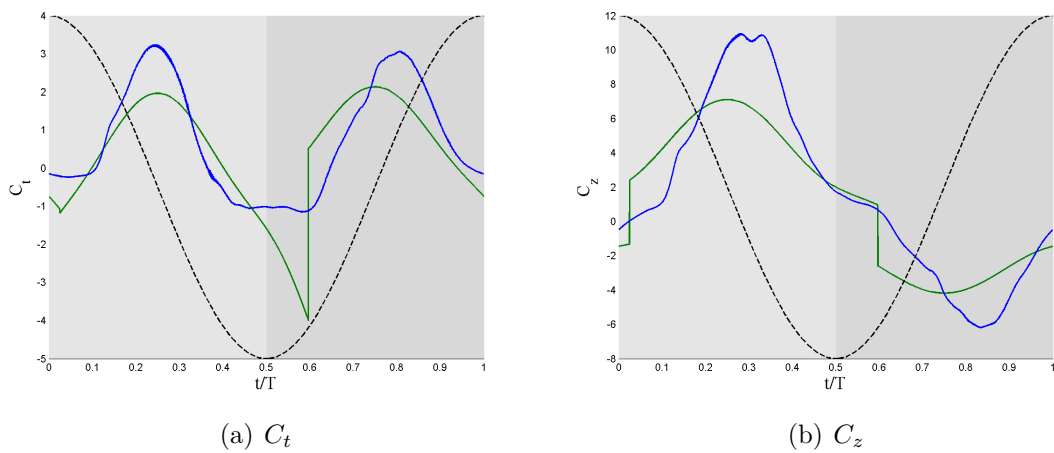

(a) C_t

(b) C_z

Figure D.11: Comparison for case 1005 ($\theta_m = 10°$ and $\phi = 130°$) of C_t and C_z between the model and the DNS with $E \equiv constant$. Model (——), DNS (——) and the vertical position h of the airfoil (- - -)
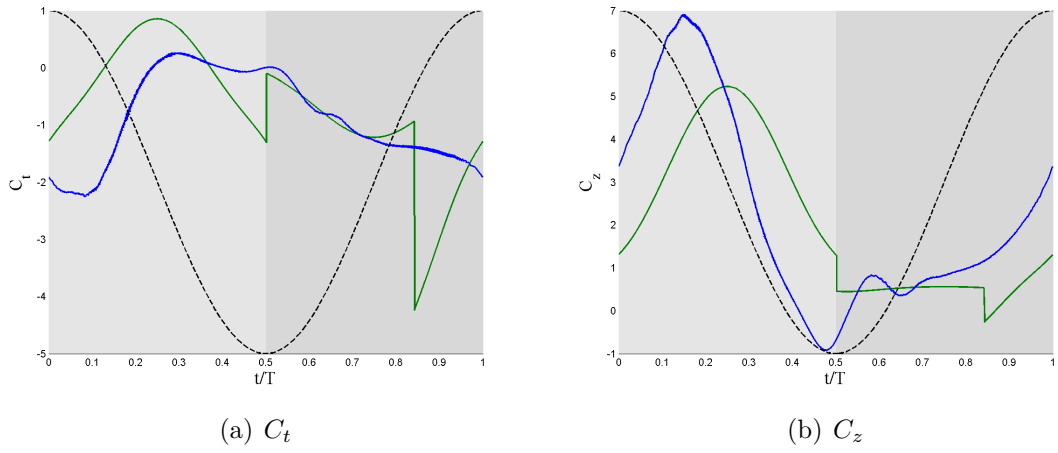
(a) C_t (b) C_z

Figure D.12: Comparison for case 2001 ($\theta_m = 20°$ and $\phi = 50°$) of C_t and C_z between the model and the DNS with $E \equiv constant$. Model (——), DNS (——) and the vertical position h of the airfoil (- - -)
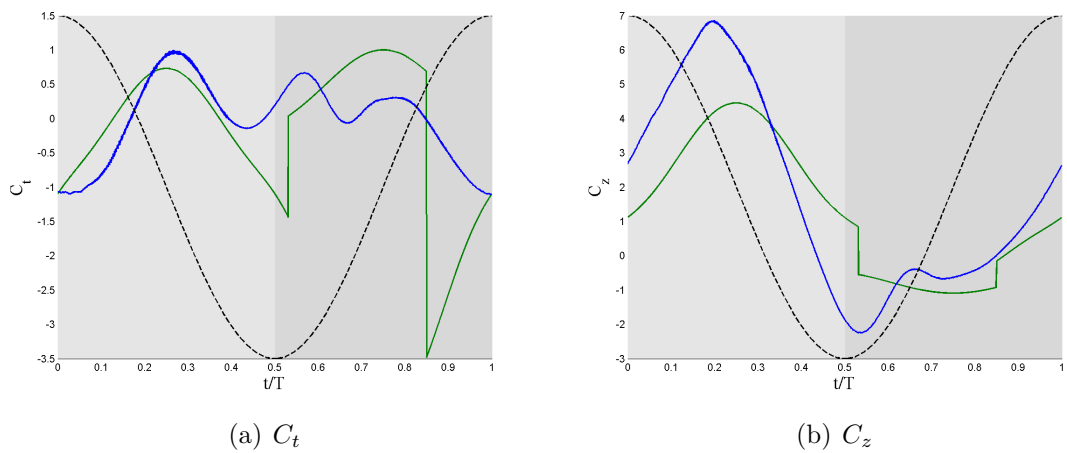

(a) C_t (b) C_z

Figure D.13: Comparison for case 2002 ($\theta_m = 20°$ and $\phi = 70°$) of C_t and C_z between the model and the DNS with $E \equiv constant$. Model (——), DNS (——) and the vertical position h of the airfoil (- - -)
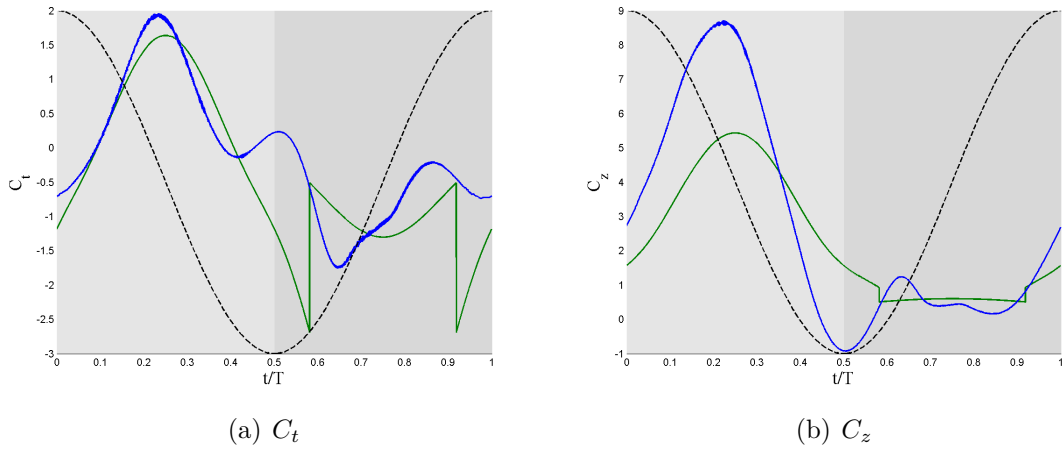
(a) C_t (b) C_z

Figure D.14: Comparison for case 2003 ($\theta_m = 20°$ and $\phi = 90°$) of C_t and C_z between the model and the DNS with $E \equiv constant$. Model (——), DNS (——) and the vertical position h of the airfoil (- - -)
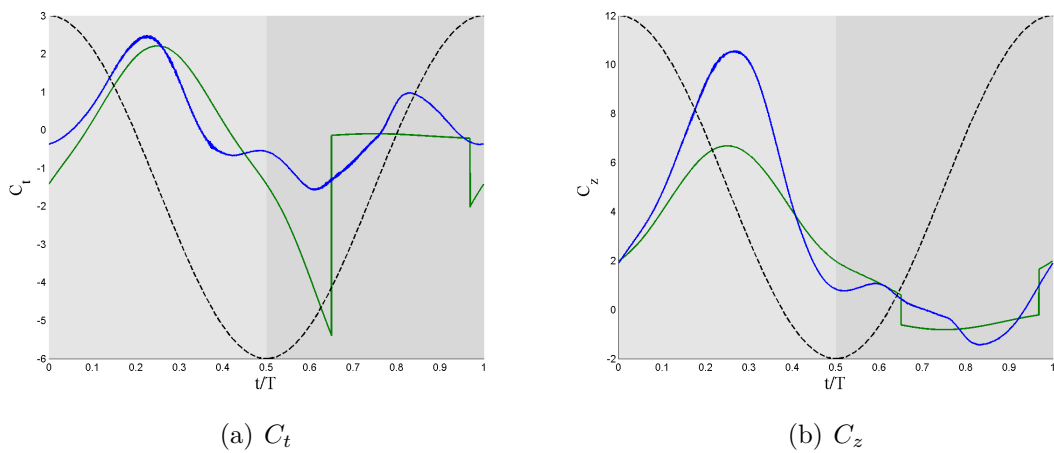

(a) C_t (b) C_z

Figure D.15: Comparison for case 1004 ($\theta_m = 20°$ and $\phi = 110°$) of C_t and C_z between the model and the DNS with $E \equiv constant$. Model (——), DNS (——) and the vertical position h of the airfoil (- - -)

(a) C_t

(b) C_z

Figure D.16: Comparison for case 2005 ($\theta_m = 20°$ and $\phi = 130°$) of C_t and C_z between the model and the DNS with $E \equiv constant$. Model (——), DNS (——) and the vertical position h of the airfoil (- - -)
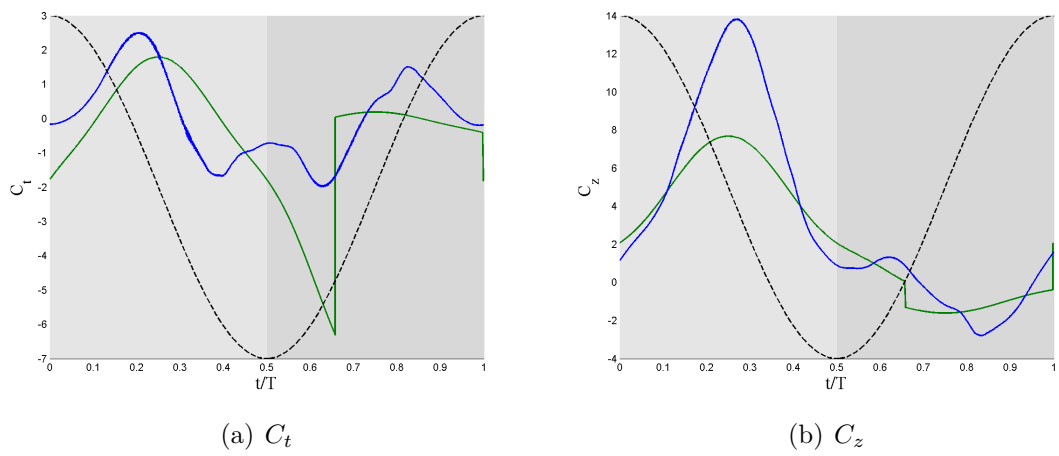
Figures of the results with option 2 and $E = C_{l_{const}}/C_{d_{\propto \alpha_{eff}^2}}$
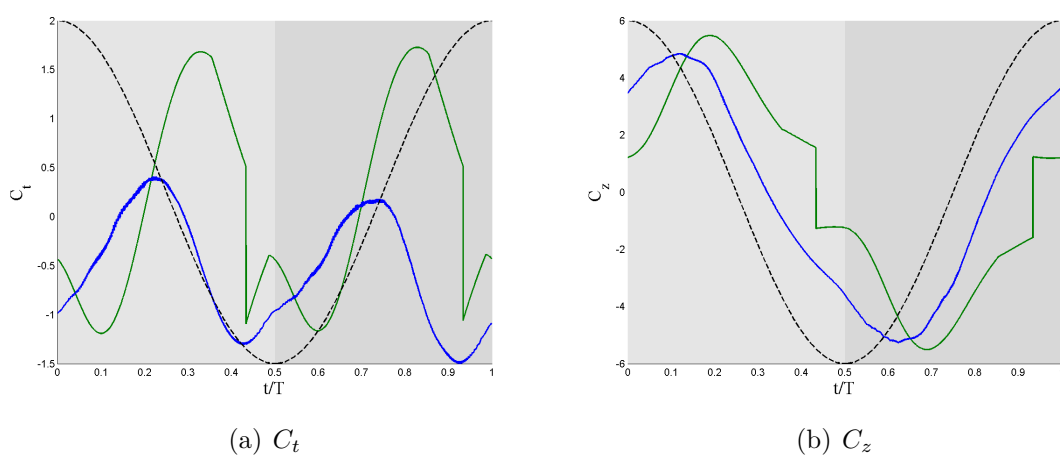

(a) C_t

(b) C_z

Figure E.1: Comparison for case 0000 ($\theta_m = 0°$ and $\phi = 30°$) of C_t and C_z between the model and the DNS with $E = C_{l_{const}}/C_{d_{\propto \alpha_{eff}^2}}$. Model (——), DNS (——) and the vertical position h of the airfoil (- - -)

(a) C_t (b) C_z

Figure E.2: Comparison for case 0001 ($\theta_m = 0°$ and $\phi = 50°$) of C_t and C_z between the model and the DNS with $E = C_{l_{const}}/C_{d_{\propto \alpha^2_{eff}}}$. Model (—), DNS (—) and the vertical position h of the airfoil (- - -)
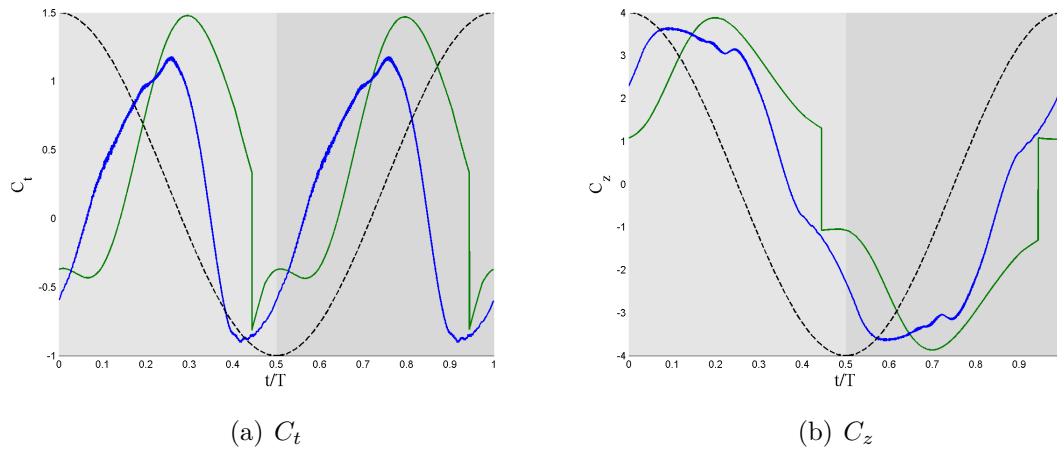

(a) C_t (b) C_z

Figure E.3: Comparison for case 0003 ($\theta_m = 0°$ and $\phi = 90°$) of C_t and C_z between the model and the DNS with $E = C_{l_{const}}/C_{d_{\propto \alpha^2_{eff}}}$. Model (—), DNS (—) and the vertical position h of the airfoil (- - -)
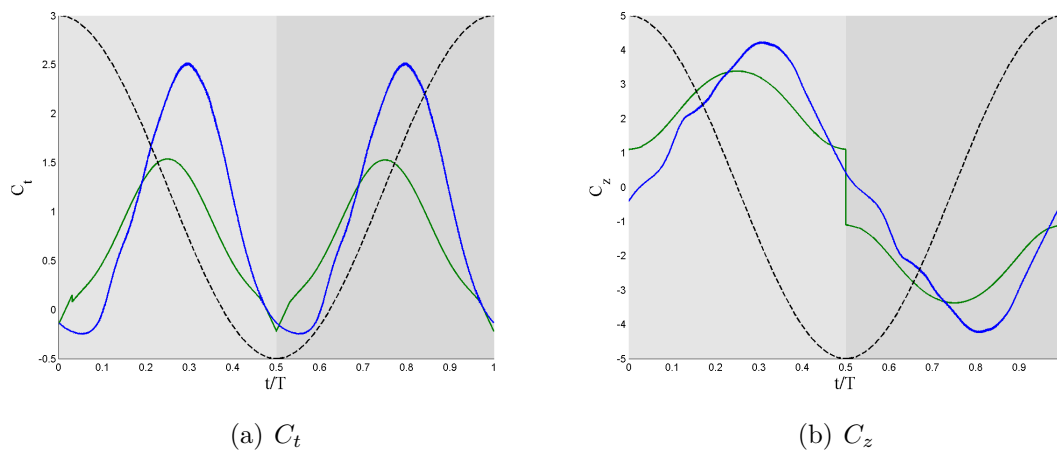
(a) C_t (b) C_z

Figure E.4: Comparison for case 0004 ($\theta_m = 0°$ and $\phi = 110°$) of C_t and C_z between the model and the DNS with $E = C_{l_{const}}/C_{d_{\propto \alpha^2_{eff}}}$. Model (——), DNS (——) and the vertical position h of the airfoil (- - -)
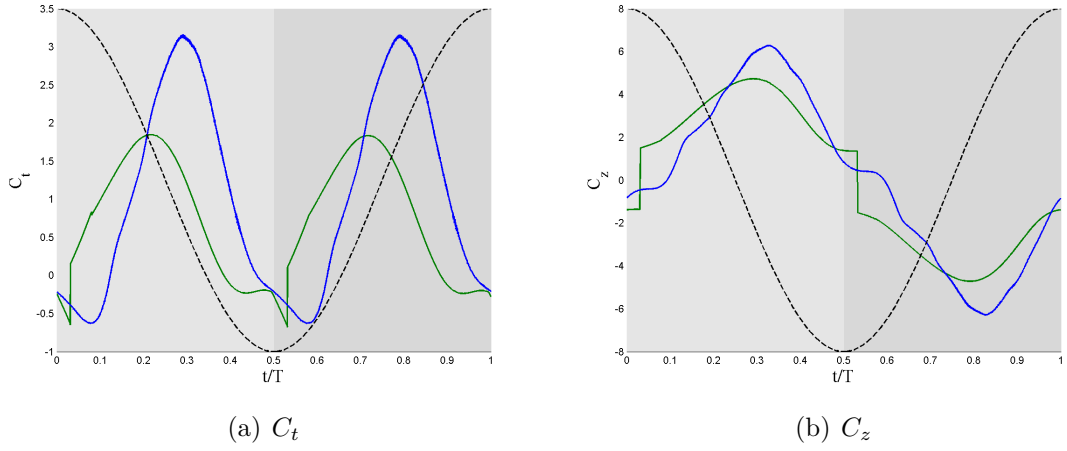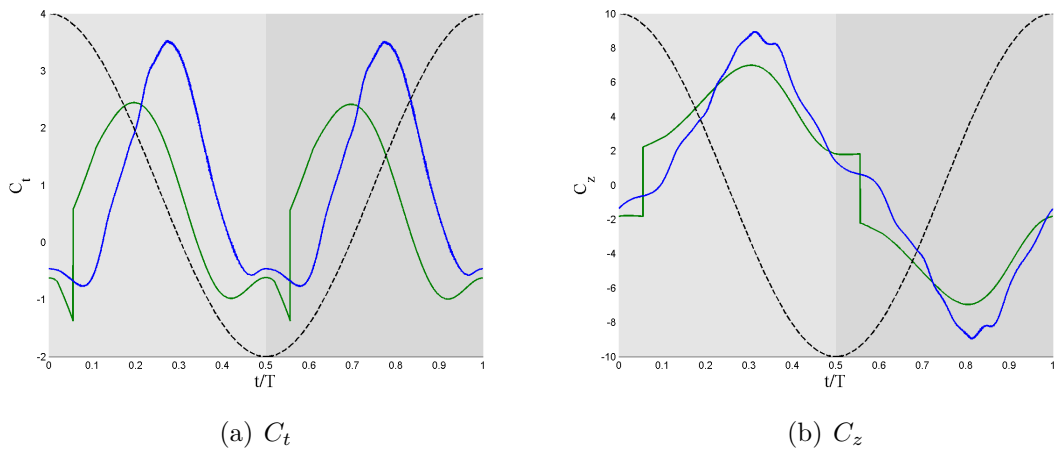

(a) C_t (b) C_z

Figure E.5: Comparison for case 0005 ($\theta_m = 0°$ and $\phi = 130°$) of C_t and C_z between the model and the DNS with $E = C_{l_{const}}/C_{d_{\propto \alpha^2_{eff}}}$. Model (——), DNS (——) and the vertical position h of the airfoil (- - -)

(a) C_t (b) C_z

Figure E.6: Comparison for case 1000 ($\theta_m = 10°$ and $\phi = 30°$) of C_t and C_z between the model and the DNS with $E = C_{l_{const}}/C_{d_{\propto \alpha^2_{eff}}}$. Model (——), DNS (——) and the vertical position h of the airfoil (- - -)
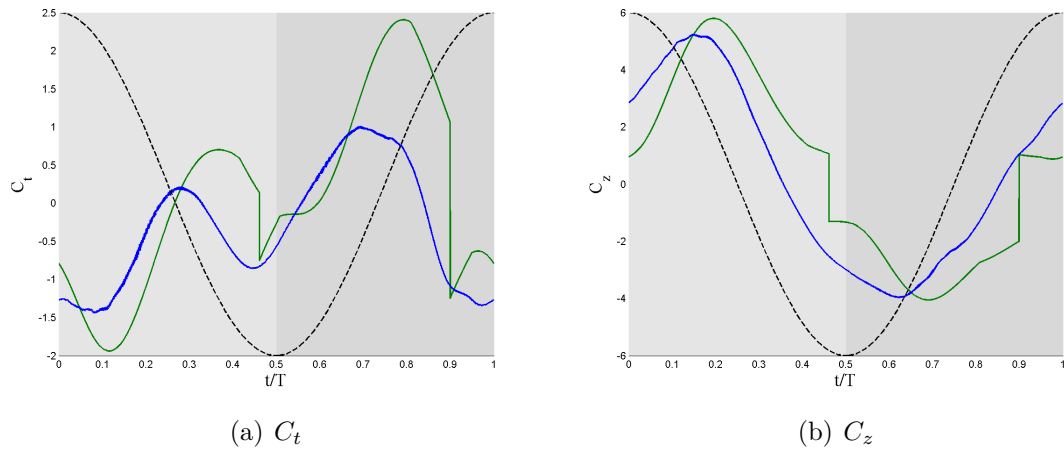

(a) C_t (b) C_z

Figure E.7: Comparison for case 1001 ($\theta_m = 10°$ and $\phi = 50°$) of C_t and C_z between the model and the DNS with $E = C_{l_{const}}/C_{d_{\propto \alpha^2_{eff}}}$. Model (——), DNS (——) and the vertical position h of the airfoil (- - -)
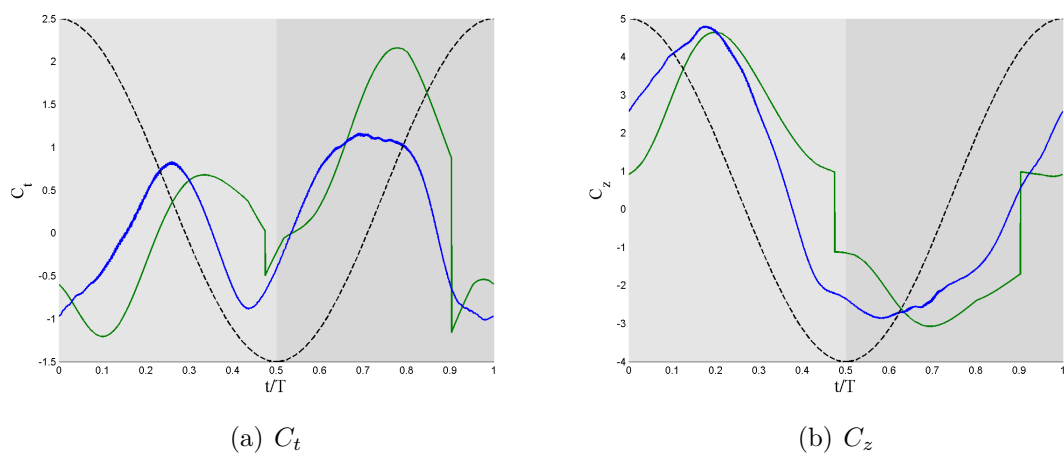
(a) C_t

(b) C_z

Figure E.8: Comparison for case 1002 ($\theta_m = 10°$ and $\phi = 70°$) of C_t and C_z between the model and the DNS with $E = C_{l_{const}}/C_{d_{\propto \alpha^2_{eff}}}$. Model (──), DNS (──) and the vertical position h of the airfoil (- - -)

(a) C_t

(b) C_z

Figure E.9: Comparison for case 1003 ($\theta_m = 10°$ and $\phi = 90°$) of C_t and C_z between the model and the DNS with $E = C_{l_{const}}/C_{d_{\propto \alpha^2_{eff}}}$. Model (──), DNS (──) and the vertical position h of the airfoil (- - -)
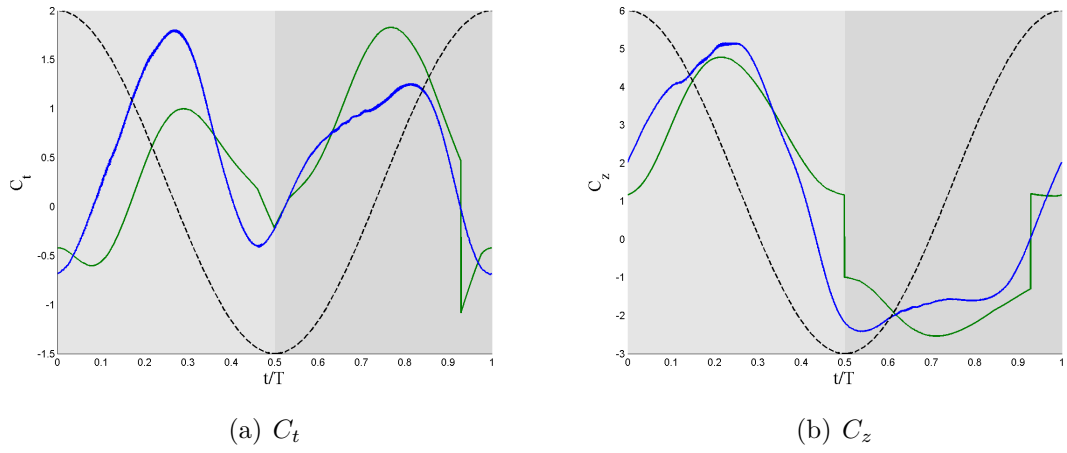
(a) C_t (b) C_z

Figure E.10: Comparison for case 1004 ($\theta_m = 10°$ and $\phi = 110°$) of C_t and C_z between the model and the DNS with $E = C_{l_{const}}/C_{d_{\propto \alpha^2_{eff}}}$. Model (——), DNS (——) and the vertical position h of the airfoil (- - -)
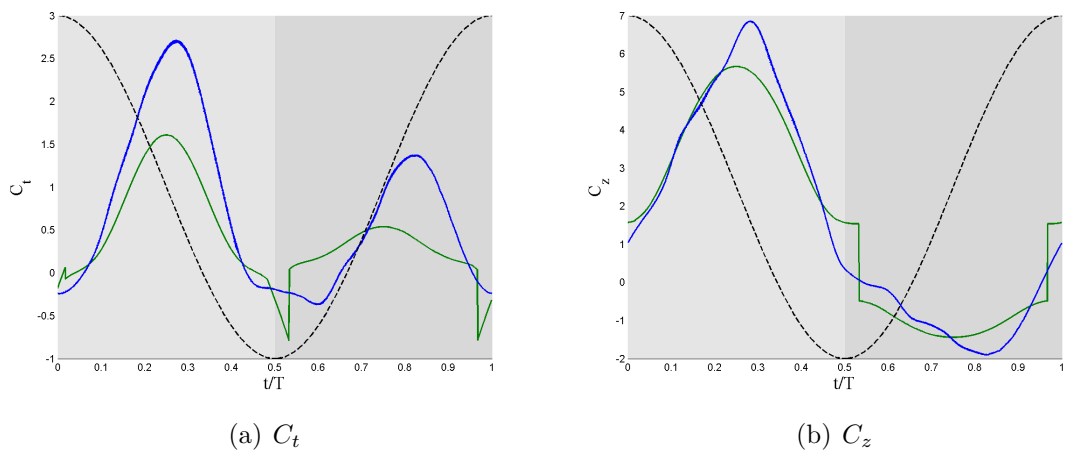

(a) C_t (b) C_z

Figure E.11: Comparison for case 1005 ($\theta_m = 10°$ and $\phi = 130°$) of C_t and C_z between the model and the DNS with $E = C_{l_{const}}/C_{d_{\propto \alpha^2_{eff}}}$. Model (——), DNS (——) and the vertical position h of the airfoil (- - -)
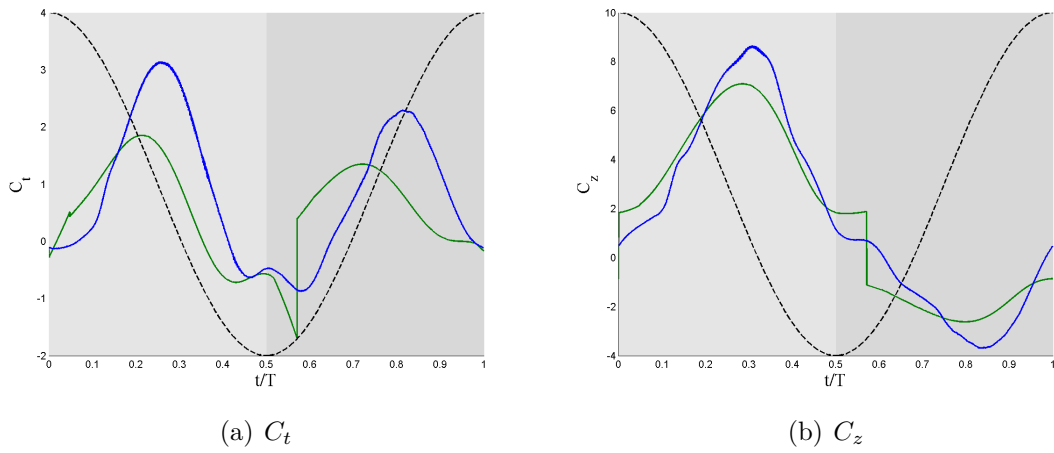
(a) C_t (b) C_z

Figure E.12: Comparison for case 2001 ($\theta_m = 20°$ and $\phi = 50°$) of C_t and C_z between the model and the DNS with $E = C_{l_{const}}/C_{d_{\propto \alpha_{eff}^2}}$. Model (——), DNS (——) and the vertical position h of the airfoil (- - -)
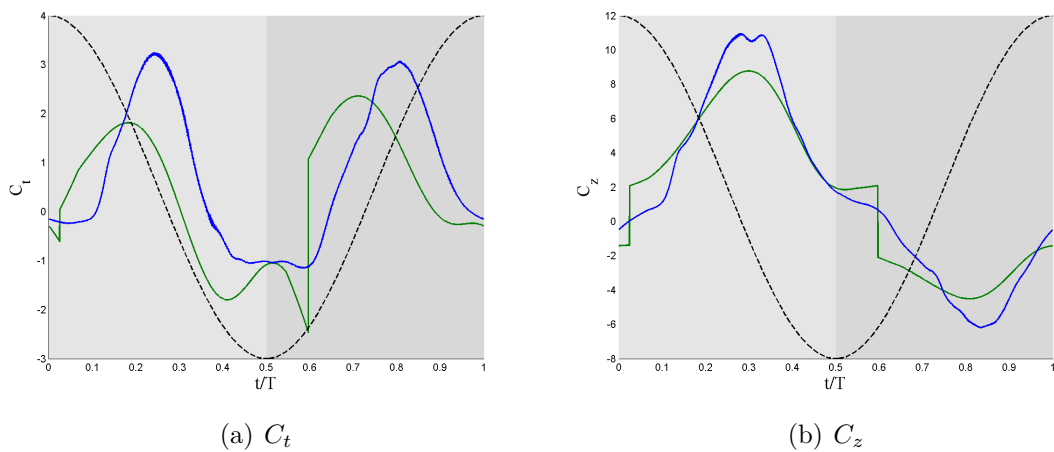

(a) C_t (b) C_z

Figure E.13: Comparison for case 2002 ($\theta_m = 20°$ and $\phi = 70°$) of C_t and C_z between the model and the DNS with $E = C_{l_{const}}/C_{d_{\propto \alpha_{eff}^2}}$. Model (——), DNS (——) and the vertical position h of the airfoil (- - -)
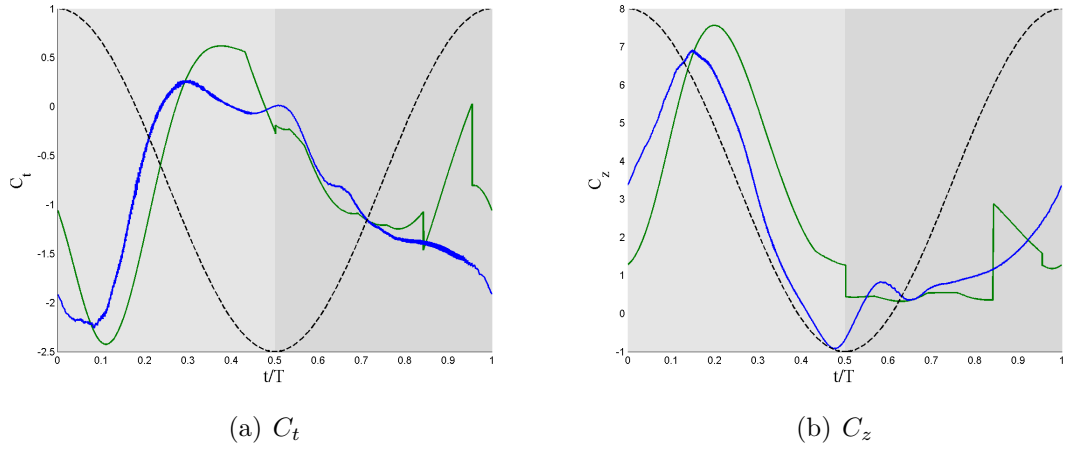
(a) C_t

(b) C_z

Figure E.14: Comparison for case 2003 ($\theta_m = 20°$ and $\phi = 90°$) of C_t and C_z between the model and the DNS with $E = C_{l_{const}}/C_{d_{\propto \alpha^2_{eff}}}$. Model (——), DNS (——) and the vertical position h of the airfoil (‐ ‐ ‐)
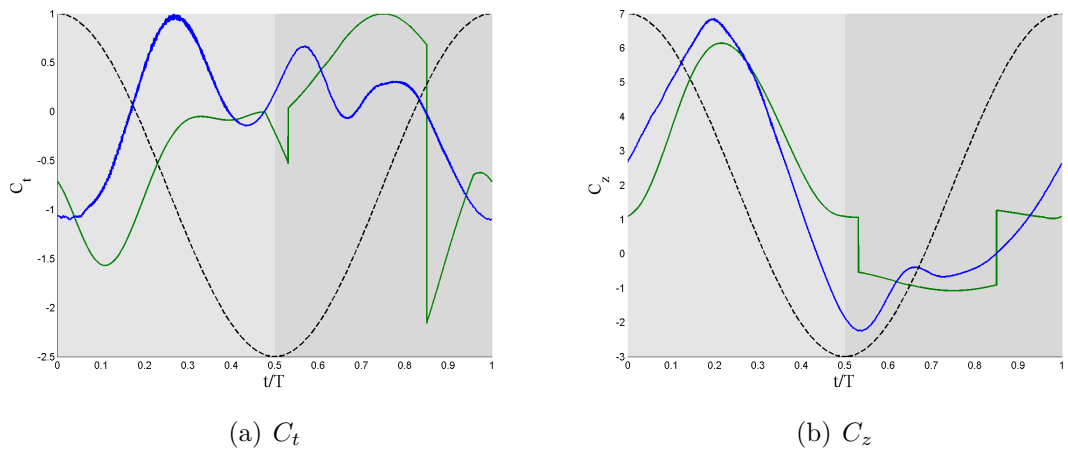

(a) C_t

(b) C_z

Figure E.15: Comparison for case 1004 ($\theta_m = 20°$ and $\phi = 110°$) of C_t and C_z between the model and the DNS with $E = C_{l_{const}}/C_{d_{\propto \alpha^2_{eff}}}$. Model (——), DNS (——) and the vertical position h of the airfoil (‐ ‐ ‐)
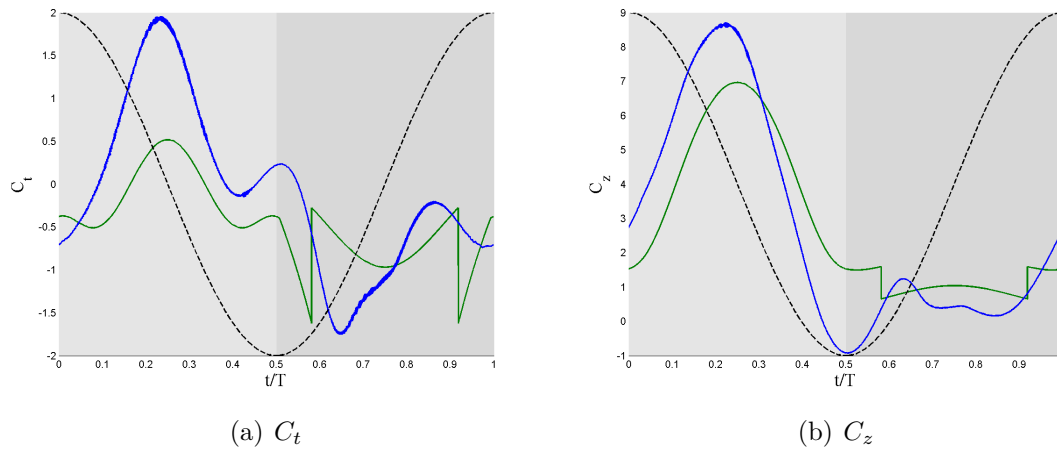
(a) C_t (b) C_z

Figure E.16: Comparison for case 2005 ($\theta_m = 20°$ and $\phi = 130°$) of C_t and C_z between the model and the DNS with $E = C_{l_{const}}/C_{d_{\propto \alpha^2_{eff}}}$. Model (——), DNS (——) and the vertical position h of the airfoil (- - -)
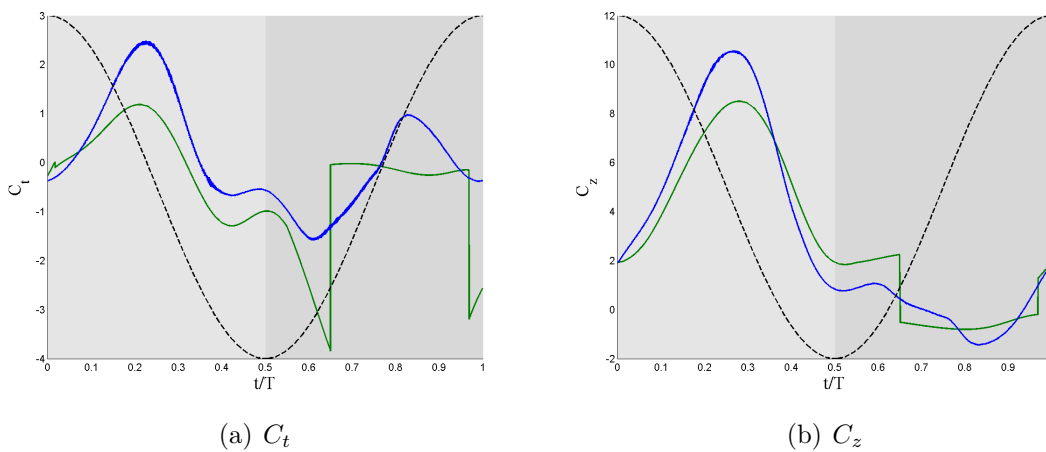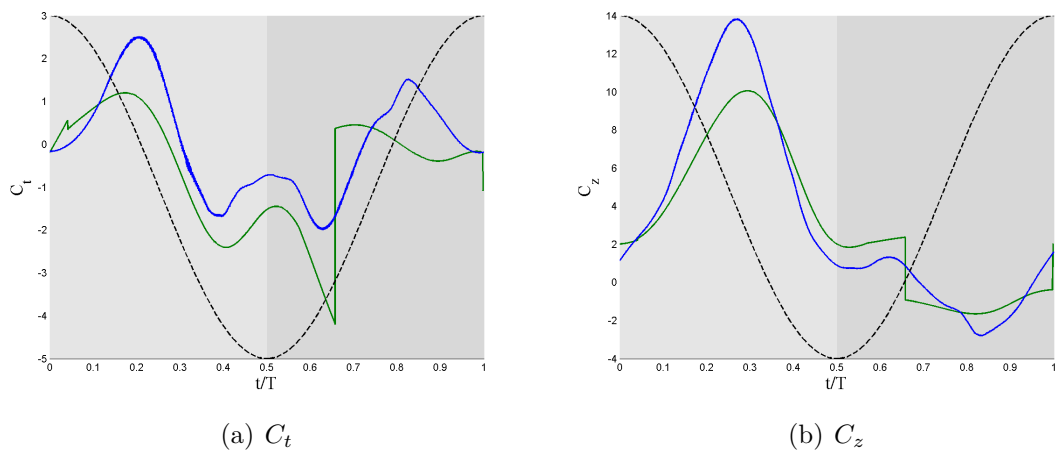
Bibliography

[1] SA Ansari, R Żbikowski, and Kevin Knowles. Aerodynamic modelling of insect-like flapping flight for micro air vehicles. *Progress in Aerospace Sciences*, 42(2):129–172, 2006.

[2] S Sunada and CP Ellington. Approximate added-mass method for estimating induced power for flapping flight. *AIAA journal*, 38(8):1313–1321, 2000.

[3] Wilhelm Hoff. Der flug der insekten und der vögel. *Naturwissenschaften*, 7(10):159–162, 1919.

[4] Torkel Weis-Fogh. Energetics of hovering flight in hummingbirds and in drosophila. *Journal of Experimental Biology*, 56(1):79–104, 1972.

[5] Ellington CP. The aerodynamics of hovering flight v. a vortex theory.

[6] JMV Rayner. A vortex theory of animal flight. part 1. the vortex wake of a hovering animal. *Journal of Fluid Mechanics*, 91(04):697–730, 1979.

[7] MFM Osborne. Aerodynamics of flapping flight with application to insects. *Journal of Experimental Biology*, 28(2):221–245, 1951.

[8] Torkel Weis-Fogh. Quick estimates of flight fitness in hovering animals, including novel mechanisms for lift production. *Journal of Experimental Biology*, 59(1):169–230, 1973.

[9] Akira Azuma. *The biokinetics of flying and swimming.* Springer Science & Business Media, 2012.

[10] Salman Ahmad Ansari. *A nonlinear, unsteady aerodynamic model for insect-like flapping wings in the hover with micro air vehicle applications.* PhD thesis, Cranfield University, 2004.

[11] Theodore Yaotsu Wu. On theoretical modeling of aquatic and aerial animal locomotion. *Advances in applied mechanics*, 38:291–350, 2002.

[12] Rafal Żbikowski. On aerodynamic modelling of an insect–like flapping wing in hover for micro air vehicles. *Philosophical Transactions of the Royal Society of London A: Mathematical, Physical and Engineering Sciences*, 360(1791):273–290, 2002.

[13] CP Ellington. The aerodynamics of hovering insect flight. i. the quasi-steady analysis. *Philosophical Transactions of the Royal Society B: Biological Sciences*, 305(1122):1–15, 1984.

[14] Wayne Johnson. *Helicopter theory*. Courier Corporation, 2012.

[15] John M Seddon and Simon Newman. *Basic helicopter aerodynamics*, volume 40. John Wiley & Sons, 2011.